

Star Formation Efficiency and Dispersal of Giant Molecular Clouds with UV Radiation Feedback: Dependence on Gravitational Boundedness and Magnetic Fields

JEONG-GYU KIM,¹ EVE C. OSTRIKER,¹ AND NINA FILIPPOVA¹

¹*Department of Astrophysical Sciences, Princeton University, Princeton, NJ 08544, USA*

ABSTRACT

Molecular clouds are supported by turbulence and magnetic fields, but quantifying their influence on cloud lifecycle and star formation efficiency (SFE) remains an open question. We perform radiation magnetohydrodynamic simulations of star-forming giant molecular clouds (GMCs) with UV radiation feedback, in which the propagation of UV radiation via ray-tracing is coupled to hydrogen photochemistry. We consider 10 GMC models that vary in either initial virial parameter ($1 \leq \alpha_{\text{vir},0} \leq 5$) or dimensionless mass-to-magnetic flux ratio ($0.5 \leq \mu_{\Phi,0} \leq 8$ and ∞); the initial mass $10^5 M_{\odot}$ and radius 20 pc are fixed. Each model is run with five different initial turbulence realizations. In most models, the duration of star formation and the timescale for molecular gas removal (primarily by photovaporation) are 4–8 Myr. Both the final SFE (ε_*) and time-averaged SFE per freefall time (ε_{ff}) are reduced by strong turbulence and magnetic fields. The median ε_* ranges between 2.1% and 9.5%. The median ε_{ff} ranges between 1.0% and 8.0% and anticorrelates with $\alpha_{\text{vir},0}$, in qualitative agreement with previous analytic theory and simulations. However, the time-dependent $\alpha_{\text{vir}}(t)$ and $\varepsilon_{\text{ff,obs}}(t)$ based on instantaneous gas properties and cluster luminosity are positively correlated due to rapid evolution, making observational validation of star formation theory difficult. Our median $\varepsilon_{\text{ff,obs}}(t) \approx 2\%$ is similar to observed values. We show that the traditional virial parameter estimates the true gravitational boundedness within a factor of 2 on average, but neglect of magnetic support and velocity anisotropy can sometimes produce large departures. Magnetically subcritical clouds are unlikely to represent sites of massive star formation given their unrealistic columnar outflows, prolonged lifetime, and low escape fraction of radiation.

Keywords: Giant molecular clouds (653), H II regions (694), Interstellar medium (847), Magnetic Fields (994), Star formation (1569), Stellar feedback (1602), Radiative magnetohydrodynamics (2009)

1. INTRODUCTION

Giant molecular clouds (GMCs) are the primary reservoir of the cold, molecular interstellar medium (ISM) and sites of ongoing star formation. The gas distribution and velocity structure of GMCs are highly complex and hierarchical, arising from the interplay of supersonic turbulence, magnetic fields, stellar feedback, and gravity. Both turbulent flows and magnetic fields are thought to play crucial roles in structure formation as well as in preventing excessive star formation by providing support against gravity (Mac Low & Klessen 2004; McKee & Ostriker 2007; Hennebelle & Inutsuka 2019; Krumholz & Federrath 2019). For example, turbulence can both create and disperse local density enhancements such as sheets, filaments, and cores, some of which become sufficiently dense to be susceptible to gravitational contraction. Magnetic fields can guide gas flows and help organize mass into filaments, but also prevent collapse if sufficiently strong.

Massive stars formed in GMCs produce intense ultraviolet (UV) radiation and stellar winds during their

evolution, and explode as supernovae at the end of their lives. The energy and momentum injected by these processes can be destructive to the natal clouds and quench star formation activity. Therefore, the efficiency with which each feedback mechanism (individually and in combination) couples to the ISM within turbulent and magnetized molecular clouds is key to understanding several important issues, such as the lifecycle of molecular clouds and formation of star clusters (Krumholz et al. 2019; Adamo et al. 2020; Chevance et al. 2020a).

Extensive surveys of molecular lines in the Milky Way and nearby galaxies have provided us with rich data that reveal physical properties of GMCs. Typical GMCs in the main disk of the Milky Way and nearby disk galaxies have mass $M \sim 10^4$ – $10^6 M_{\odot}$, size $R \sim 10$ – 10^2 pc, surface density $\Sigma \sim 10$ – $10^3 M_{\odot} \text{ pc}^{-2}$, and one dimensional (1D) velocity dispersion $\sigma_{1\text{d}} \sim 1$ – 8 km s^{-1} (e.g., Bolatto et al. 2008; Heyer et al. 2009; Fukui & Kawamura 2010; Heyer & Dame 2015; Miville-Deschénes et al. 2017). From extragalactic surveys, certain cloud properties such as surface density, velocity dispersion, and internal turbulent pressure widely vary as a function of

galactic environment (Sun et al. 2018, 2020a,b). The virial parameter α_{vir} , which measures the relative importance of the turbulent kinetic energy to the self-gravitational energy (albeit with some simplifying assumptions), has a relatively narrow distribution with a typical value $\sim 0.5 - 5$ (Roman-Duval et al. 2010; Heyer & Dame 2015; Sun et al. 2018, 2020b). This suggests that molecular clouds are self-gravitating yet internal turbulent support is sufficient to prevent global collapse. While self-gravity is important to GMCs' dynamical state (Sun et al. 2020a), they are not necessarily virialized or even gravitationally bound as isolated systems. Nevertheless, overdense clumps in filaments within GMCs are more strongly bound (Kauffmann et al. 2013), and these are susceptible to collapse and star formation.

Although observational constraints are indirect and weak, GMCs are permeated by dynamically important magnetic fields (see the review by Crutcher 2012). Linear polarization of dust thermal emission and spectral lines shows that molecular clouds have a well-defined mean field direction that is correlated with the direction of larger scale Galactic magnetic fields (Li et al. 2006; Li & Henning 2011; Li et al. 2013). The orientation of the local magnetic field is perpendicular to dense filaments, whereas it tends to be aligned with low-density filaments connected to dense filaments (Palmeirim et al. 2013; Planck Collaboration et al. 2016; Ward-Thompson et al. 2017; Soler 2019). Observing Zeeman splitting of spectral lines is the only direct method to obtain the line-of-sight component of magnetic field strength. The geometry-corrected total magnetic field strength B_{tot} is relatively constant $\sim 6 \mu\text{G}$ in diffuse H I clouds (Heiles & Troland 2005), but increases roughly as $B_{\text{tot}} \propto n_{\text{H}}^{2/3}$ in denser molecular gas (Crutcher et al. 2010). The average dimensionless mass-to-magnetic flux ratio $\mu_{\Phi} \propto M_{\text{gas}}/\Phi \propto \Sigma/B_{\text{tot}}$, which measures the relative importance of magnetic fields to gravity, exceeds unity (supercritical) by a factor $\sim 2-3$ in molecular cores (Crutcher 1999; Crutcher et al. 2010). Recently, Thompson et al. (2019) measured the magnetic strength of low-density (inter-core) regions of nearby molecular clouds obtained from OH Zeeman effect, finding the total magnetic strength of a few μG to $30 \mu\text{G}$ with mean $15 \mu\text{G}$.

The efficiency and rate of star formation (SFE and SFR) on the scale of molecular clouds are both low (e.g., Mooney & Solomon 1988; Evans 1991; Kennicutt & Evans 2012; Utomo et al. 2018). Observational constraints on the net (or final) SFE of GMCs, the fraction of the initial cloud gas mass that will ever become stars before destruction, can be obtained indirectly based on a “snapshot” view of a population of clouds in different evolutionary stages. The distribution of instantaneous SFE $\varepsilon = M_*/(M_* + M_{\text{gas}})$ suggests that GMCs in the Milky Way convert only a small fraction of gas into stars before dispersal (e.g., Myers et al. 1986; Lee et al.

2016). The fraction of gas mass turned into stars per freefall time (or SFE per freefall time, ε_{ff}), is also very small with large scatter (e.g., Krumholz & Tan 2007; Lee et al. 2016; Vutisalchavakul et al. 2016; Ochsendorf et al. 2017; for a recent review, see Section 3.2 of Krumholz et al. 2019). Curiously, however, Lee et al. (2016); Vutisalchavakul et al. (2016) found no significant correlation between estimated ε_{ff} and the instantaneous α_{vir} , while an anticorrelation is predicted by analytic theory and numerical simulations of star formation (e.g., Krumholz & McKee 2005; Federrath & Klessen 2012; Padoan et al. 2012). The question of whether GMCs are transients or long-lived objects has historically been controversial (Heyer & Dame 2015), but recent investigation of cloud evolutionary timelines based on scale-dependent CO-to-H α flux ratios shows that molecular clouds are dispersed rapidly ($\lesssim 5$ Myr) after the onset of massive star formation in a range of star-forming galaxies (Kruijssen et al. 2019; Chevance et al. 2020b,c). The youth of clusters ($\sim 2-4$ Myr) associated with molecular clouds in external galaxies also suggests rapid disruption by stellar feedback (Grasha et al. 2018, 2019).

From a theoretical point of view, a number of authors have studied how the SFE depends on cloud properties and the feedback processes that are included (see the reviews by Padoan et al. 2014; Krumholz 2014a; Dale 2015; Krumholz et al. 2019). Much theoretical work agrees that a higher net SFE is required for the destruction of massive, high surface density clouds and that the disruption is rapid occurring roughly over the gas free-fall time (e.g., Fall et al. 2010; Kim et al. 2016; Raskutti et al. 2016; Geen et al. 2017; Grudić et al. 2018; Kim et al. 2018; Li et al. 2019; Rahner et al. 2019; Fukushima et al. 2020). Simple models of cloud dispersal based on 1D dynamical expansion (driven by thermal pressure of photoionized gas and radiation pressure on dust) and photoevaporation show that H II regions produced by UV radiation are very effective in clearing out gas in low- and moderate- Σ clouds, requiring only a few percent of SFE (e.g., Whitworth 1979; Franco et al. 1994; Williams & McKee 1997; Matzner 2002; Krumholz et al. 2006; Murray et al. 2010; Kim et al. 2016; Rahner et al. 2019; Inoguchi et al. 2020).

In realistic turbulent clouds with multiple sources of radiation, the momentum injection by feedback is less effective than in simple 1D analytic models due to the escape of radiation and lack of spherical symmetry (e.g., Dale 2017; Raskutti et al. 2017; Kim et al. 2018, 2019b). Still, simulations show that UV radiation feedback can keep the SFE low and disperse the cloud within $\lesssim 10$ Myr in low- and moderate- Σ clouds (Raskutti et al. 2016; Grudić et al. 2018; Kim et al. 2018; He et al. 2019; Fukushima et al. 2020; González-Samaniego & Vazquez-Semadeni 2020), although massive, high- Σ clouds with large escape velocity are less prone to disruption (Dale et al. 2012; Kim et al. 2018). While photoevaporation is the dominant mechanism for

cloud dispersal in low- and moderate- Σ clouds, radiation pressure on dust grains becomes more important than photoionization at $\Sigma \sim 10^3 M_\odot \text{ pc}^{-2}$ (Kim et al. 2018).

Despite the recent progress in the field, several questions still remain. First, simulations of turbulent, star-forming clouds that use *magnetohydrodynamics* (rather than hydrodynamics) have been mostly limited to low-mass clouds with periodic boundary conditions (e.g., Federrath 2015; Cunningham et al. 2018), and have not included effects of massive star feedback that definitively quenches star formation. A few studies included magnetic fields of various levels in simulations of GMC dispersal following star formation (e.g., Grudić et al. 2018; Geen et al. 2018; Zamora-Avilés et al. 2019; He et al. 2019) and in simulations with a single, constant-luminosity source put in by hand (Geen et al. 2016; Arthur et al. 2011), but a systematic, quantitative study of the effects of magnetic field strength on GMC dispersal with self-consistent star formation has been lacking. Second, both theory and simulations indicate that the gravitational boundedness (α_{vir}) is the primary parameter controlling the SFE per freefall time, but the lack of correlation between observationally inferred α_{vir} and ε_{ff} requires an explanation. Third, even at a given kinetic energy, the evolution of a cloud will differ depending on the relative amplitude of different modes in the spectrum of turbulence, and it is interesting to understand how much this might contribute to observed variances (in the SFR, SFE, and lifetime). Fourth, the usual virial parameter makes a number of assumptions about cloud geometry and ignores the contributions from magnetic fields, and it is important to assess quantitatively how reliable it is as a magnetized, turbulent cloud evolves and is dispersed under the influence of feedback. Fifth, many simulations use approximate numerical treatments of radiation feedback (e.g., Dale et al. 2012; Grudić et al. 2018; González-Samaniego & Vazquez-Semadeni 2020) and/or adopt an isothermal equation of state (e.g., Dale et al. 2012; Kim et al. 2018), rather than implementing explicit radiative transfer with heating/cooling and ionization/recombination, and it is not known how much these simplified numerical treatments compromise the conclusions. To make progress on these and other pressing questions, controlled numerical simulations with high-accuracy and performance-optimized algorithms for solving the equations of radiation magnetohydrodynamics (RMHD) are required.

In this work, we carry out a suite of RMHD simulations to study the dynamical evolution and progress of star formation in a turbulent, magnetized molecular cloud under the influence of UV radiation feedback. A key aspect of evolution is the quenching of star formation by the dispersal of the cloud. In addition to including magnetic fields, we improve upon our previous simulations (Kim et al. 2018, 2019b) by coupling the UV radiative transfer with a simple thermochemistry module

that tracks the non-equilibrium abundances of molecular, ionized, and atomic hydrogen and includes realistic heating and cooling processes. We consider a cloud with fixed mass and size typical of GMCs in the Milky Way but vary the initial virial parameter, mass-to-magnetic flux ratio, and specific realization of the turbulent velocity spectrum. Our simulation suite has 10 sets of different model parameters, for a total of 50 runs.

We systematically explore how the morphological evolution, SFR, SFE, photoevaporation, timescales of star formation and cloud destruction, and escape fraction of radiation depend on the initial virial parameter and mass-to-magnetic ratio, and quantify variations resulting from the initial turbulence realization. We also test the reliability of the triadiational virial parameter by comparing it with the true virial parameter that allows for the cloud’s total energy accounting for full distributions of gas, stars, and magnetic fields. Finally, we study the relationship between the SFE per freefall time and virial parameter measured from our simulations, as compared to previous theoretical models of SFR and observations of star-forming clouds.

The plan of this paper is as follows. In Section 2, we describe our numerical methods and model parameters. In Section 3, we present the simulation results. We first describe the overall evolution of the fiducial model (3.1) and other models (3.2). In Sections 3.3–3.7, we intercompare quantitative simulation outcomes such as star formation history, SFE, photoevaporation fraction, evolutionary timescales, and radiation escape fractions. In Section 3.8, we present our analysis of the virial parameter. Section 3.9 compares our result on the star formation efficiency per freefall time with other theoretical and observational work. Finally, in Section 4 we summarize our results and discuss their implications.

2. METHODS

We carry out RMHD simulations of cloud evolution and destruction by UV radiation feedback, focusing on the effects of the initial cloud virial parameter and magnetic fields. Our simulations are performed using the grid-based MHD code *Athena* (Stone et al. 2008), with additional physics modules for gravity (using open boundary conditions), sink particles, heating/cooling, photochemistry, and adaptive ray-tracing of radiation originating in clusters. The simulation setup is largely similar to that used by Kim et al. (2017, 2018, 2019b), with the addition of magnetic fields, UV background radiation (treated using a six-ray shielding approximation), more detailed photochemical and heating/cooling processes, and time-dependent luminosity of star clusters. In this section, we present our basic equations, establish notation, outline our numerical methods, and summarize simulation parameters.

2.1. Basic Equations

The set of equations we solve are

$$\frac{\partial \rho}{\partial t} + \nabla \cdot (\rho \mathbf{v}) = 0, \quad (1)$$

$$\frac{\partial(\rho \mathbf{v})}{\partial t} + \nabla \cdot \left[\rho \mathbf{v} \mathbf{v} + P^* \mathbb{I} - \frac{\mathbf{B} \mathbf{B}}{4\pi} \right] = -\rho \nabla \Phi + \mathbf{f}_{\text{rad}}, \quad (2)$$

$$\frac{\partial E}{\partial t} + \nabla \cdot \left[(E + P^*) \mathbf{v} - \frac{\mathbf{B}(\mathbf{B} \cdot \mathbf{v})}{4\pi} \right] = \mathcal{G} - \mathcal{L} + \mathbf{v} \cdot (-\rho \nabla \Phi + \mathbf{f}_{\text{rad}}), \quad (3)$$

$$\frac{\partial n_s}{\partial t} + \nabla \cdot (n_s \mathbf{v}) = n_{\text{H}} \mathcal{C}_s, \quad (4)$$

$$\frac{\partial \mathbf{B}}{\partial t} - \nabla \times (\mathbf{v} \times \mathbf{B}) = 0, \quad (5)$$

$$\nabla^2 \Phi = 4\pi G(\rho + \rho_*). \quad (6)$$

Here, $P^* = P + B^2/(8\pi)$ is the sum of gas pressure and magnetic pressure, \mathbf{f}_{rad} is the radiative force per unit volume, Φ is the total gravitational potential due to gas and stars, $E = P/(\gamma - 1) + \rho v^2/2 + B^2/(8\pi)$ is the total energy density with the ratio of specific heats $\gamma = 5/3$, \mathcal{G} and \mathcal{L} are the volumetric heating and cooling rates. The number density of hydrogen is denoted as $n_{\text{H}} \equiv \rho/(\mu_{\text{H}} m_{\text{H}})$, where $\mu_{\text{H}} m_{\text{H}} = 2.37 \times 10^{-24} \text{ g}$ is the mean mass of all gas per hydrogen nucleus.

The quantity $n_s = x_s n_{\text{H}}$ represents the number density of species “s,” where x_s is the fractional abundance relative to the hydrogen nucleus. Each species we follow is passively advected with the velocity field, with the right-hand side of Equation (4) representing the net creation rate \mathcal{C}_s due to various collisional reactions, cosmic ray ionization, and photodestruction processes. We explicitly follow the non-equilibrium abundances of hydrogen in molecular (H_2), atomic neutral (H^0), and ionized (H^+) phases but assume equilibrium abundances for carbon- and oxygen-bearing species (C^0 , C^+ , CO , O^0) (see Section 2.3). Adopting the ideal gas law, assuming $x_{\text{He}} = 0.1$, and ignoring the abundance of trace species, the gas temperature can be written as $T = P/[(1.1 + x_{\text{e}} - x_{\text{H}_2}) k_{\text{B}} n_{\text{H}}]$.

In addition to Equations (1)–(6), we solve radiative transfer equations in the form

$$\hat{\mathbf{n}} \cdot \nabla I = -\kappa I \quad (7)$$

where I is the intensity, κ is crosssection per unit volume in a given radiation component, and $\hat{\mathbf{n}}$ is the direction of ray propagation. The scattering and emission by dust grains are ignored. The radiation field is decomposed into diffuse background and starlight: $I = I^{\text{bg}} + I^*$. We use the six-ray approximation to solve for the diffuse background, meaning that only $\hat{\mathbf{n}}$ aligned with the

cardinal axes of the grid are considered. For the radiation produced by star particles formed in the simulation, we use the adaptive ray-tracing technique. We include three different frequency components for the radiation field.

2.2. Star Formation and Radiation Feedback

Star formation is modeled via the sink particle method of [Gong & Ostriker \(2013\)](#) (slightly updated as described in [Kim et al. 2020](#)). A sink particle is created if a gas cell (1) exceeds the Larson-Penston density criterion for self-gravitating collapse ($\rho_{\text{crit}} = 8.86 c_s^2/(\pi G \Delta x^2)$ for the local sound speed $c_s = \sqrt{\gamma P/\rho}$ and the grid spacing Δx), (2) is located at a local minimum of the gravitational potential, and (3) has the velocity field converging along the three Cartesian axes. For actively accreting sink particles, we reset the density, momentum, and energy of 3^3 cells surrounding each sink particle (control volume) by extrapolating from surrounding non-control volume cells after the MHD update. The accretion rates of mass and momentum onto sink particles are determined based on the flux across the surface of the control volume, subtracting out the difference between the total mass and momentum on the grid inside the control volume at the beginning and end of the step.

Once sink particles are formed, they are considered as discrete, point sources of UV radiation. Since individual stars are not resolved in our simulations (with typical mass of individual sink particles being a few hundred solar masses), we assume that each sink particle represents a coeval stellar population following the Kroupa initial mass function (IMF) with mass-weighted mean age t_{age} (e.g., [Kim & Ostriker 2017](#)). Using the stellar population synthesis model STARBURST99 ([Leitherer et al. 2014](#)), the time-dependent radiative output per unit mass Ψ is calculated in three frequency bins: (1) Photoelectric (PE; $110.8 \text{ nm} < \lambda < 206.6 \text{ nm}$); (2) Lyman-Werner (LW; $91.2 \text{ nm} < \lambda < 110.8 \text{ nm}$); (3) Lyman Continuum (LyC; $\lambda < 91.2 \text{ nm}$). The PE and LW constitute FUV (or non-ionizing) radiation and are absorbed mainly by dust. Absorption of the FUV photons by small grains ejects electrons, which are important for heating neutral gas. The LW photons include photodissociation bands of H_2 and CO molecules and also ionize C^0 . The LyC (or ionizing) photons are responsible for ionizing H^0 ($h\nu > 13.6 \text{ eV}$) and H_2 ($h\nu > 15.2 \text{ eV}$). We assume that the mean energy of ionizing photons is $h\nu_{\text{LyC}} = 18 \text{ eV}$. In Appendix A, we show $\Psi(t_{\text{age}})$ in different frequency bins.

We calculate the cross sections for dust absorption and photoionization averaged over the cluster’s UV spectrum and find that the dependence on t_{age} is weak. We thus take constant cross sections $\kappa_{\text{PE}} = n_{\text{H}} \sigma_{\text{d,PE}}$ and $\kappa_{\text{LW}} = n_{\text{H}} \sigma_{\text{d,LW}}$, where $\sigma_{\text{d,PE}} = 10^{-21} \text{ cm}^2 \text{ H}^{-1}$ and $\sigma_{\text{d,LW}} = 1.5 \times 10^{-21} \text{ cm}^2 \text{ H}^{-1}$. These values are appropriate for [Weingartner & Draine \(2001a\)](#)’s grain model with $R_V = 3.1$. For LyC radiation, we

take $\kappa_{\text{LyC}} = n_{\text{H}}\sigma_{\text{d,LyC}} + n_{\text{H}^0}\sigma_{\text{pi,H}^0} + n_{\text{H}_2}\sigma_{\text{pi,H}_2}$, where $\sigma_{\text{d,LyC}} = 10^{-18} \text{ cm}^2$, $\sigma_{\text{pi,H}^0} = 3 \times 10^{-18} \text{ cm}^2$, and $\sigma_{\text{pi,H}_2} = 6 \times 10^{-18} \text{ cm}^2$.

We note that the dust absorption cross section for LyC radiation is uncertain; in H II regions small carbonaceous grains (or PAHs) can be destroyed by an intense radiation field (e.g., Deharveng et al. 2010; Chastenet et al. 2019), while large grains can be disrupted by radiative torque and disintegrate into smaller grains (Hoang et al. 2019) or swept out by radiation pressure (e.g., Draine 2011a; Akimkin et al. 2015). Our adopted value would be intermediate between the case of the complete destruction and the case of no destruction (see also Glatzle et al. 2019). Kim et al. (2019b) found that using a lower value of $\sigma_{\text{d,LyC}}$ does not affect the overall cloud evolution and star formation, although the escape fraction of ionizing radiation can be boosted significantly.

We employ the adaptive ray-tracing module of Kim et al. (2017) to model the propagation of radiation from multiple point sources. The reader is referred to Kim et al. (2017) for more detailed description of the ray tracing algorithm and test results. Here we give a brief summary of the method. We inject photon packets onto the grid at the position of each source and transport them along radial rays, whose directions are determined by the HEALPix scheme (Górski et al. 2005). As they propagate out, the photon packets are split into sub-rays to ensure that each cell is intersected by at least four rays per source. The optical depths between ray's consecutive intersection points (at grid cell faces) are used to calculate the contribution from stellar sources to the volume-averaged radiation energy density (\mathcal{E}) and flux density (\mathbf{F}) of each cell in each radiation band.

For PE and LW, in addition to radiation from embedded sources we also include diffuse radiation originating outside of the cloud. We use the six-ray approximation (e.g., Glover & Mac Low 2007; Gong et al. 2018) to calculate the shielding of the FUV background. The volume averaged mean intensity in a given cell is computed as

$$J^{\text{bg}} = \frac{I^{\text{bg},0}}{6} \sum_k \frac{e^{-\tau_k} (1 - e^{-\Delta\tau})}{\Delta\tau}, \quad (8)$$

where the index k runs over the six faces of the computational domain, τ_k is the optical depth integrated from the outer boundary to the cell face along the Cartesian axis, and $\Delta\tau = n_{\text{H}}\sigma_{\text{d}}\Delta x$ is the cell optical depth (in the respective energy band, PE or LW). We impose boundary conditions $I_{\text{PE}}^{\text{bg},0} = J_{\text{PE}}^{\text{(ISRF)}} = 1.8 \times 10^{-4} \text{ cm}^{-2} \text{ s}^{-1} \text{ sr}^{-1}$ and $I_{\text{LW}}^{\text{bg},0} = J_{\text{LW}}^{\text{(ISRF)}} = 3.0 \times 10^{-5} \text{ erg cm}^{-2} \text{ s}^{-1} \text{ sr}^{-1}$, where $J^{\text{(ISRF)}}$ is Draine (1978)'s estimate of radiation intensity in the solar neighborhood. We assume $J_{\text{LyC}}^{\text{(ISRF)}} = 0$. We also neglect the (small) contribution to the flux due to the ISRF.

At any location, the angle-averaged intensity in each band is the sum of $c\mathcal{E}/(4\pi)$ with \mathcal{E} computed from ART,

plus the corresponding $J^{\text{(ISRF)}}$ (if any). For notational convenience, we denote the normalized mean intensity in the FUV bands with χ : $\chi_{\text{PE}} \equiv J_{\text{PE}}/J_{\text{PE}}^{\text{(ISRF)}}$, $\chi_{\text{LW}} \equiv J_{\text{LW}}/J_{\text{PE}}^{\text{(ISRF)}}$, and $\chi_{\text{FUV}} = (J_{\text{PE}} + J_{\text{LW}})/(J_{\text{PE}}^{\text{(ISRF)}} + J_{\text{LW}}^{\text{(ISRF)}})$.

The radiative force on the gas in a given cell is computed using a weighted sum of fluxes calculated from the ART,

$$\mathbf{f}_{\text{rad}} = \frac{1}{c} (\kappa_{\text{LyC}} \mathbf{F}_{\text{LyC}} + \kappa_{\text{LW}} \mathbf{F}_{\text{LW}} + 1.25 \kappa_{\text{PE}} \mathbf{F}_{\text{PE}}). \quad (9)$$

In Equation (9), the factor 1.25 for the PE band is an approximate treatment for the additional force that would be exerted by absorption of optical photons (not followed) by dust grains, given the ratio of optical to FUV in the composite spectrum of young clusters.

The LyC energy density is used to calculate the photoionization rate per H atom

$$\zeta_{\text{pi}} = \sigma_{\text{pi}} c \mathcal{E}_{\text{LyC}} / (h\nu_{\text{LyC}}), \quad (10)$$

where c is the speed of light and σ_{pi} is the photoionization cross section.

To model the dissociation of H_2 by LW band photons, it is important to account for the effects of both dust shielding and self-shielding by absorption lines. We employ the self-shielding function of Draine & Bertoldi (1996) assuming a constant Doppler broadening parameter $b = 3 \text{ km s}^{-1}$. This value is the typical one-dimensional velocity dispersion of our simulated clouds, but we note that the shielding factor is insensitive to the choice of b at $N_{\text{H}_2} \gtrsim 10^{17} \text{ cm}^{-2}$ because absorption occurs mainly on Lorentzian damping wings (Sternberg et al. 2014). The evaluation of shielding factor requires that the adaptive ray-tracing follow the column density of molecular hydrogen from each point source to every cell in the computational domain (and similarly for the six-ray approximation). The H_2 photodissociation rate is calculated as

$$\zeta_{\text{pd,H}_2} = \zeta_{\text{pd,H}_2}^{\text{(ISRF)}} \chi_{\text{LW}} f_{\text{shld,H}_2,\text{eff}}, \quad (11)$$

where $\zeta_{\text{pd,H}_2}^{\text{(ISRF)}} = 5.7 \times 10^{-11} \text{ s}^{-1}$ is the dissociation rate for unshielded gas exposed to the ISRF (Heays et al. 2017). The effective self-shielding factor $f_{\text{shld,H}_2,\text{eff}}$ in Equation (11) is the shielding factor averaged over individual point sources and background radiation incident from six boundary faces of the computational domain, weighted by dust-attenuated (continuum) radiation energy density in the LW frequency bin.

Because the threshold wavelengths for C^0 ionization and CO dissociation are about the same as that of the H_2 photodissociation band ($\sim 110 \text{ nm}$) (e.g., Heays et al. 2017), we use the LW radiation χ_{LW} to calculate the ionization rate of C^0 and the equilibrium abundance of CO. we calculate the C^0 -ionizing radiation field accounting

for the self-shielding and cross-shielding by H_2 , following the process described in [Gong et al. \(2017\)](#). For the CO dissociating radiation field, we consider only the dust shielding and ignore the CO self-shielding and shielding by H_2 . The FUV energy density (χ_{FUV}) is used for evaluating the photoelectric heating rate.

2.3. Thermochemistry

The chemical reaction rates and heating/cooling rates have complex dependence on the local gas density, temperature, radiation field, species abundance, dust abundance, and cosmic ray ionization rate. Here we only briefly summarize the physical processes that we include. A full description of our heating/cooling module and test results will be presented in a forthcoming paper (J.-G. Kim et al. 2020, in preparation).

We solve the non-equilibrium evolution of molecular/atomic/ionized hydrogen, while adopting the equilibrium abundances for carbon- and oxygen-bearing species. We adopt gas-phase abundances of C ($x_{\text{C,tot}} = 1.6 \times 10^{-4}$) and O ($x_{\text{O,tot}} = 3.2 \times 10^{-4}$) at solar metallicity and rate coefficients used by the simple chemistry network in [Gong et al. \(2017\)](#). For molecular hydrogen, we include the formation on grain surfaces and destruction by cosmic ray ionization, photodissociation, and photoionization.¹ For ionized hydrogen, we consider the formation by photoionization, cosmic ray ionization, and collisional ionization; and the destruction by radiative and grain-assisted recombination.

The equilibrium abundance of C^+ is determined by balancing radiative, dielectronic, and grain-assisted recombination with photoionization and collisional ionization of C^0 . The abundance of CO is determined by making use of the critical density for the C^0 -to-CO transition that depends on (shielded) χ_{LW} found by [Gong et al. \(2017\)](#). The abundance of neutral hydrogen is determined from the closure $x_{\text{H}^0} = 1 - 2x_{\text{H}_2} - x_{\text{H}^+}$, and the abundance of free electron is set to $x_e = x_{\text{H}^+} + x_{\text{C}^+}$. For the primary cosmic ray ionization rate, we adopt the canonical value $\xi_{\text{cr}} = 2 \times 10^{-16} \text{ s}^{-1}$ found in diffuse molecular clouds (e.g., [Indriolo et al. 2007](#); [Neufeld & Wolfire 2017](#)).

The volumetric heating rate \mathcal{G} is taken as the sum of photoelectric heating, cosmic ray heating, H_2 heating, and photoionization heating. The photoelectric emission from dust by FUV radiation is the dominant heat source in diffuse atomic gas. The heating rate is proportional to χ_{FUV} and is calculated using the functional form provided by [Weingartner & Draine \(2001b\)](#), allowing for a heating efficiency that depends on gas temperature and charging of grains. For the heating by cosmic ray ionization (which is important to FUV-shielded gas), we

adopt fitting formulae suggested by [Draine \(2011b\)](#) for atomic regions and [Krumholz \(2014b\)](#) for molecular regions (see Eqs.(30)–(32) in [Gong et al. \(2017\)](#)). We also include the heating due to H_2 formation on dust grains, photodissociation, and UV pumping, following prescriptions given in [Hollenbach & McKee \(1979\)](#). We assume that the photoionization of H^0 (H_2) deposits an excess energy of 4.4 eV (2.8 eV) per event.

We include cooling by collisionally excited atomic fine-structure levels in C^+ , O^0 , C^0 ; Ly α emission, and recombination of electrons on small grains ([Weingartner & Draine 2001b](#)). We also include cooling by rotational transitions of CO with the large velocity gradient approximation, which becomes the dominant coolant in dense molecular gas. For photoionized gas, we use a temperature- and density-dependent fitting formula that accounts for the cooling by free-free emission, recombination radiation, and cooling by collisionally excited emission lines of heavy elements (Kim, J.-G. et al. 2020, in preparation).

2.4. Numerical Integration

We advance the equations of ideal MHD in time using the Roe Riemann solver, piecewise-linear reconstruction, and a predictor-corrector type time-integrator ([Stone & Gardiner 2009](#)) combined with the constrained transport method ([Gardiner & Stone 2008](#)) that enforces the divergence-free constraint on the magnetic field. We apply diode-like boundary conditions to boundary faces of both the computational domain and the control volumes of sink particles. The Poisson equation is solved via the fast Fourier transform method with open (vacuum) boundary conditions ([Skinner & Ostriker 2015](#)), allowing for the contribution of star particles by using the triangular-shaped cloud method to map point masses to density (ρ_*) on the computational grid ([Gong & Ostriker 2013](#)).

After the updates of the MHD equations, gravity, and sink particles, we perform adaptive ray tracing and six-ray transfer calculations. We then perform the operator-split, explicit update of source terms due to chemical reactions, heating/cooling, and the radiative force. We take substeps in updating the chemical abundances and thermal energy, with the time-step size of each substep chosen as the minimum of 10% of the cooling time ($0.1P/[(\gamma - 1)|\mathcal{G} - \mathcal{L}|]$) and 10% of the chemical time ($0.1/|\mathcal{C}_s|$). In contrast to the previous studies in which the radiative transfer is subcycled alternatingly with the abundance update ([Kim et al. 2017](#)), we perform ray tracing once per MHD update. This approach cannot accurately follow the early evolution of R-type ionization fronts if the front propagation speed is much greater than the maximum signal speed in the computational domain. However, we found that it has little impact on modeling the dynamical expansion of H II regions (Kim, J.-G. et al. 2020 in preparation; see also Figure 6 in [Kim et al. 2017](#)).

¹ We do not include the destruction by collisional dissociation that can be important in high-velocity shocks (e.g., [Hollenbach & McKee 1979](#)).

Table 1. Model parameters

Model	$\alpha_{\text{vir},0}$	$\mu_{\Phi,0}$	$\sigma_{1d,0}$ [km s ⁻¹]	$B_{z,0}$ [μ G]	\mathcal{M}_0	$\mathcal{M}_{A,0}$
(1)	(2)	(3)	(4)	(5)	(6)	(7)
α -series						
A1B2	1.0	2.0	2.1	13.5	13.6	1.3
A2B2	2.0	2.0	2.9	13.5	19.2	1.9
A3B2	3.0	2.0	3.6	13.5	23.5	2.3
A4B2	4.0	2.0	4.1	13.5	27.2	2.7
A5B2	5.0	2.0	4.6	13.5	30.4	3.0
β -series						
A2B05	2.0	0.5	2.9	54.0	19.2	0.5
A2B1	2.0	1.0	2.9	27.0	19.2	0.9
A2B2	2.0	2.0	2.9	13.5	19.2	1.9
A2B4	2.0	4.0	2.9	6.7	19.2	3.8
A2B8	2.0	8.0	2.9	3.4	19.2	7.6
A2Binf	2.0	∞	2.9	0.0	19.2	∞

NOTE—Each model is run with 5 different random seeds for turbulence. All models have the same initial mass $M_0 = 10^5 M_\odot$ and radius $R_0 = 20$ pc. Columns are as follows: (1) model name indicating the initial virial parameter (A) and magnetic flux-to-mass ratio (B). (2) initial virial parameter $\alpha_{\text{vir},0} = 5\sigma_{1d,0}^2 R_0 / (GM_0)$. (4) initial magnetic mass-to-flux ratio $\mu_{\Phi,0} = 2\pi\sqrt{G}\Sigma_0 / |B_{z,0}|$. (3) initial velocity dispersion. (5) initial magnetic field strength. (6) 3D sonic Mach number of initial turbulence. (7) 3D Alfvén Mach number of initial turbulence.

2.5. Model Initialization and Parameters

We initialize the simulation by placing a uniform density cloud with mass $M_0 = 10^5 M_\odot$ and radius $R_0 = 20$ pc at the center of the computational domain, which has a side length $L_{\text{box}} = 4R_0 = 80$ pc. The number of grid cells is set to 256^3 corresponding to the uniform grid spacing of $\Delta x = 0.31$ pc. The cloud has the initial gas surface density $\Sigma_0 \equiv M_0 / (\pi R_0^2) = 79.6 M_\odot \text{ pc}^{-2}$, hydrogen number density $n_{\text{H},0} = 3M_0 / (4\pi R_0^3 \mu_{\text{H}} m_{\text{H}}) = 86.2 \text{ cm}^{-3}$, and freefall time

$$t_{\text{ff},0} = \left(\frac{3\pi}{32G\rho_0} \right)^{1/2} = 4.68 \text{ Myr.} \quad (12)$$

The gas temperature is set to 24 K and the H₂ abundance to the equilibrium value $x_{\text{H}_2} = 0.43$, appropriate for UV-shielded gas with $\xi_{\text{cr}} = 2.0 \times 10^{-16} \text{ s}^{-1}$ (see Equations (15)–(18) in Gong et al. 2018). The ambient medium is a warm neutral medium with $n_{\text{H}} = 10^{-2} n_{\text{H},0}$ and $T = 8200$ K and has a total mass of $0.16M_0$. We

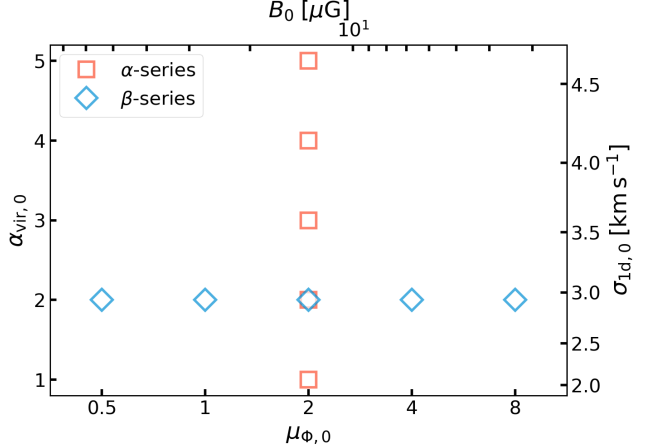


Figure 1. Parameters of simulated clouds in α - and β -series models (see also Table 1). All clouds have the same mass $M_0 = 10^5 M_\odot$ and radius $R_0 = 20$ pc. The bottom x -axis is the mass-to-magnetic flux ratio $\mu_{\Phi,0} = 2\pi\sqrt{G}\Sigma_0 / |B_{z,0}|$ and the left y -axis is the kinetic virial parameter $\alpha_{\text{vir},0} = 5R_0\sigma_{1d,0}^2 / (GM_0)$. The top x -axis and right y -axis show the corresponding magnetic field strength $B_{z,0}$ and one-dimensional turbulent velocity dispersion $\sigma_{1d,0}$, respectively. For each pair of $(\alpha_{\text{vir},0}, \mu_{\Phi,0})$, we run five simulations with different random seeds for initial turbulent velocity field.

note that we have tested the effects of the initial temperature choice, and found that they are unimportant as thermal and ionization equilibrium are rapidly achieved.

We assign the gas that is initially molecular a passive scalar field value $s_{\text{cl}} = 1$ and the ambient atomic gas with $s_{\text{cl}} = 0$. We use s_{cl} to differentiate the “cloud material” from the ambient medium, but it should be noted that the use of a passive scalar cannot serve as a perfect surrogate for the Lagrangian tracer particle due to numerical diffusion. For analysis, we select gas that is neutral and initially molecular by using a filter function

$$\Theta = \begin{cases} 1, & \text{if } x_{\text{H}^+} < 0.5 \text{ and } s_{\text{cl}} > 10^{-2} \\ 0, & \text{otherwise.} \end{cases} \quad (13)$$

We initiate all clouds (except the non-magnetized model) with a uniform magnetic field aligned along the z -axis. We note that a uniform magnetic field exerts no Lorentz force and does not play a role in supporting the cloud at $t = 0$, but the nonuniform magnetic fields created by the turbulence provide support against gravity from the early stages of evolution. The initial magnetic field strength is measured by the dimensionless mass-to-magnetic flux ratio

$$\mu_{\Phi,0} = \frac{2\pi\sqrt{G}\Sigma_0}{B_{z,0}} \quad (14)$$

which is defined such that global gravitational collapse is suppressed in subcritical clouds with $\mu_{\Phi,0} \lesssim 1$, i.e.,

where the mass-to-flux ratio exceeds the critical value² $(2\pi\sqrt{G})^{-1}$. The parameter $\mu_{\Phi,0}^2$ is equal to 2/5 of the ratio between the initial gravitational energy and magnetic energy of the cloud.

All simulations are initialized with a Gaussian-random turbulent velocity field with a power spectrum $|\delta\mathbf{v}_k|^2 \propto k^{-4}$ for $2 \leq 2\pi/L_{\text{box}} \leq 64$. The corresponding structure function has velocity dispersion increasing with scale as $\sigma(\ell) \propto \ell^{1/2}$, consistent with observations of GMCs (Heyer & Brunt 2004). We use the kinetic virial parameter

$$\alpha_{\text{vir},0} = \frac{5\sigma_{1d,0}^2 R_0}{GM_0} \quad (15)$$

for an isolated, uniform, spherical cloud (Bertoldi & McKee 1992) to quantify the level of initial turbulent support, where $\sigma_{1d,0}$ is the mass-weighted one-dimensional velocity dispersion averaged over the whole cloud. The parameter $\alpha_{\text{vir},0}$ is equal to twice the initial kinetic energy divided by the initial gravitational energy of the cloud. We note that even with a given value of $\sigma_{1d,0}$ and given power spectrum, the velocity amplitudes of individual modes differ (and therefore the cloud evolution differs) depending on the random seeds selected.

For $M_0 = 10^5 M_{\odot}$, $R_0 = 20$ pc and isothermal sound speed $c_{s,\text{iso}} = 0.26$ km s $^{-1}$, the initial Alfvén speed in the cloud can be written in terms of $\mu_{\Phi,0}$ as $v_A = B_{z,0}/\sqrt{4\pi\rho_0} = 5.3\mu_{\Phi,0}^{-1}$ km s $^{-1}$. The 3D sonic and Alfvén Mach numbers of the initial turbulence are then $\mathcal{M}_0 = \sigma_{3d,0}/c_{s,\text{iso}} = 13.6\alpha_{\text{vir},0}^{1/2}$, $\mathcal{M}_{A,0} = \sigma_{3d,0}/v_A = 0.67\alpha_{\text{vir},0}^{1/2}\mu_{\Phi,0}$, respectively. The plasma beta parameter in the cloud is $\beta_0 = P/P_{\text{mag}} = 2c_{s,\text{iso}}^2/v_A^2 = 4.9 \times 10^{-3}\mu_{\Phi,0}^2$.

To investigate the effects of the initial virial parameter and the magnetic field strength, we consider α - and β -series models, in which either the initial kinetic or magnetic energy is held constant, while the other changes. This is equivalent to holding either $\alpha_{\text{vir},0}$ (or $\sigma_{1d,0}$) fixed or holding $\mu_{\Phi,0}$ (or $B_{z,0}$ or β) fixed, as depicted in Figure 1. In the α -series, we vary $\alpha_{\text{vir},0}$ from 1 to 5, while the initial magnetic field is set to $B_{z,0} = 13.5\mu\text{G}$, corresponding to $\beta_0 = 0.02$ and $\mu_{\Phi,0} = 2$. In the β -series, we vary μ_{Φ} from 0.5 to 8 (by factors of two), while holding $\alpha_{\text{vir},0} = 2$ (corresponding to $\sigma_{1d,0} = 2.93$ km s $^{-1}$). We also consider the non-magnetized case with $\mu_{\Phi,0} = \infty$. All model parameters are listed in Table 1. Our chosen parameter range for $\alpha_{\text{vir},0}$ encompasses the observational estimates of average α_{vir} for molecular clouds in the Milky Way and nearby galaxies (e.g., Miville-Deschénes et al. 2017; Sun et al. 2018, 2020b). Except for the subcritical case $\mu_{\Phi,0} = 0.5$ (which we include for theoretical completeness), the range of magnetic field

strength is also consistent with the range of observed values in inter-core regions of nearby molecular clouds (a few μG – $30\mu\text{G}$) inferred from OH Zeeman observations (Thompson et al. 2019).

For each model we run five simulations with different random seeds for the initial turbulent velocity field. This allows us to study the variations of star formation history and cloud destruction outcomes that result from different turbulence realizations.

The name of each simulation is designated as **AaBbSs**, where **a**, **b**, and **s** respectively denote $\alpha_{\text{vir},0}$, $\mu_{\Phi,0}$, and the label of the set of random seeds used for initializing turbulence (**seed**). We choose the run with $\alpha_{\text{vir},0} = 2$, $\mu_{\Phi,0} = 2$, and **seed** = 4 as the fiducial case, for which we run additional simulations at higher ($N_{\text{cell}} = 512^3$) and lower ($N_{\text{cell}} = 128^3$) resolutions to check the numerical convergence.

3. RESULTS

3.1. Evolution of the Fiducial Model

We first sketch out the evolution of the fiducial model **A2B2S4** with $(\alpha_{\text{vir},0}, \mu_{\Phi,0}) = (2, 2)$. Figure 2 shows the volume rendering of molecular (blue), atomic (green), and ionized (red) gas of the fiducial model at times $t' \equiv t - t_{*,0} = 1$ Myr, 3 Myr, 5 Myr, and 8 Myr, where $t_{*,0} = 3.3$ Myr denotes the time at which the first star formation occurs. Magnetic field lines are visualized by lines (colored by magnitude) and star particles by spheres (colored by t_{age}). Projections of density for snapshots at $t' = -0.2, 2, 5, 8$ Myr of this model are also seen in the comparison figures of Appendix B.

The overall evolutionary sequence is similar to that of the hydrodynamic simulations presented in Kim et al. (2018, 2019b). The compression of gas by supersonic turbulence creates a network of dense filaments that have some preference for alignment perpendicular to the direction of the large-scale magnetic field. It also gives rise to a density probability density function (PDF) that is approximately log-normal in shape and develops a high-density tail as time progresses. At $t = 3.3$ Myr $\equiv t_{*,0}$, the densest part of a filament collapses and forms the first sink particle.

Ionizing radiation from the first sink particle creates a compact and confined H II region, and the pressure of photoionized gas and (subdominant) radiation pressure force drive its dynamical expansion, suppressing further gas accretion. Once the H II region breaks out of the local star-forming clump, ionized gas quickly fills the bulk of the computational volume, and more and more UV photons escape the computational domain through optically-thin sight lines. Pre-existing dense structures are carved into pillars and cometary globules and rocket away from ionizing sources due to anisotropic ablation, as seen in other simulations of expanding H II regions in turbulent clouds (e.g., Mellema et al. 2006; Gritschneider et al. 2010; Arthur et al. 2011; Ali et al. 2018). Until $t' \approx 5$ Myr, stellar mass continues to increase, multi-

² The numerical factor $1/(2\pi) \simeq 0.16$ is exact for an infinite cold sheet (Nakano & Nakamura 1978), but a spherical cold cloud has a similar value of 0.17 (Tomisaka et al. 1988).

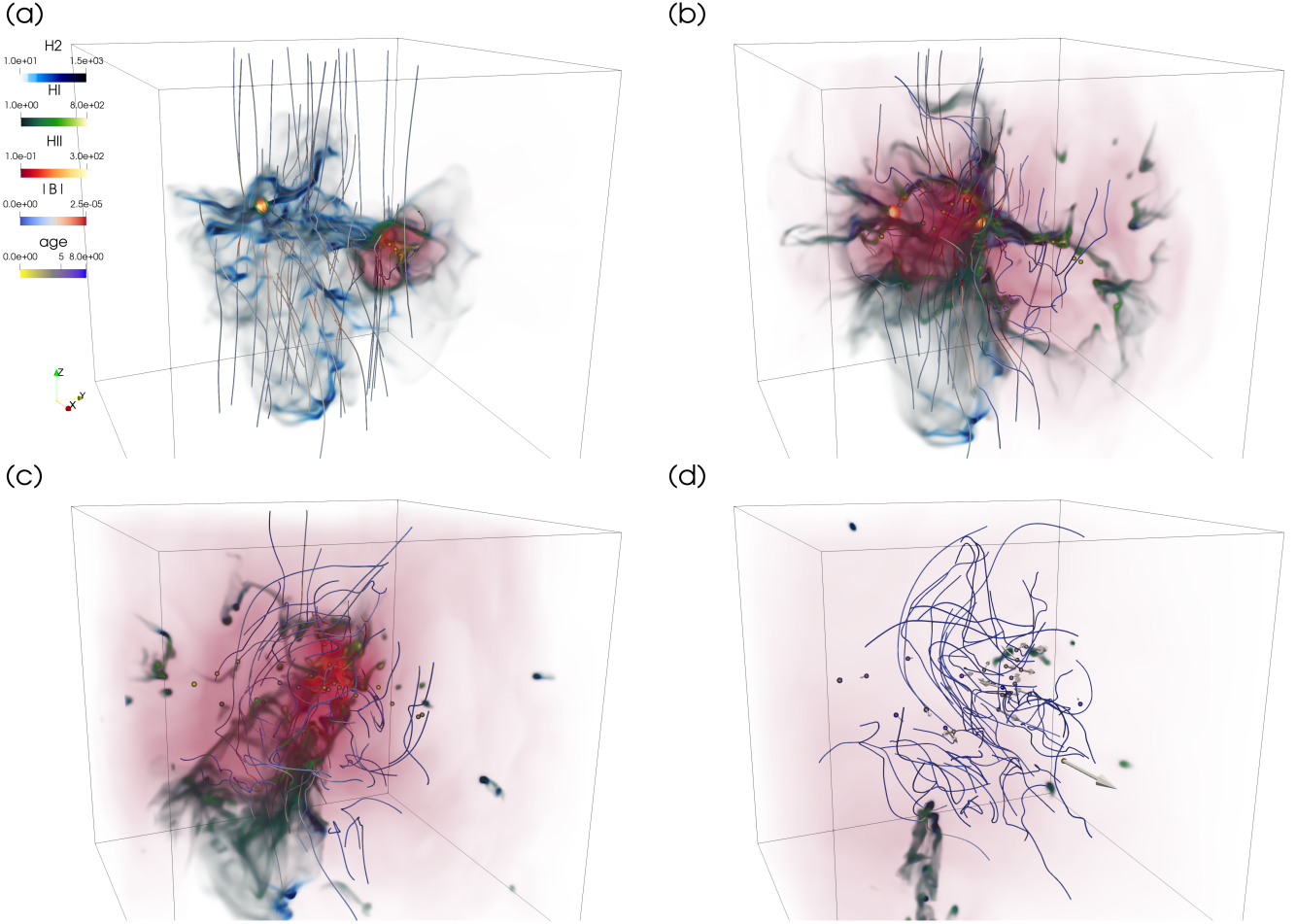


Figure 2. Volume rendering of molecular (blue-white), atomic (green-white), and ionized (red-orange) gas for the fiducial model A2B2S4 ($\alpha_{\text{vir},0} = 2$, $\mu_{\Phi,0} = 2$, $\text{seed} = 4$) at resolution of 256^3 . Panels show snapshots at (a) $t = t_{*,0} + 1, (b) $t_{*,0} + 3, (c) $t_{*,0} + 5, and (d) $t_{*,0} + 8, where $t_{*,0} = 3.3 is the time of first star formation. Magnetic fields are shown as lines (colored by magnitude) and star particles are shown as spheres (colored by t_{age}). In the bottom right panel, the arrows indicate the velocity of star particles.$$$$$

ple subclusters form, and H II regions merge with each other.

A substantial fraction of molecular gas at the periphery of the H II region turns into the atomic phase by dissociating radiation and then into ionized phase by ionizing radiation. Only 5% of the initial cloud mass remains molecular in the swept-up gas at $t' = 8. The main group of particles are found in the second quadrant of the x - y plane, moving outward at a few km s^{-1} , as indicated by arrows in the bottom right panel of Figure 2.$

Figure 3(a) shows the temporal evolution of the gas and stellar mass in the fiducial model.³ The stellar mass growth (blue) is roughly linear in time and 90% of the total star formation is complete at $t' = 5.7$ Myr.

The net SFE (or lifetime/integrated/final SFE) is $\varepsilon_* = M_{*,\text{final}}/M_0 = 0.058$. Photodissociation is efficient at depleting molecular gas mass: at $t' = 3.6$ Myr, the mass of molecular hydrogen is only $0.36M_0$ and the mass of atomic hydrogen increases to $0.33M_0$. The dashed lines show the outflow cloud gas mass that has left the computational domain as neutrals (black) and ions (green). Most (72%) of the cloud mass is photoevaporated and ejected as ions, consistent with the findings from hydrodynamic simulations of Kim et al. (2018). In addition, 22% of the initial cloud is driven out as neutrals (9% molecular). We note that even without radiation feedback, a small fraction ($\sim 0.1M_0$) of neutrals would have been ejected; this is the portion of gas that is unbound from the initial turbulence (Raskutti et al. 2016).

In Figure 3(b) we present the evolution of the cluster luminosity in LyC and FUV (LW+PE) frequency bins for the fiducial model. The LyC (FUV) luminosity keeps increasing until $t' = 4.6$ Myr (6.0 Myr) at which point

³ Only gas that was originally part of the cloud is shown, selected, e.g., as $M_{\text{H}_2} = \int 2n_{\text{H}_2}\mu_{\text{H}}m_{\text{H}}s_{\text{cl}}dV$ where s_{cl} is the passive scalar for the initial cloud.

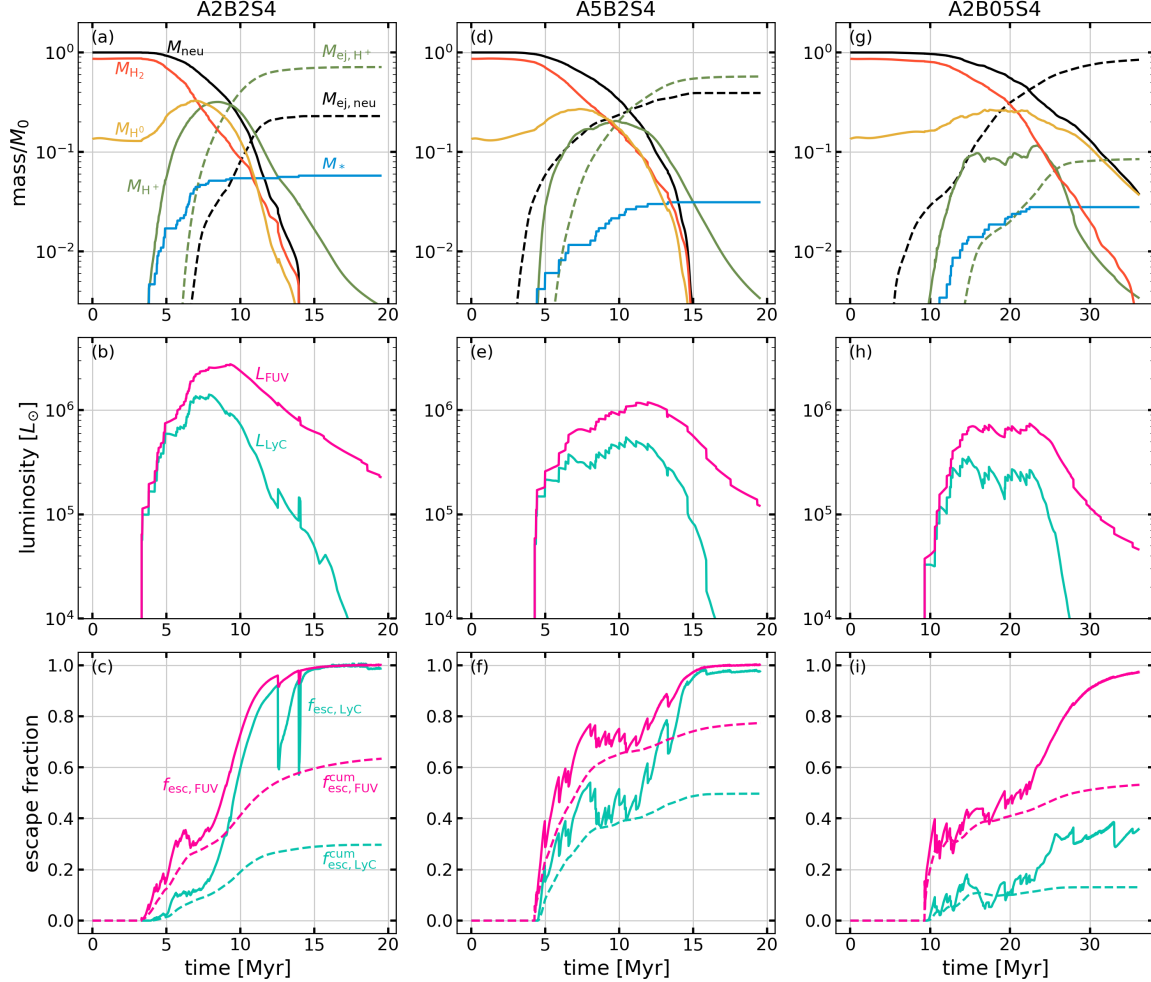


Figure 3. Time evolution of global quantities in three different models: (left) the fiducial model A2B2S4 with $(\alpha_{\text{vir},0}, \mu_{\Phi,0}) = (2, 2)$; (middle) a highly unbound cloud A5B2S4 with $(\alpha_{\text{vir},0}, \mu_{\Phi,0}) = (5, 2)$; (right) a magnetically subcritical cloud A2B05S4 with $(\alpha_{\text{vir},0}, \mu_{\Phi,0}) = (2, 0.5)$. The three clouds have identical initial turbulent velocity field realizations (`seed` = 4), but with different normalization for $\alpha_{\text{vir},0} = 2, 5$. (Top) Stellar mass (M_*), cloud gas mass in molecular (M_{H_2}), atomic (M_{H^0}), and ionized (M_{H^+}) phases. The dashed lines show the cumulative gas mass that has left the simulation domain as neutrals ($M_{\text{ej, neu}}$; black) and ions ($M_{\text{ej, H}^+}$; green). (Middle) Luminosities of ionizing (LyC; cyan) and non-ionizing (FUV; magenta) photons. (Bottom) Instantaneous (solid) and cumulative (dashed) escape fractions of ionizing and non-ionizing photons.

$$Q_{\text{LyC}} = L_{\text{LyC}}/\hbar\nu_{\text{LyC}} = 1.9 \times 10^{50} \text{ s}^{-1} \quad (L_{\text{FUV}} = 2.8 \times 10^6 L_{\odot})$$

Figure 3(c) shows LyC and FUV escape fractions for the fiducial model. Instantaneous escape fractions $f_{\text{esc}}(t) = L_{\text{esc}}(t)/L(t)$ are plotted as solid lines while the cumulative (or luminosity-weighted, time-averaged) escape fractions $f_{\text{esc}}^{\text{cum}}(t) = \int_{t_{0,*}}^t L_{\text{esc}}(t')dt'/\int_{t_{0,*}}^t L(t')dt'$ are shown as dashed lines. Overall, both the instantaneous and cumulative escape fractions keep increasing with time.⁴ The cumulative escape fractions measured at $t' = 3$ Myr are 6.3% and 24% for LyC and FUV ra-

diation, but they become as large as 30% and 63% at the end of the simulation ($t = 19.6$ Myr). As we shall show, except for the magnetically subcritical clouds in which the evolutionary timescale is significantly longer than the lifetime of radiation sources, most of LyC radiation escapes in the first 5 Myr after the star formation.

Figure 4 depicts maps of emission measure (EM = $\int n_e^2 d\ell$) from ionized gas projected along the y -axis, with snapshots from the fiducial model at $t' = 1, 3, 5, 8$ Myr shown in the left column of panels. Also overlaid (white contours) are the loci where $A_V = 1$ ($N_{\text{H}} = 1.87 \times 10^{21} \text{ cm}^{-2}$) in the neutral gas, outlining the overall projection of the cloud. Although at $t' = 1$ Myr the H II region remains relatively confined, it has already broken out of the cloud. Over the next several Myr the region of high EM rapidly expands to cover the

⁴ The downward spikes of f_{esc} at $t = 12.5$ Myr and $t = 14.0$ Myr are due to the formation of sinks in the swept up gas near the computational boundary.

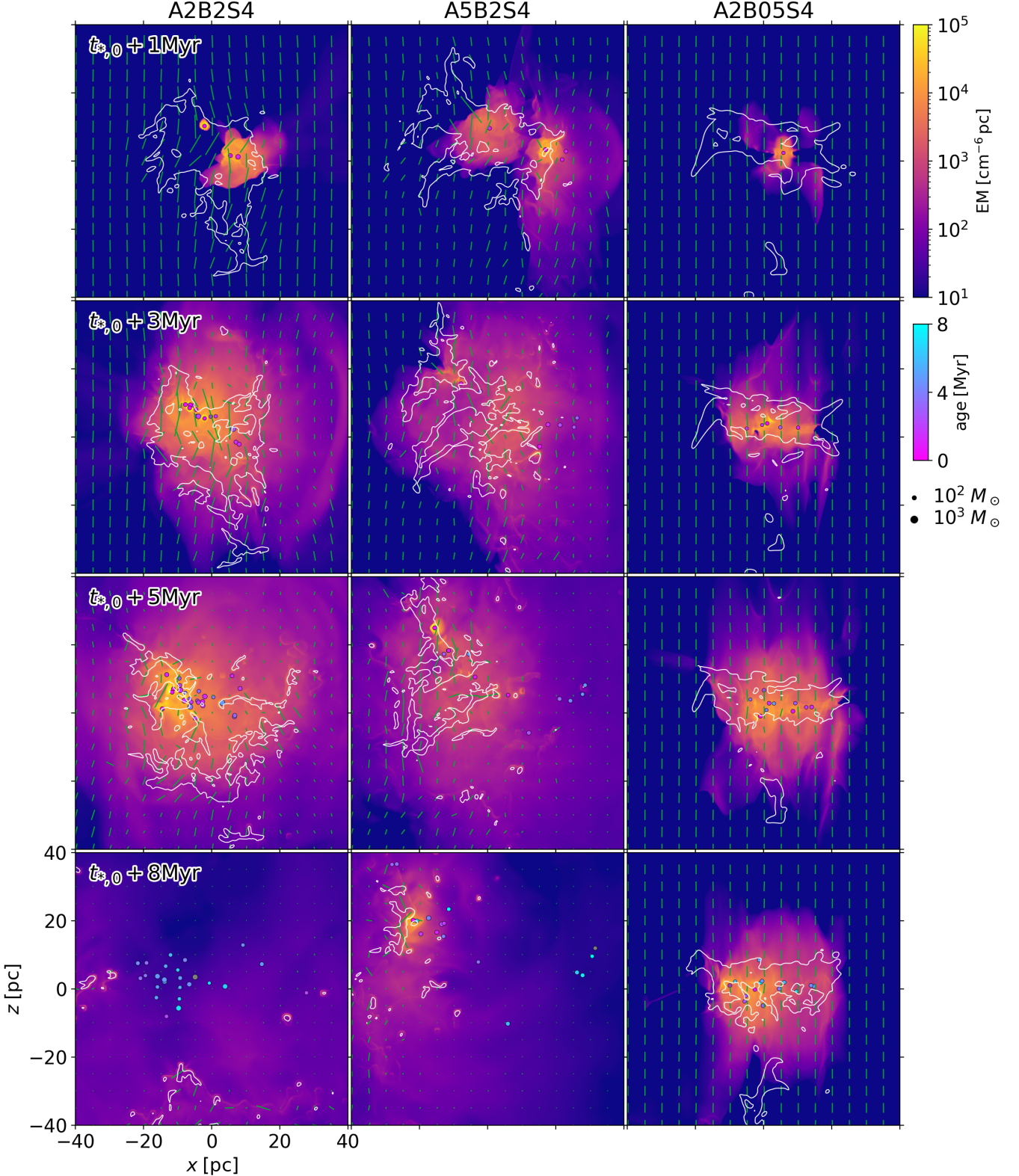


Figure 4. Emission measure along the y -axis of three different models (A2B2S4, A5B2S4, and A2B05S4) at times (from top to bottom) $t' = 1, 3, 5, 8$ Myr after the onset of star formation. Green line segments indicate the polarization vectors of dust thermal emission rotated by 90° , indicating the direction of magnetic field. The length of the segment is proportional to the magnitude and is normalized by the initial magnetic field $B_{z,0}$. White contours show the loci where $A_V = 1$, corresponding to column density of neutral (atomic + molecular) hydrogen gas $1.87 \times 10^{21} \text{ cm}^{-2}$ ($21.4 M_\odot \text{ pc}^{-2}$).

area of the neutral cloud and beyond. The coincidence between high EM and $A_V > 1$ suggests that bright H α and CO gas would overlap for several Myr until the cloud is substantially dispersed, as seen in observations (e.g., Schinnerer et al. 2019; Chevance et al. 2020b).

Figure 4 includes overlaid line segments indicating the magnetic field orientation in the x - z plane obtained from synthetic maps of Stokes Q and U parameters of polarized dust emission, assuming a spatially constant dust temperature, opacity, and intrinsic polarization fraction (e.g., Kim et al. 2019a). The length of a segment indicates the magnetic field strength normalized by the initial field strength $B_{0,z}$.

At early times a fraction of the initial kinetic energy is converted into turbulent magnetic fields. The magnetic intensity in neutral gas increases (sublinearly) with density and becomes as high as $\sim 10^2 \mu\text{G}$ in densest ($n_{\text{H}} \sim 10^4 \text{ cm}^{-3}$) regions. While the large-scale magnetic field orientation remains unchanged before significant gas dispersal, the small-scale magnetic field fluctuates and its orientation exhibits deviation from the large-scale orientation. Regions of higher and lower fractional polarization also reflect the facts the parallel component of the magnetic field strength is enhanced across shock fronts, but it is weakened significantly across ionization fronts after the onset of star formation (e.g., Redman et al. 1998; Draine 2011b; Kim & Kim 2014).

The evolution of a cloud's size and velocity dispersion reflect its dynamical evolution, both before and after the onset of radiation feedback. There are many ways to compute cloud size⁵, but here we define the effective cloud radius as $R = 2^{1/3}R_{50\%}$, where $R_{50\%}$ is the half-mass radius of the neutral gas and the factor $2^{1/3}$ applies to a homogeneous sphere ($R = R_0$ at $t = 0$). The mass-weighted, line-of-sight velocity dispersions are measured along the Cartesian axes $\sigma_{1\text{d},i}^2 = \int \rho(v_i - \bar{v}_i)^2 \Theta dV / \int \rho dV$, where \bar{v}_i is the mean velocity (see Equation (13) for definition of Θ , which selects only neutral “cloud” gas). Because the gas motion is anisotropic in the presence of strong magnetic field, we consider the velocity dispersions perpendicular and parallel to the z -axis and their average separately:

$$\sigma_{1\text{d},\parallel} = \sigma_{1\text{d},z}, \quad (16)$$

$$\sigma_{1\text{d},\perp} = \frac{1}{\sqrt{2}} (\sigma_{1\text{d},x}^2 + \sigma_{1\text{d},y}^2)^{1/2}, \quad (17)$$

$$\sigma_{1\text{d}} = \frac{1}{\sqrt{3}} (\sigma_{1\text{d},x}^2 + \sigma_{1\text{d},y}^2 + \sigma_{1\text{d},z}^2)^{1/2}. \quad (18)$$

The time evolution of R and of $\sigma_{1\text{d}}$, $\sigma_{1\text{d},\parallel}$, and $\sigma_{1\text{d},\perp}$ for the fiducial model are shown in Figure 5(a) and (b). We show the time evolution until $t_{*,90\%}$, the time at

which 90% of the final stellar mass has been assembled. The time of the first star formation is indicated by grey dashed vertical lines. Although gas in the cloud is compressed internally by turbulence and gravity, the overall cloud size changes very little until $t' \sim 5$ Myr, when feedback begins to dominate the evolution. The decrease of velocity dispersion before $t = t_{*,0}$ reflects the rapid decay of turbulence within a flow crossing time (e.g., Ostriker et al. 2001), but the level of the velocity dispersion begins to increase after $t' \sim 0.5$ Myr due to expanding motions induced by the radiation feedback. The velocity dispersion becomes weakly anisotropic after $t > 6$ Myr.

Evolution of individual energies and their ratios are shown for the fiducial model in Figure 5(c) and (d); these will be discussed in detail in Section 3.8. Here, we simply note that as expected, the cloud's gravitational energy ($|\mathcal{W}|$) is near constant at first and then declines (mirroring evolution of the cloud radius R), while kinetic energy (\mathcal{T}_{kin}) initially drops and then increases (tracking the velocity dispersion). Magnetic energy (\mathcal{B}) at first increases as magnetic turbulence is driven, and then declines as the cloud is dispersed.

3.1.1. PDFs of Density, Radiation, and Pressure

The gas in our simulations is found in a range of physical conditions. Figure 6 shows the mass-weighted PDF in the density (n_{H}) and radiation intensity (χ_{FUV} or \mathcal{E}_{LyC}) plane at times $t' = -0.2, 2, 5, 8$ Myr. The top row shows the PDF of the entire gas, while the other rows select gas in molecular ($2x_{\text{H}_2} > 0.5$; blue), neutral atomic ($x_{\text{H}^0} > 0.5$; green), and ionized ($x_{\text{H}^+} > 0.5$; orange) phases. In the top three rows of Figure 6, we show the distribution in the $n_{\text{H}}-\chi_{\text{FUV}}$ plane; in the bottom row we plot the distribution in the $n_{\text{H}}-\mathcal{E}_{\text{LyC}}$ plane. Similarly, Figure 7 shows mass-weighted PDFs in the density and pressure (P/k_{B}) plane.

Before the onset of massive star formation ($t_{*,0} - 0.2$ Myr panels), gas is subject to the background FUV radiation only. The ambient gas is optically thin, and is therefore exposed to the ISRF with $0.8 \lesssim \chi_{\text{FUV}} \leq 1$; it has low density and is in the warm ($T \sim 8000$ K) atomic phase. The width of the density PDF of the ambient warm gas is narrow as subsonic.

The cold, dense gas in the cloud is subject to a range of FUV intensity and becomes increasingly shielded at higher density. Most of the cloud is molecular, as seen in the PDFs in the middle two rows. For the fiducial cloud, we compute the mass-weighted mean FUV intensity in each density bin for snapshots before the first star formation. In the left panel of the second row in Figure 6, the black line shows the time-averaged mean FUV intensity $\chi_{\text{FUV},\text{avg}}$, with the error bars indicating the standard deviation. We find that $\chi_{\text{FUV},\text{avg}}$ has weak temporal variation and is well described by a local shielding approximation. The red dashed line shows that the average FUV radiation field in molecular gas with $n_{\text{H}} > 1 \text{ cm}^{-3}$ is well fit by the function $\chi_{\text{FUV},\text{avg}} = 0.9e^{-\tau_{\text{FUV},\text{eff}}}$, where

⁵ We have also considered the rms distance from the center of gas mass, as well as the effective radius $[3 \int \Theta dV / (4\pi)]^{1/3}$, and found similar results.

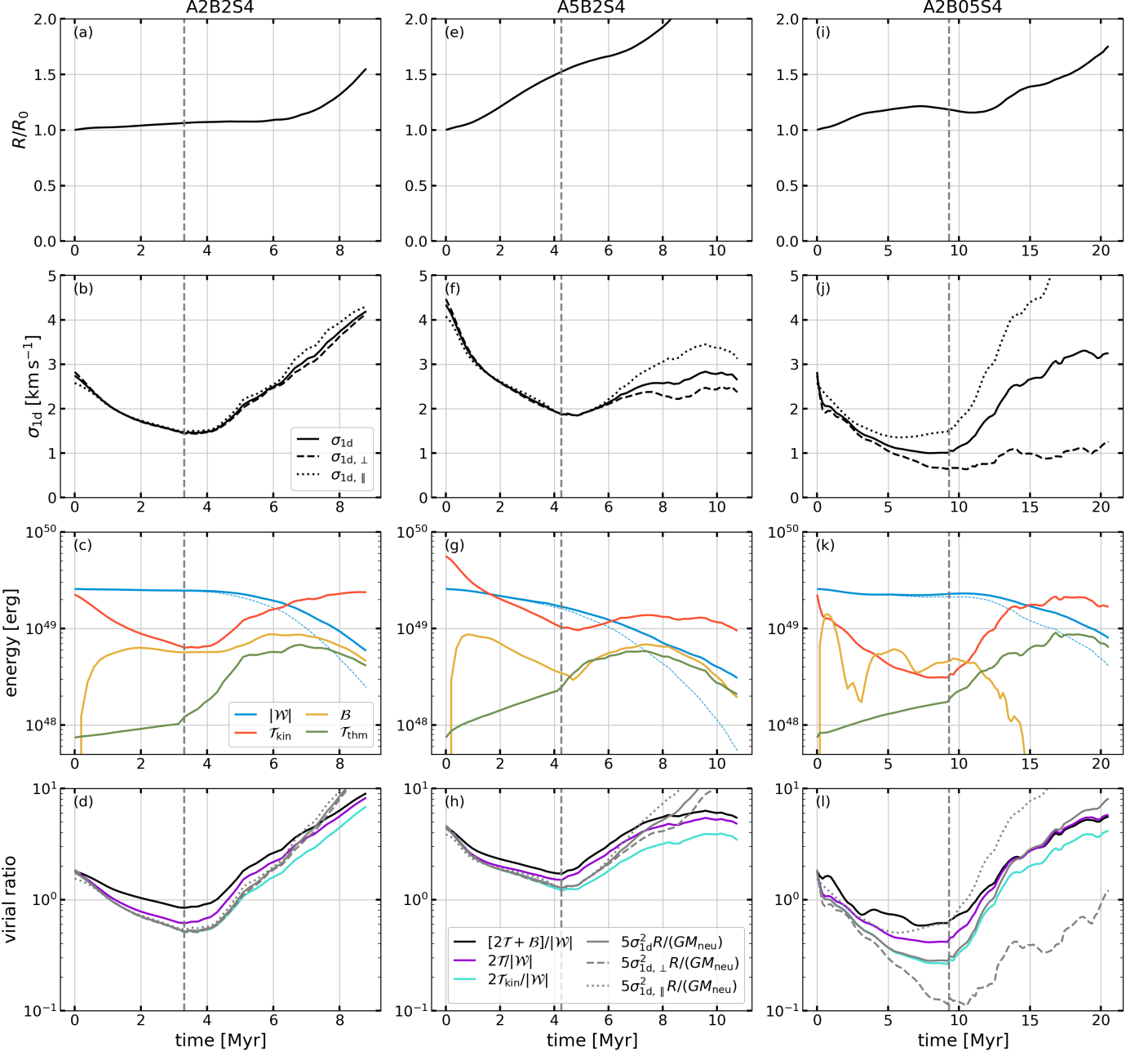


Figure 5. Time evolution of cloud size, velocity dispersion, energy, and virial ratios for three different models A2B2S4, A5B2S4, and A2B05S4 until $t_{*,90\%}$, when 90% of the final stellar mass has been formed. The grey dashed vertical lines indicate the time of first star formation. (Top row) The effective radius of neutral cloud $R = 2^{1/3} R_{50\%}$, where $R_{50\%}$ is the half-mass radius. (Second row) Velocity dispersion measured perpendicular ($\sigma_{1d,\perp}$) and parallel ($\sigma_{1d,\parallel}$) to the background magnetic field, and averaged over all directions (σ_{1d}). (Third row) Gravitational ($|\mathcal{W}|$, blue), kinetic (\mathcal{T}_{kin} , red), thermal (\mathcal{T}_{thm} , green), and magnetic (\mathcal{B} , yellow) energies (see Equations (21)–(24)). A simple estimate of gravitational energy is also shown (blue dashed). (Fourth row) The kinetic virial parameter $\alpha_{\text{vir}} = 5\sigma_{1d}^2 R/(GM_{\text{neu}})$ for different viewing angles (gray lines) and various energy ratios.

the density-dependent optical depth is

$$\tau_{\text{FUV,eff}} = 1.8 \left(\frac{n_{\text{H}}}{10^2 \text{ cm}^{-3}} \right)^{0.30}. \quad (19)$$

That is, the effective optical depth increases sub-linearly with density, such that if we define $\tau_{\text{FUV,eff}} \equiv$

$\sigma_{\text{d}} n_{\text{H}} L_{\text{shld}}$, this corresponds to the shielding length of $L_{\text{shld}} \sim 6$ pc when $n_{\text{H}} = 10^2 \text{ cm}^{-3}$.

Based on this result, we calculate the equilibrium chemical abundances and temperature of molecular gas as a function of n_{H} assuming constant $\xi_{\text{cr}} = 2 \times 10^{-16} \text{ s}^{-1}$, and density-dependent FUV intensity

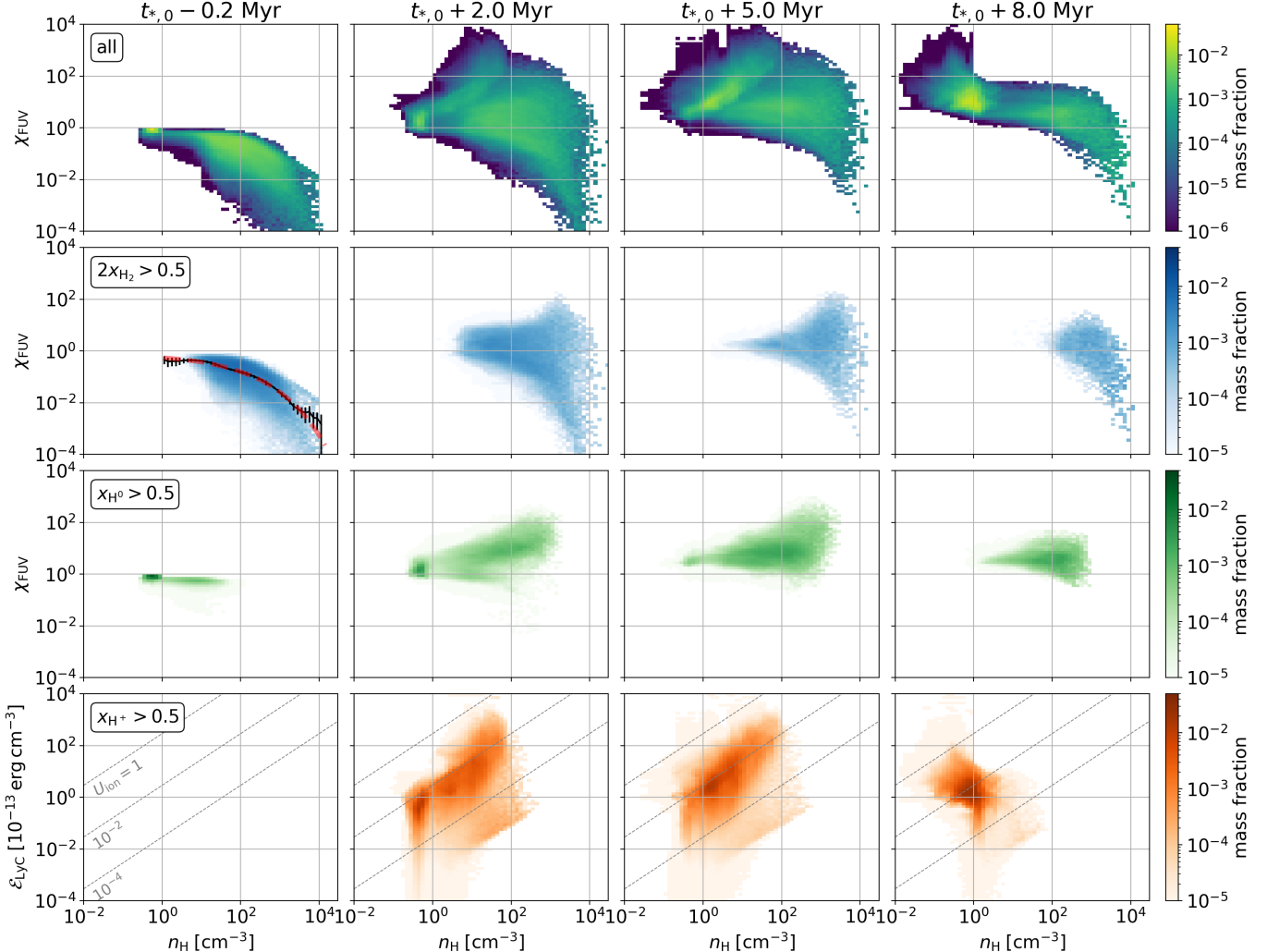


Figure 6. Mass-weighted PDFs of radiation intensity and density for the fiducial model (A2B2S4). at times, from left to right, $t_{*,0} - 0.2$ Myr, $t_{*,0} + 2$ Myr, $t_{*,0} + 5$ Myr, $t_{*,0} + 8$ Myr, where $t_{*,0}$ is the time of first star formation. From top to bottom, rows show the PDF of all gas, mostly-molecular gas ($2x_{H_2} > 0.5$), mostly-atomic gas ($x_{H^0} > 0.5$), and mostly-ionized gas ($x_{H^+} > 0.5$). The top three panels show the intensity in the FUV band, while the bottom row shows the intensity in the LyC band. In the left panel of the second row, the black line with error bars shows the mass-weighted average FUV intensity in molecular gas before $t_{*,0}$. This density-dependent attenuation of the ISRF is well fit by Equation (19), shown as the red dashed line. The gray dashed diagonal lines in the bottom row are the loci of constant ionization parameters (top to bottom) $U = \mathcal{E}_{\text{LyC}} / (n_{\text{H}} h \nu_{\text{LyC}}) = 1, 10^{-2}, 10^{-4}$.

$\chi_{\text{FUV,avg}}$. We also calculate the equilibrium curve for unshielded atomic gas assuming $\xi_{\text{cr}} = 2 \times 10^{-16} \text{ s}^{-1}$, $\chi_0 = 1$, and $\tau_{\text{FUV,eff}} = 0$. The gray dashed lines in center rows of Figure 7 show the resulting equilibrium curves. The low-density molecular gas with $10 \text{ cm}^{-3} < n_{\text{H}} < 10^3 \text{ cm}^{-3}$ exhibits a range of temperature $20 \text{ K} < T < 100 \text{ K}$, while the high-density molecular gas for which the heating is dominated by cosmic ray ionization has a constant temperature of $\sim 20 \text{ K}$

(blue diagonal lines in Figure 7).⁶ The thermal pressure of the atomic and diffuse molecular gas ranges from $P/k_{\text{B}} \sim 10^3 - 10^4 \text{ cm}^{-3} \text{ K}$, while it can be as high as $\sim 2 \times 10^5 \text{ cm}^{-3}$ at the density of sink particle formation ($\sim 2 \times 10^4 \text{ cm}^{-3}$).

⁶ In reality, the cosmic ray ionization rate may be significantly attenuated within dense molecular gas (e.g. Neufeld & Wolfire 2017), leading to lower gas temperature. However, for practical purposes the thermal energy density is already extremely low compared to kinetic and magnetic energy densities.

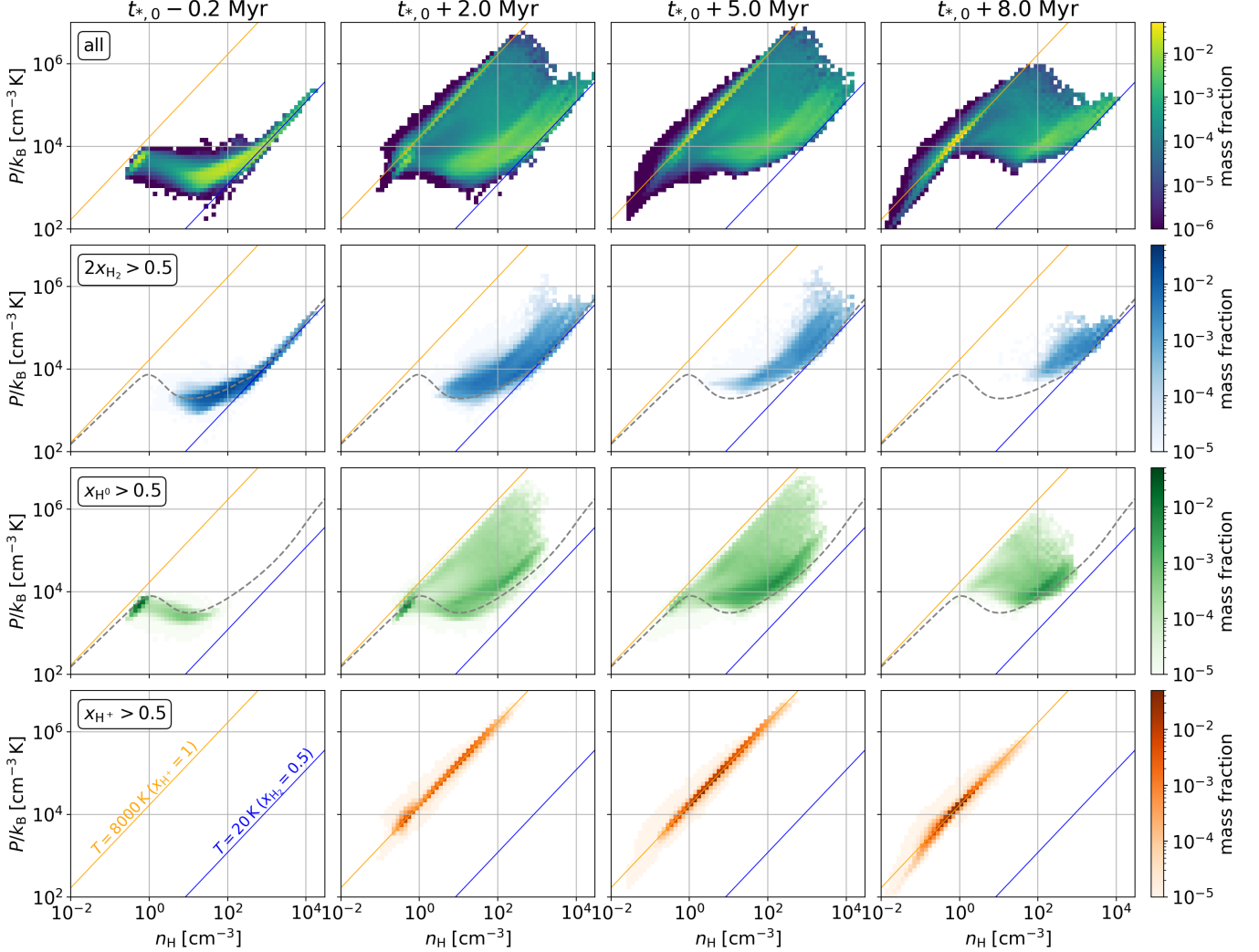


Figure 7. Mass-weighted PDF of thermal pressure and density of the fiducial model (A2B2S4). Temporal snapshots and gas phases are as in Figure 6. The blue and orange diagonal lines show constant temperature 20 K and 8000 K for fully molecular ($x_{H_2} = 0.5$) and ionized ($x_{H^+} = 1$) gas. In the second and third rows, the grey dashed lines plot the equilibrium pressure expected for gas exposed to the background UV radiation with density-dependent shielding (see text for details).

At $t' > 0$, both neutrals and ions are subject to intense UV radiation from newborn stars, and the normalized FUV radiation intensity can be as high as $\chi_{\text{FUV}} \sim 10^2$ in the photon dominated region (PDR). ⁷ The temperature of (unshielded) dense molecular/atomic gas in the PDR is significantly elevated because of enhanced heating, but most of the gas is still shielded and remains cold, at $T \sim 20\text{-}100$ K. The photoionized gas has temperature ~ 8000 K (orange diagonal lines in Figure 7). The ionized gas has a range of ionization parameter $U_{\text{ion}} = \mathcal{E}_{\text{LyC}} / (\hbar v_{\text{LyC}} n_{\text{H}})$, but most falls in the range

$10^{-2.5}\text{--}10^{-1.5}$ (see gray dashed diagonal lines in the bottom row of Figure 6).

3.2. Evolution of Other Models

While the overall evolution of other models is similar to that of the fiducial model, there are a few notable differences. Here we give an overview of other simulations and take two extreme cases, one with the strongest initial turbulence/highest $\alpha_{\text{vir},0}$ (A5B2S4) and the other with the strongest initial magnetic field/lowest $\mu_{\Phi,0}$ (A2B05S04), to compare and contrast with the fiducial model. Results from these two extreme models are shown in the middle and right columns of Figures 3, 4, 5. In addition, in Section B we compare a series of snapshots of projected column density from members of the α -series in Figure 17 (all with `seed` = 4), members of the

⁷ For reference, this is equivalent to the intensity 10 pc away from a point source of luminosity $10^6 L_{\odot}$.

β -series models in Figure 18 (all with `seed` = 4), and the fiducial model (A2B2) with initial different turbulence realizations (i.e., varying `seed` but the same initial kinetic and magnetic energy) in Figure 19.

Our key simulation results are summarized in Table 2. Quantitative comparisons of star formation history, SFE, ionized and neutral gas ejection, timescale for star formation/cloud destruction, and escape fraction of radiation from all models will be presented in Sections 3.3–3.7. Comparisons of virial parameter evolution and efficiency per freefall time, also connecting with observations, will be discussed in Sections 3.8 and 3.9, respectively.

The bottom two rows of Table 2 show results from the fiducial model run at higher ($N_{\text{cell}} = 512^3$) and lower ($N_{\text{cell}} = 128^3$) resolutions. For the lower-resolution test, all turbulence realizations are run, while only the `seed` = 4 is run for the more-expensive, higher-resolution case. These tests demonstrate numerical convergence of our results, within the range of variation that is expected from turbulence-induced stochasticity in the evolution.

3.2.1. Dependence on $\alpha_{\text{vir},0}$

Even at quite early times, the extent of the molecular cloud systematically changes with $\alpha_{\text{vir},0}$. The left panels of Figure 17 in Figure B show that the cloud with the lowest initial virial parameter (A1B2S4, with $\alpha_{\text{vir},0} = 1$) initially contracts in size as turbulent pressure support is insufficient to counteract gravity. In contrast, clouds that are initially unbound have a larger fraction of their material at velocity greater than the escape speed of the cloud, and expand rapidly over the first few Myr of evolution. This has the effect of both directly enhancing the mass loss of neutrals and reducing the gas surface density during the star-forming epoch, both of which contribute to a systematically lower net SFE at higher $\alpha_{\text{vir},0}$.

In part because the turbulent shear is more effective in dispersing overdense structures before they collapse in the higher- $\alpha_{\text{vir},0}$ models, the time of the first star formation $t_{*,0}$ is nearly 1 Myr (on average) earlier in the lowest- $\alpha_{\text{vir},0}$ models compared to the highest- $\alpha_{\text{vir},0}$ models. Comparing Figure 3(a) and (d), even though the lifetime SFE is lower in the $\alpha_{\text{vir},0} = 5$ model compared to the $\alpha_{\text{vir},0} = 2$ model, “active” star formation continues over a longer period in the $\alpha_{\text{vir},0} = 5$ model (up to $t \sim 11$ Myr, compared to $t \sim 9$ Myr) because the cloud is not as rapidly dispersed by the feedback from vigorous star formation. Still, there is late-time residual star formation in the $\alpha_{\text{vir},0} = 2$ model, and the overall beginning-to-end duration of star formation does not show strong dependence on $\alpha_{\text{vir},0}$ across models (see Section 3.6).

We also note, as can be seen from the comparisons in Figure 4 and Figure 17, that distribution of radiation sources is less compact in the high- $\alpha_{\text{vir},0}$ compared to the low- $\alpha_{\text{vir},0}$ models.

3.2.2. Dependence on $\mu_{\Phi,0}$

Our simulation suite includes both strongly magnetized clouds (with the $\mu_{\Phi,0} = 0.5$ case even subcritical) and weakly magnetized clouds. The latter (models $\mu_{\Phi,0} = 4$ and 8) have initial $B_{z,0} < 10\mu\text{G}$, and the magnetic field remain energetically subdominant – with super-Alfvénic turbulence – throughout their lifetimes. Their overall evolution and morphological characteristics are largely similar to the fiducial model. Compared to the non-magnetized run, the first star formation event is a bit delayed (~ 0.5 –1 Myr), and SFR and net SFE are slightly lower.

The magnetically subcritical and critical clouds ($\mu_{\Phi,0} = 0.5$ and 1) have initial magnetic fields $54\mu\text{G}$ and $27\mu\text{G}$, with initially sub-Alfvénic turbulence. Figure 18 shows that overdense filamentary structures preferentially aligned perpendicular to the z -axis (to an extreme degree in the subcritical case). The strong magnetic field constrains motions to proceed primarily along the z -axis, and as a result the cloud expansion driven by feedback at late times is highly anisotropic in these models.

Compared to the fiducial model, in the subcritical and critical cases the strong magnetic field both delays the onset of star formation and reduces the SFR. As a result, it takes longer to build up enough stellar mass that the feedback is sufficient to disperse the residual gas. In addition, the reduced gas compressibility and strong magnetic tension force makes cloud structure less porous and H II regions remain confined for a longer period of time. This makes the escape of ionized gas and ionizing radiation more difficult. For these reasons, only a small fraction of gas is photoevaporated by LyC in the critical and subcritical cases. Compared to the fiducial model, in which most of the mass loss is in ionized gas, nearly 10 times as much gas is dispersed in the neutral phase as the ionized phase.

In fact, the evolution of magnetically subcritical clouds are unusual in several aspects. In A2B05S4, the first star formation occurs at 9.3 Myr and the net SFE is only 2.8%. The stellar mass builds up on a timescale that is long compared to the lifetime of ionizing luminosity (see Figure 3g, h). Due to the low luminosity, gas dispersal takes place steadily over a very long period (~ 20 Myr), the mass loss by photoevaporation is much less effective than in the fiducial model, and the LyC escape fraction does not reach a high value even at late times (Figure 3(g)). The evolution of σ_{1d} (Figure 5(j)) shows that the motion of neutral gas becomes highly anisotropic after the onset of feedback, with motions almost entirely parallel to the background magnetic field. The map of EM in Figure 4 shows that ionized gas outflows follow the magnetic field lines, and that the cloud dispersal is incomplete even at $t' = 8$ Myr (see also the right panels in Figure 3). The final frame of Figure 18 for the $\mu_{\Phi,0} = 0.5$ model shows an essentially columnar

outflow. Lack of evidence for these unusual morphological features in observations suggests that at GMC scales, real clouds are generally magnetically critical or supercritical.

3.2.3. Dependence on Turbulence Realization

For each model in the α - and β -series, we run five simulations with different random realizations for the initial turbulence. The initial large-scale velocity field and its orientation relative to the field line affect the specifics of when and where dense structures form, which in turn affect the subsequent cluster formation and cloud evolution. As a result, the simulation outcome exhibits a moderate degree of variation with random seeds. Figure 19 shows snapshots of the fiducial model with different turbulence realizations. We find that runs with `seed` = 1 and 5 form centrally-concentrated dense filaments, which are favorable to early, rapid burst of star formation (see second column in Figure 19). In contrast, overdense structures in runs with `seed` = 2 and 3 are spatially separated from each other, and these models have slower SFR and lower SFE. While some of the same trends with `seed` persist in other models with different $\alpha_{\text{vir},0}$ or $\mu_{\Phi,0}$, not all quantitative outcomes systematically vary with the random seed (see Sections 3.3–3.7).

For a given total kinetic energy, lower SFR and SFE in some turbulent realizations may simply be due to more of the large-scale modes (which contain most of the energy) favoring expansion or shear rather than compression.

3.3. Star Formation History and Rate

We compare star formation history of all models in Figure 8, which shows the stellar mass M_* as a function of $t' = t - t_{*,0}$ in the α -series (top) and β -series (bottom) models. Different initial turbulence realizations are labeled by `seed` = 1–5 (left to right).

The stellar mass growth occurs over several Myrs in a “stair-stepping” fashion due to our finite mass resolution (typical initial sink mass is about $10^{-3} M_0$). It is roughly linear during the main phase of star formation and levels off once the radiative feedback takes over. Some models exhibit a few episodic star formation events that take place in swept-up gas at the periphery of H II regions at late times.

We quantify the time-averaged SFR, $\langle \dot{M}_* \rangle$, during the main period of star formation by performing a least square fit to a function $M_*(t) = \langle \dot{M}_* \rangle t$ for the time interval $(t_{*,0}, t_{*,90\%})$. The results are shown as dashed lines in Figure 8, suggesting that linear mass growth is a good approximation for most of our models. Except for the runs with `seed` = 1 in the α -series, the mean SFR monotonically increases with decreasing $\alpha_{\text{vir},0}$ and with increasing $\mu_{\Phi,0}$. That is, higher kinetic and magnetic energy reduce the SFR, for a given cloud mass and size.

3.4. Star Formation Efficiency

Figure 8 shows that clouds in our simulations convert only a small fraction of the initial gas mass into stars over their lifetimes. In Figure 9, we show the SFE at $t' = 3$ Myr ($\varepsilon_{*,3\text{Myr}}$) and the lifetime SFE (ε_*) in the α - (left) and β -series (right) models. For each model, we show runs with different turbulent seeds with different symbols and colors. For the β -series models, the results of non-magnetized runs are shown as horizontal dashed lines. The time $t' = 3$ Myr is chosen to provide an estimate of the SFE at the time of the first supernova. In Columns (4) and (5) of Table 2 we list result for medians (over `seed`) of ε_* and $\varepsilon_{*,3\text{Myr}}$, and give differences to the minimum/maximum values with superscripts/subscripts. For example, the fiducial model (A2B2) has net SFE of $\varepsilon_* = 5.8^{+2.1}_{-1.4}\%$ for the 5 different runs.

For fixed turbulent realization, Figure 8 shows that final stellar mass decreases with increasing $\alpha_{\text{vir},0}$ and decreasing $\mu_{\Phi,0}$. The median net SFE in the α -series ranges between 2.1% and 9.5%, increasing for lower kinetic energy (lower $\alpha_{\text{vir},0}$). The median net SFE in the β -series models ranges between 2.4% and 8.4%, increasing for lower magnetization (higher $\mu_{\Phi,0}$). In all models, different turbulence realizations can produce variations at a level of a few percent in the SFE. Although the absolute variations in SFE are small, this amounts to up to factor of 2–3 range in $\varepsilon_{*,3\text{Myr}}$ and ε_* for different turbulence realizations. Most of our simulated clouds have formed about $\sim 50^{+20}_{-20}\%$ of the final stellar mass at $t' = 3$ Myr. The exceptions are the very strongly-magnetized models A2B05 and A2B1, in which $\varepsilon_{*,3\text{Myr}}/\varepsilon_* \sim 0.25$ as they have significantly longer star formation duration (see Section 3.6).

The simulations of Kim et al. (2018) were purely hydrodynamic, including a model analogous to `seed` = 1 and $\mu_{\Phi,0} = \infty$, which resulted in $\varepsilon_* = 0.13$, somewhat higher than 0.096 of our model A2B1infS1. This difference is likely to be caused by the inclusion of more realistic thermochemical processes in our new simulations; the temperature of molecular gas in the PDR is raised significantly due to the FUV heating, which makes the collapse of dense structures more difficult at late times (e.g., Inoguchi et al. 2020). Considering the stochastic nature of the system, these differences can also induce other changes; as we have shown, different realizations of turbulence lead to variations in SFE of a few percent.

3.5. Photoevaporation and Ejection Efficiencies

Clouds in our simulations are efficiently dispersed by UV radiation feedback, which converts the cold molecular gas that would otherwise form stars into atomic/ionized gas and drives outflows out of the computational domain. We define the photoevaporation efficiency (ε_{ion}) as the fraction of the initial cloud mass turned into ionized gas, and the neutral ejection efficiency ($\varepsilon_{\text{ej,neu}}$) as the fraction ejected from the simulation box in the molecular and atomic phases. Both ε_{ion}

Table 2. Simulation results

Model	$t_{*,0}$	$\tilde{\alpha}_{\text{vir,tot}}(t_{*,0})$	ε_*	$\varepsilon_{*,3 \text{ Myr}}$	ε_{ion}	$\varepsilon_{\text{ej,neu}}$	t_{SF}	$t_{\text{dest,H}_2}$	$t_{\text{dep,0}}$	$\varepsilon_{\text{ff,0}}$	$\langle f_{\text{esc,LyC}} \rangle$	$\langle f_{\text{esc,FUV}} \rangle$
	[Myr]		[%]	[%]	[%]	[%]	[Myr]	[Myr]	[Myr]	[%]	[%]	[%]
(1)	(2)	(3)	(4)	(5)	(6)	(7)	(8)	(9)	(10)	(11)	(12)	(13)
α-series												
A1B2	$3.5^{+0.6}_{-0.4}$	$0.67^{+0.12}_{-0.05}$	$9.5^{+2.9}_{-1.8}$	$5.6^{+1.3}_{-0.6}$	$73.2^{+1.1}_{-2.9}$	$17.4^{+3.5}_{-2.2}$	$5.0^{+0.3}_{-0.2}$	$7.4^{+0.7}_{-0.8}$	58^{+6}_{-13}	$8.0^{+2.4}_{-0.8}$	$21.0^{+4.6}_{-7.6}$	$52.7^{+4.3}_{-10.5}$
A2B2	$3.8^{+0.5}_{-0.5}$	$0.81^{+0.09}_{-0.10}$	$5.8^{+2.1}_{-1.4}$	$2.6^{+2.4}_{-1.1}$	$71.7^{+2.2}_{-0.7}$	$21.9^{+2.8}_{-2.6}$	$5.4^{+0.3}_{-1.1}$	$7.6^{+0.2}_{-0.8}$	99^{+52}_{-39}	$4.7^{+3.0}_{-1.6}$	$26.7^{+3.0}_{-0.5}$	$62.4^{+1.0}_{-5.1}$
A3B2	$3.7^{+1.3}_{-0.4}$	$1.08^{+0.01}_{-0.21}$	$4.1^{+2.2}_{-1.5}$	$1.9^{+2.0}_{-0.7}$	$68.3^{+3.4}_{-7.7}$	$28.7^{+8.2}_{-6.3}$	$5.5^{+1.1}_{-1.1}$	$7.5^{+0.5}_{-0.1}$	149^{+78}_{-52}	$3.2^{+1.7}_{-1.1}$	$27.6^{+12.9}_{-3.4}$	$65.9^{+3.0}_{-4.8}$
A4B2	$4.1^{+1.1}_{-0.9}$	$1.34^{+0.09}_{-0.20}$	$3.6^{+0.6}_{-1.9}$	$1.7^{+0.4}_{-0.7}$	$63.1^{+4.5}_{-15.9}$	$33.2^{+17.9}_{-4.8}$	$6.3^{+0.2}_{-1.2}$	$7.4^{+0.5}_{-0.6}$	163^{+190}_{-11}	$2.9^{+0.2}_{-1.5}$	$34.2^{+8.3}_{-9.4}$	$67.8^{+4.6}_{-0.1}$
A5B2	$4.3^{+1.3}_{-0.9}$	$1.69^{+0.04}_{-0.28}$	$2.1^{+1.1}_{-1.2}$	$1.2^{+0.2}_{-0.6}$	$48.3^{+9.4}_{-19.5}$	$49.6^{+20.4}_{-10.4}$	$5.3^{+1.5}_{-0.9}$	$8.3^{+0.5}_{-1.3}$	255^{+313}_{-31}	$1.8^{+0.3}_{-1.0}$	$31.2^{+18.5}_{-17.1}$	$68.8^{+8.6}_{-3.2}$
β-series												
A2B05	$8.6^{+4.7}_{-2.1}$	$0.69^{+0.07}_{-0.20}$	$2.4^{+1.2}_{-0.5}$	$0.5^{+0.3}_{-0.1}$	$12.4^{+5.0}_{-7.5}$	$83.5^{+2.2}_{-4.7}$	$12.0^{+3.5}_{-3.1}$	$17.3^{+4.8}_{-1.4}$	464^{+401}_{-163}	$1.0^{+0.5}_{-0.5}$	$13.1^{+0.3}_{-4.8}$	$56.5^{+1.7}_{-6.8}$
A2B1	$4.4^{+2.4}_{-0.9}$	$0.82^{+0.03}_{-0.17}$	$4.3^{+1.8}_{-1.8}$	$1.5^{+0.5}_{-0.9}$	$35.3^{+17.7}_{-8.7}$	$54.2^{+5.5}_{-13.9}$	$6.9^{+1.3}_{-1.1}$	$9.4^{+0.7}_{-1.0}$	182^{+103}_{-59}	$2.6^{+2.8}_{-0.9}$	$21.1^{+2.8}_{-9.5}$	$58.3^{+2.5}_{-1.7}$
A2B2	$3.8^{+0.5}_{-0.5}$	$0.81^{+0.09}_{-0.10}$	$5.8^{+2.1}_{-1.4}$	$2.6^{+2.4}_{-1.1}$	$71.7^{+2.2}_{-0.7}$	$21.9^{+2.8}_{-2.6}$	$5.4^{+0.3}_{-1.1}$	$7.6^{+0.2}_{-0.8}$	99^{+52}_{-39}	$4.7^{+3.0}_{-1.6}$	$26.7^{+3.0}_{-0.5}$	$62.4^{+1.0}_{-5.1}$
A2B4	$3.1^{+0.1}_{-0.4}$	$0.86^{+0.04}_{-0.16}$	$6.9^{+1.6}_{-1.9}$	$3.4^{+1.0}_{-0.6}$	$79.0^{+4.8}_{-1.9}$	$13.9^{+2.8}_{-6.1}$	$4.9^{+2.2}_{-0.7}$	$6.9^{+2.1}_{-0.4}$	84^{+20}_{-22}	$5.5^{+2.0}_{-1.1}$	$25.8^{+10.9}_{-2.5}$	$61.3^{+3.5}_{-5.3}$
A2B8	$2.6^{+0.2}_{-0.1}$	$0.90^{+0.12}_{-0.15}$	$7.4^{+2.3}_{-0.1}$	$3.7^{+0.7}_{-0.1}$	$82.3^{+2.4}_{-1.4}$	$9.2^{+1.5}_{-1.2}$	$5.4^{+1.0}_{-1.1}$	$7.4^{+0.7}_{-0.4}$	75^{+16}_{-13}	$6.3^{+1.3}_{-1.1}$	$33.0^{+4.5}_{-9.3}$	$64.2^{+2.6}_{-7.8}$
A2Binf	$2.1^{+0.2}_{-0.5}$	$1.00^{+0.27}_{-0.07}$	$8.2^{+3.3}_{-1.1}$	$5.1^{+1.7}_{-1.1}$	$82.6^{+2.7}_{-0.6}$	$8.1^{+1.7}_{-1.6}$	$4.1^{+0.8}_{-0.2}$	$6.4^{+0.4}_{-0.5}$	61^{+8}_{-14}	$7.7^{+2.2}_{-0.9}$	$30.7^{+5.5}_{-2.5}$	$63.3^{+3.4}_{-1.9}$
A2B2_N128	$4.2^{+0.4}_{-1.2}$	$0.81^{+0.12}_{-0.06}$	$6.1^{+3.4}_{-0.8}$	$3.1^{+2.7}_{-1.4}$	$68.1^{+5.7}_{-2.2}$	$25.9^{+1.2}_{-9.1}$	$6.3^{+0.4}_{-2.6}$	$7.6^{+0.3}_{-0.7}$	109^{+21}_{-57}	$4.3^{+4.7}_{-0.7}$	$32.7^{+0.5}_{-9.3}$	$63.1^{+1.2}_{-6.3}$
A2B2S4_N512	3.3	0.86	5.0	1.9	71.6	23.9	5.1	7.9	126	3.7	28.7	62.1

NOTE—For each model in the α - and β -series there are 5 realizations of turbulence. The reported values are medians, and the superscript (subscript) refers to the difference to the maximum (minimum) value. Results from tests at lower and higher (only `seed=4`) resolution are given in bottom two rows. Columns are as follows (1): model name indicating the initial virial parameter (A) and the magnetic flux-to-mass ratio (B). (2): time of first star formation. (3): virial parameter $\tilde{\alpha}_{\text{vir,tot}} = (2\mathcal{T} + \mathcal{B})/|\mathcal{W}|$ at $t_{*,0}$. (4): final SFE $\varepsilon_* = M_*/M_0$. (5): SFE at $t' = 3$ Myr. (6): photoevaporation efficiency. (7): ejected neutral efficiency. (8): star formation duration needed to assemble 90% of the final stellar mass. (9): cloud destruction time needed to reach $M_{\text{H}_2} = 0.05M_0$. (10): gas depletion time $t_{\text{dep,0}} = M_0/\langle \dot{M}_* \rangle$. (11): SFE per freefall time $\varepsilon_{\text{ff,0}} = t_{\text{ff,0}}/t_{\text{dep,0}}$ (12)–(13): cumulative (or luminosity-weighted mean) escape fractions of ionizing (LyC) and non-ionizing (FUV) radiation.

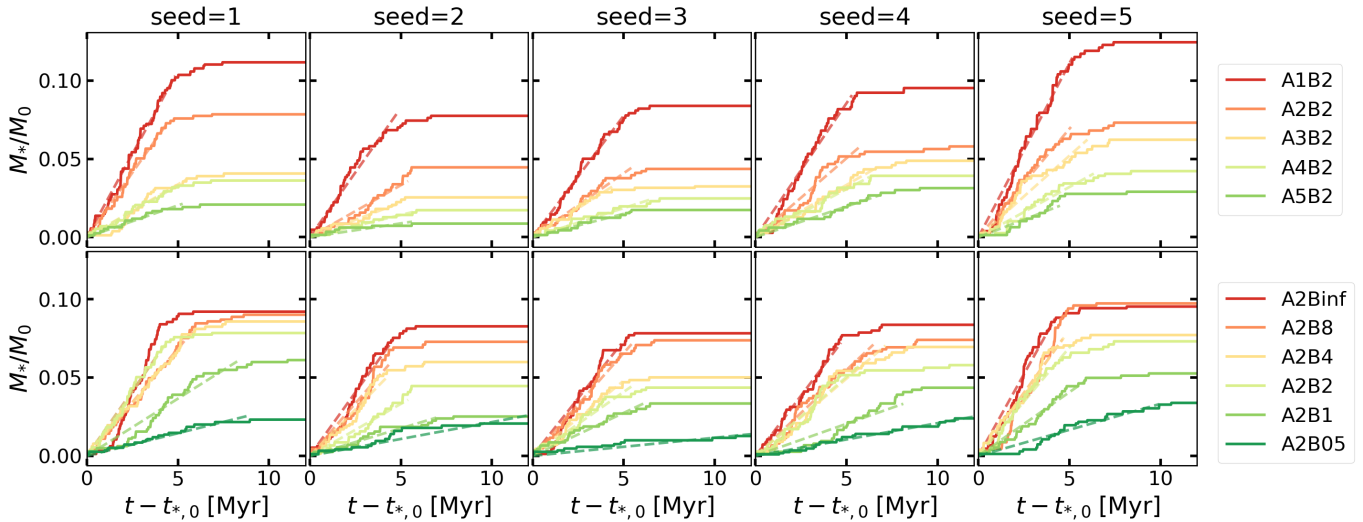


Figure 8. Star formation history of all models with different seeds. The upper/lower panels show α/β -series models. Time is measured from the moment of first star formation $t_{*,0}$. The dashed lines represent a linear least square fit for the time range $t_{*,0} < t < t_{*,90\%}$, where $t_{*,90\%}$ is the time at which 90% of the final stellar mass has been assembled. We use the slope of the line as the time averaged SFR $\langle \dot{M}_* \rangle$.

and $\varepsilon_{\text{ej,neu}}$ are measured at the end of the simulation (see also Kim et al. 2018).

Figure 10 shows ε_{ion} (top) and $\varepsilon_{\text{ej,neu}}$ (bottom) of the α - (left) and β - (right) series models. The me-

dian/minimum/maximum values are listed in Table 2. Except for strongly magnetized ($\mu_{\Phi,0} \leq 1$) clouds, the mass loss is dominated by photoevaporation, consistent with the results of hydrodynamic simulations by Kim

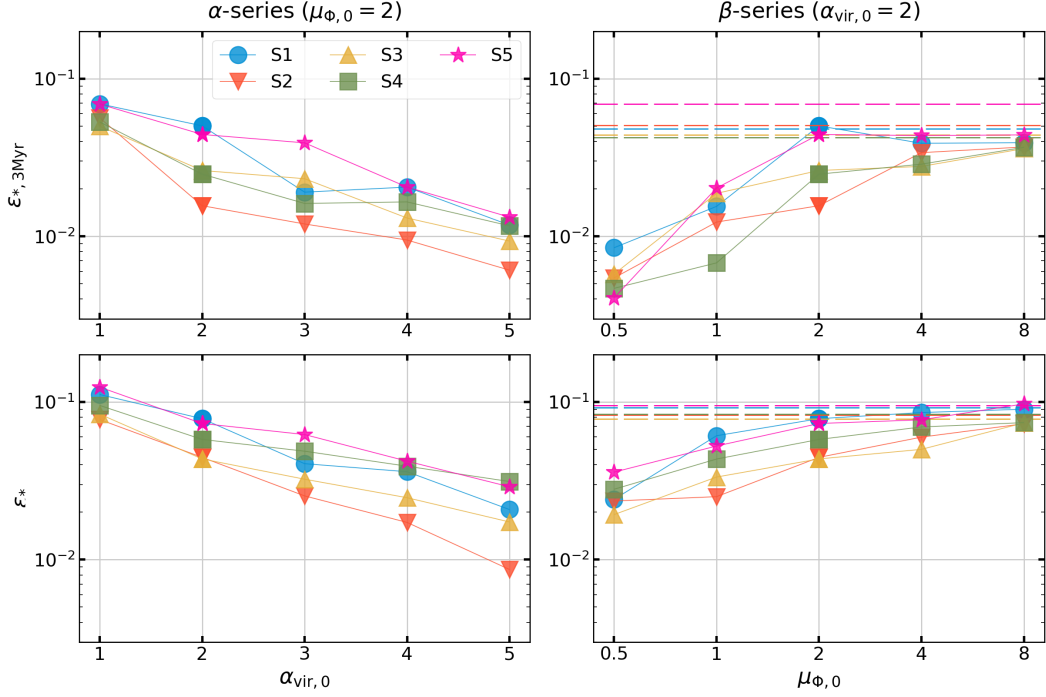


Figure 9. Star formation efficiency at time 3 Myr after the first star formation ($\varepsilon_{*,3 \text{ Myr}}$; top) and final star formation efficiency (ε_* ; bottom), in models with varying initial kinetic or magnetic energy or turbulence realization. The α -series is shown to the left and β -series to the right, with simulation runs having different turbulent realizations as marked by `seed` with different colors/symbols. Horizontal dashed lines in the right panels indicate the values for the unmagnetized models (A2Binf). Higher initial turbulence level (larger $\alpha_{\text{vir},0}$) or magnetization (smaller $\mu_{\Phi,0}$) reduces the star formation efficiency.

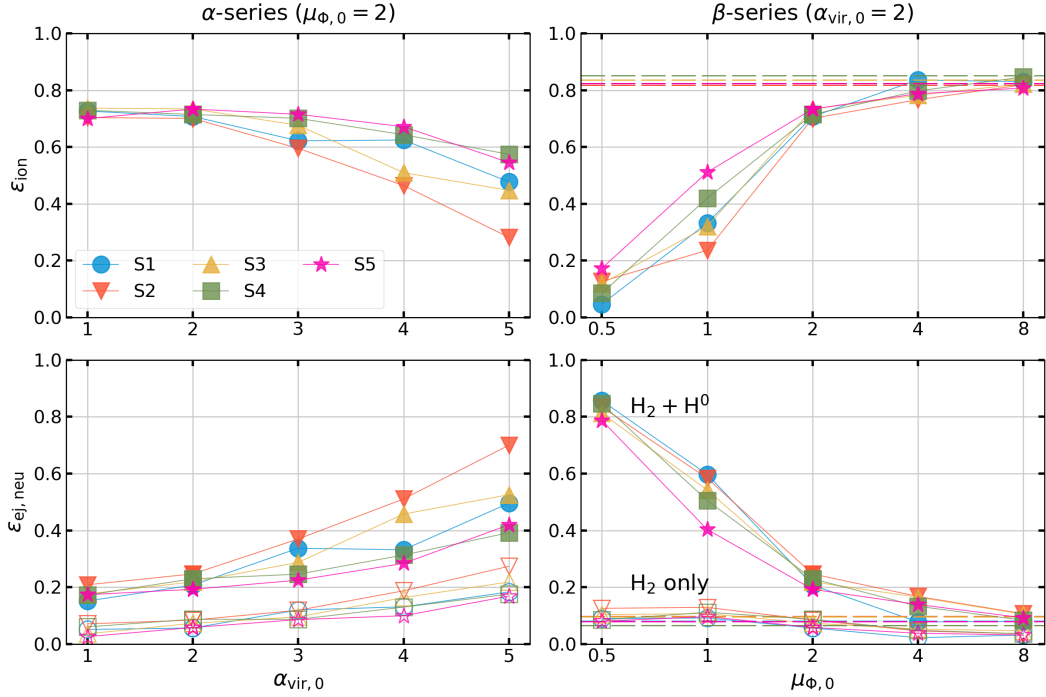


Figure 10. (Top) Fraction of initial cloud mass converted into ionized gas (photoevaporation efficiency; ε_{ion}) and (bottom) ejected from the computational domain as neutrals (ejected neutral efficiency; $\varepsilon_{\text{ej,neu}}$). The open symbols show the ejection efficiency of molecular gas. The left/right column shows results from the α/β -series simulations, with different turbulent `seed` and unmagnetized models indicated as in Figure 9.

et al. (2018). In the α -series models, as $\alpha_{\text{vir},0}$ increases

from 1 to 5, the median value of ε_{ion} decreases from 73%

to 48% while $\varepsilon_{\text{ej,neu}}$ increases from 17% to 50%. This result can be understood as initially unbound clouds ejecting a larger amount of neutral gas by initial turbulence and having lower ionizing photon rate. In the β -series models, the median value of ε_{ion} is higher than 70% for clouds with lower magnetization ($\mu_{\Phi,0} \geq 2$). In the magnetically subcritical (critical) case, however, only 13% (35%) of gas is photoevaporated by LyC photons and most of outflow mass is in the atomic phase. Although magnetically subcritical clouds have extended lifetime, the evaporation efficiency is low because of the low ionizing photon rate and magnetically confined H II region geometry. We also remark that outflows in magnetically subcritical clouds are unrealistically anisotropic; more than $\sim 80\%$ of the mass loss occurs along the direction of the background magnetic field (through the vertical (z) boundaries of the computational domain).

3.6. Timescales

Our simulations allow us to characterize several evolutionary timescales of GMCs dispersed by radiative feedback: the time of first star formation, timescales for star formation and cloud destruction, and the gas depletion time. Similar to the definition used by [Kim et al. \(2018\)](#), we define the duration of star formation as $t_{\text{SF}} = t_{*,90\%} - t_{*,0}$. The cloud destruction time is defined as the time for the molecular gas mass⁸ to be reduced to 5% of the initial cloud mass ($0.05M_0$), $t_{\text{dest,H}_2} = t_{\text{H}_2,5\%} - t_{*,0}$. The gas depletion time is calculated using the initial cloud mass and the time-averaged SFR as $t_{\text{dep,0}} = M_0 / \langle \dot{M}_* \rangle$. This should be distinguished from the observed gas depletion time, based on instantaneous gas mass and SFR. We note that the “instantaneous” depletion time $M_{\text{gas}}(t) / \dot{M}_*(t)$ will be close to $t_{\text{dep,0}}$ if the SFR is relatively constant and only a small fraction of the mass has been dispersed by feedback; from Figure 3 and Figure 8, these conditions are generally satisfied for our simulations in the middle of the active star-forming phase. An inherent issue in observations, however, is how the SFR is measured; we return to this in Section 3.9.2.

Figure 11 shows, from top to bottom, $t_{*,0}$, t_{SF} , $t_{\text{dest,H}_2}$, $t_{\text{dep,0}}$ of the α - (left) and β -series (right) models. Results for all turbulence realizations (labeled by **seed**) are shown separately; median, minimum, and maximum values for each model are summarized in Table 2. In the α -series models, the median value of $t_{*,0}$ ranges from 3.5 Myr to 4.3 Myr, equivalent to $0.8 - 0.9t_{\text{ff,0}}$, increasing only weakly with $\alpha_{\text{vir,0}}$. The duration of star formation is also roughly constant (slightly increasing with $\alpha_{\text{vir,0}}$) at $\sim 5 - 6$ Myr, which is $\sim 1.1 - 1.3t_{\text{ff,0}}$. Cloud destruction

⁸ We find that the destruction timescale based on the total neutral gas ($M_{\text{H}_0} + M_{\text{H}_2}$) gas mass is about 10% longer than the destruction timescale based on M_{H_2} , except for the model A2B05 for which $t_{\text{dest,neu}}$ is about 30% longer than $t_{\text{dest,H}_2}$.

occurs within $\sim 1.6 - 1.8t_{\text{ff,0}}$, a few Myrs after $t_{*,90\%}$, consistent with the results of hydrodynamic simulations in [Kim et al. \(2018\)](#).

In the β -series models, $t_{*,0}$ systematically increases with decreasing $\mu_{\Phi,0}$ while t_{SF} and $t_{\text{dest,H}_2}$, have mild variations with $\mu_{\Phi,0}$ for $\mu_{\Phi,0} \gtrsim 2$, but all timescales become significantly longer in the magnetically critical and especially subcritical cases. For example, the model A2B05S4 has $t_{*,0} = 9.3$ Myr, $t_{\text{SF}} = 12.0$ Myr, and $t_{\text{dest,H}_2} = 17.3$ Myr (see also Figure 3(g)).

The depletion time $t_{\text{dep,0}}$ systematically increases with increasing $\alpha_{\text{vir,0}}$, with median values ranging over 58–260 Myr. The median depletion time also increases from 62–460 Myr from unmagnetized to subcritically-magnetized models. The ratio $t_{\text{ff,0}} / t_{\text{dep,0}}$ is equivalent to the star formation efficiency per freefall time ε_{ff} . For our models, the median value increases from 2% to 8% as $\alpha_{\text{vir,0}}$ decreases, and from 1% to 8% as $\mu_{\Phi,0}$ increases. We further discuss how our results on efficiency per freefall time relate to theoretical models and observations in Section 3.9.

3.7. Escape Fraction of Radiation

Figure 12 shows the cumulative escape fractions of LyC and FUV radiation measured at the end of simulations (see also Table 2). Because neutral hydrogen acts as an additional source of opacity for ionizing radiation and most of LyC photons are emitted before the cloud destruction, the escape fraction of LyC radiation is smaller than that of FUV radiation.

In the α -series, median values of $f_{\text{esc,LyC}}^{\text{cum}}$ are in the range 21–34%, generally increasing with $\alpha_{\text{vir,0}}$, although there is a significant variation with random seeds at large $\alpha_{\text{vir,0}}$. In the β -series, $f_{\text{esc,LyC}}^{\text{cum}}$ increases with decreasing magnetic field strength, with medians in the range 13–33%. For point radiation sources, the escape fraction is determined by the solid-angle PDF of the optical depth as seen from the source and is higher if the width of the PDF is higher ([Safarzadeh & Scannapieco 2016](#); [Kim et al. 2019b](#)). Therefore, the trend in the β -series is a result of the reduced gas compressibility and the reduced width of the density PDF in strongly magnetized clouds.

In all of our models, $f_{\text{esc,LyC}}^{\text{cum}}$ measured at $t' = 3$ Myr is only $\sim 2 - 10\%$. In contrast, the hydrodynamic simulations of ([Kim et al. 2019b](#)) found that $f_{\text{esc,LyC}}^{\text{cum}} = 0.30$ at $t' = 3$ Myr for the same cloud with $M_0 = 10^5 M_\odot$, $R_0 = 20$ pc, seed = 1, $\mu_{\Phi,0} = \infty$. This discrepancy is likely due to different treatments of the ionizing photon production rate per stellar mass in the two simulations. In the present simulations, Ψ_{LyC} decreases with time and $\Psi_{\text{LyC}}(t_{\text{age}} = 3 \text{ Myr}) \approx 0.5\Psi_{\text{LyC}}(0)$; the cumulative value is heavily weighted by values at early times when $f_{\text{esc,LyC}} \ll 1$. In contrast, the conversion factor adopted by [Kim et al. \(2019b\)](#) was constant with time, but depended on the total cluster mass to account for the effects of poor sampling of the IMF at the high mass end. This effectively made the LyC photon pro-

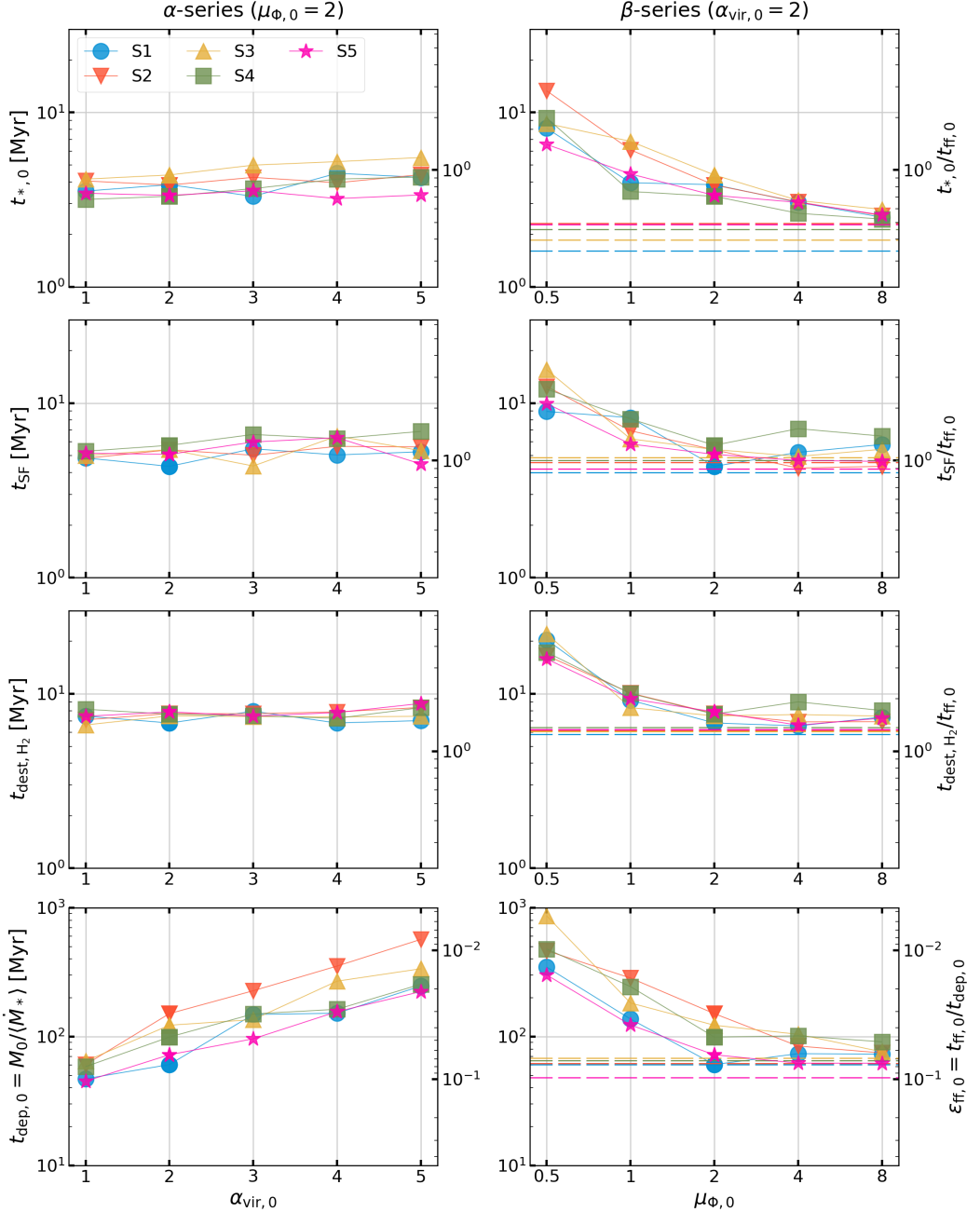


Figure 11. Evolutionary timescales with varying initial kinetic or magnetic energy or turbulence realization. (a) Time of first star formation event $t_{*,0}$, (b) duration of star formation $t_{\text{SF}} = t_{*,90\%} - t_{*,0}$, (c) timescale for cloud destruction $t_{\text{dest},\text{H}_2} = t_{\text{H}_2,5\%} - t_{*,0}$, and (d) gas depletion time $t_{\text{dep},0} = M_0/\langle \dot{M}_* \rangle$. Left axes give times in Myr. Right axes (top three rows) show times in units of the initial free-fall time $t_{\text{ff},0} = 4.68$ Myr, while the bottom row shows the inverse, equivalent to the star formation efficiency per freefall time. The left/right column shows the α/β -series simulations, with different turbulent **seed** and unmagnetized models indicated as in Figure 9.

duction rate per unit mass lower at the earliest times (when $M_{*,\text{total}} \lesssim 10^3$) compared to later time. Thus, the luminosity-weighted escape fraction was more heavily weighted to later times when photons escape more easily.

3.8. Virial Ratios

The Lagrangian virial theorem

$$\frac{1}{2} \ddot{I} = 2(\mathcal{T}_{\text{kin}} + \mathcal{T}_{\text{thm}} - \mathcal{T}_{\text{thm},0}) + \mathcal{B} - \mathcal{W} \quad (20)$$

describes the change (acceleration) of the gaseous system's moment of inertia ($I = \int \rho r^2 dV$) by kinetic (\mathcal{T}_{kin}), thermal (\mathcal{T}_{thm}), magnetic (\mathcal{B}), and gravitational (\mathcal{W}) en-

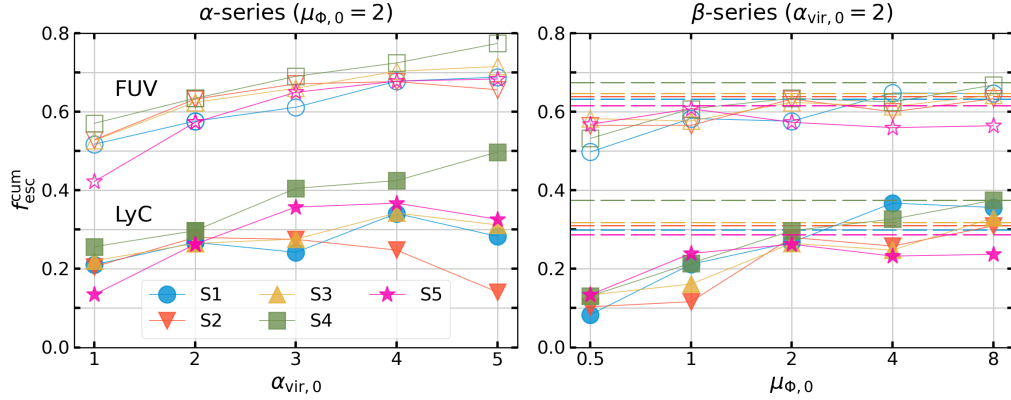


Figure 12. Cumulative escape fractions of LyC and FUV radiation for our α -series (left) and β -series models (right). Different turbulent seed and unmagnetized models are indicated as in Figure 9.

ergies associated with it. The term $\mathcal{T}_{\text{thm},0} = \frac{1}{2} \int_{\partial V_{\text{cl}}} \mathbf{P} \mathbf{r} \cdot d\mathbf{S}$ represents the confinement by thermal pressure of an external medium, where ∂V_{cl} is the bounding surface (an analogous term involving surface Reynolds stresses appears in the Eulerian virial theorem). It has been widely invoked to study global structure and stability (e.g., Zweibel 1990; Bertoldi & McKee 1992; McKee & Zweibel 1992; Ballesteros-Paredes et al. 1999) and to obtain mass estimates for molecular clouds (e.g., Solomon et al. 1987; Bolatto et al. 2008).

While it is observationally very difficult, if not impossible, to determine the individual terms in Equation (20) with precision (e.g., Singh et al. 2019), observers have traditionally employed the simple kinetic virial parameter $\alpha_{\text{vir}} = 5\sigma_{1\text{d}}^2 R/(GM)$ based on estimates of size, velocity dispersion, and mass to assess whether a cloud is gravitationally bounded ($\alpha_{\text{vir}} < 2$) or in virial equilibrium ($\alpha_{\text{vir}} \approx 1$). Strictly speaking, these diagnostics using α_{vir} apply to a steady-state ($\ddot{I} = 0$), homogeneous, spherical, non-magnetized cloud with no external forces acting on it. In particular, simple approaches treat clouds as isolated, while in reality GMCs are often in close proximity to each other, which reduces the magnitude of the gravitational energy because the effective zero of the gravitational potential lies near clouds rather than at infinite distance. By analyzing the dynamical state of structures found in kpc-scale simulations of the multiphase, star-forming ISM with self-consistent star formation and supernova feedback, Mao et al. (2020) found that α_{vir} is often inadequate as a measure of the gravitational boundedness of a structure, because tidal gravity, magnetic terms, and other effects can be large.

While in the present simulations there are no tidal forces, our model clouds have very high resolution and realistic physics. It is therefore interesting to test how well the simple estimate α_{vir} represents the true boundedness of our simulated clouds. To do this, we directly measure the virial parameter accounting for kinetic, thermal, and magnetic energies and compare with

α_{vir} computed via the traditional estimate. We calculate the energies of the neutral gas in the cloud as

$$\mathcal{T}_{\text{kin}} = \frac{1}{2} \int \rho v^2 \Theta dV, \quad (21)$$

$$\mathcal{T}_{\text{thm}} = \frac{3}{2} \int P \Theta dV, \quad (22)$$

$$\mathcal{B} = \frac{1}{8\pi} \int (B^2 - B_{\text{mean}}^2) \Theta dV, \quad (23)$$

$$\mathcal{W} = - \int \rho \mathbf{r} \cdot \nabla \Phi \Theta dV. \quad (24)$$

(e.g., McKee & Zweibel 1992). In Equation (23), the mean magnetic field strength $B_{\text{mean}} = |\int \mathbf{B} dS / \int dS|$ is measured at the spherical surface $r = 1.95R_0$.⁹ The gravitational potential Φ in Equation (24) includes contributions from not only the neutral cloud gas but also ionized gas and stars in the computational domain. This would make \mathcal{W} larger in magnitude than the self-gravitational energy of the neutral cloud at late times. Because Φ includes “external” terms, we cannot re-express \mathcal{W} as $-(1/2) \int \rho \Phi dV$; the latter expression would only apply if we were considering the whole system. We note that we shall henceforth ignore the term $\mathcal{T}_{\text{thm},0}$; given our relatively small box and outflowing gas, it is comparable to \mathcal{T}_{thm} , but realistically would be smaller.

With the above definitions, the more exact equivalent of the traditional kinetic virial parameter defined (for the initial cloud) in Equation (15) is

$$\tilde{\alpha}_{\text{vir}} \equiv \frac{2\mathcal{T}_{\text{kin}}}{|\mathcal{W}|}; \quad (25)$$

⁹ Ideally, the surface needs to be far enough from the cloud that B_{mean} represents the asymptotic value in the ambient medium (McKee & Zweibel 1992), but the finite size of the computational domain prevents us from doing that.

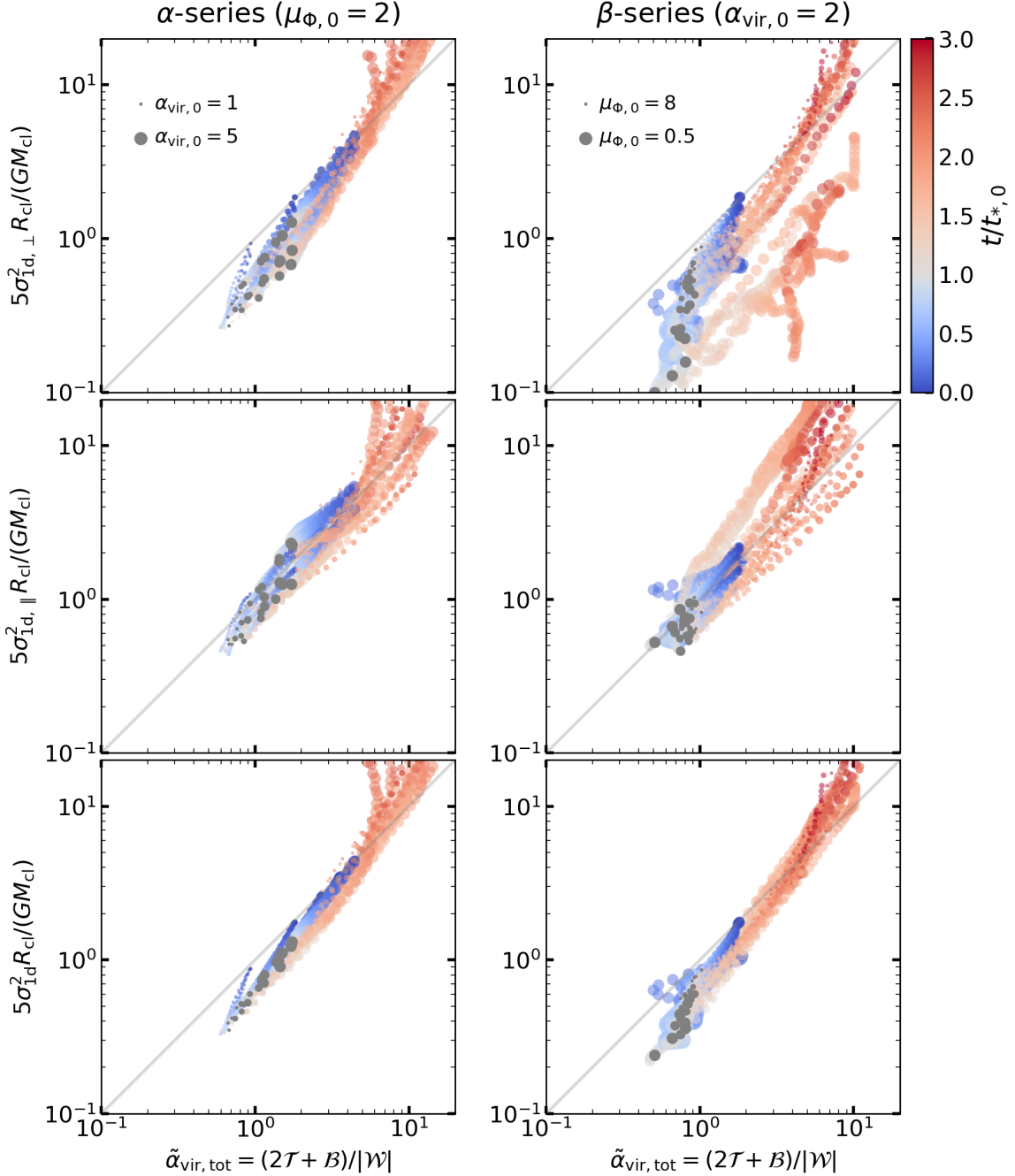


Figure 13. Comparison of the virial ratio $\tilde{\alpha}_{\text{vir,tot}} = (2\mathcal{T} + \mathcal{B})/|\mathcal{W}|$ and the traditional kinetic virial parameter defined as $\alpha_{\text{vir}} = 5\sigma_{1d}^2 R/(5M_{\text{neu}})$ in the α -series (left) and β -series (right) models. Each circle represents one snapshot and the color indicates the time of the snapshot normalized by the time of the first star formation. The grey circles mark values at $t = t_{*,0}$. The size of circles increases with increasing $\alpha_{\text{vir},0}$ and $B_{z,0}$ (decreasing $\mu_{\Phi,0}$). Rows show the traditional α_{vir} calculated with velocity dispersion perpendicular (top) and parallel (middle) to the z -axis, and averaged along all three Cartesian axes (bottom).

we use the tilde to emphasize the distinction.

The third row in Figure 5 plots the evolution of kinetic, thermal, magnetic, and gravitational energies of the cloud in models A2B2S4, A5B2S4, and A2B05S4. In the fiducial model, the magnitude of the gravitational energy remains very close to the initial value

$3GM_0^2/(5R_0)$ at early times. At late times ($t \gtrsim 5$ Myr), it begins to decrease as gas is photoevaporated and dispersed. A naive estimate $3GM_{\text{neu}}^2/(5R)$ for the late-time gravitational energy using the half-mass radius ($R = 2^{1/3}R_{50\%}$) is also shown using a blue dashed curve; the true gravitational energy is larger than this. This

is because the simple estimate ignores the gravitational binding energy from ionized gas and stars, and, more importantly, and substructure in the mass distribution, which is characterized by a few widely-separated clusters of gas clumps (which themselves contain closely packed dense cores), leading to the overestimation of the effective size of the system.

The evolution of the kinetic energy follows that of the velocity dispersion (second row in Figure 5), although the increase after $t \sim 5$ Myr is less significant due to mass loss. The magnetic energy saturates at a level that is about four times lower than the initial gravitational energy, until it decreases due to gas dispersal at late times. The thermal energy is unimportant at early times, but later becomes comparable to \mathcal{B} and $|\mathcal{W}|$ due to the FUV heating.

The other two models show a similar evolutionary trend, but it is worth noting that $|\mathcal{W}|$ in A5B2S4 decreases starting from $t = 0$ due to the initial expansion of the unbound cloud, and that the magnetic energy in A2B05S4 is comparable to the kinetic energy before $t \sim 12$ Myr when dispersal by feedback begins.

In the fourth row of Figure 5, we show the “observed” virial parameter α_{vir} computed from the instantaneous M_{neu} and $R = 2^{1/3}R_{50\%}$, and three different measures of the velocity dispersion: $\sigma_{1d,\perp}$, $\sigma_{1d,\parallel}$, and σ_{1d} . We compare to the ratio $\tilde{\alpha}_{\text{vir}} = 2\mathcal{T}_{\text{kin}}/|\mathcal{W}|$ (cyan). The kinetic virial parameter $\alpha_{\text{vir}} = 5\sigma_{1d}^2 R/(GM_{\text{neu}})$ (gray) agrees very well with $\tilde{\alpha}_{\text{vir}} = 2\mathcal{T}_{\text{kin}}/|\mathcal{W}|$ at early times, but becomes larger than $\tilde{\alpha}_{\text{vir}}$ when cloud disruption is underway, as the true gravitational binding energy is larger than the simple estimate $3GM_{\text{neu}}^2/(5R)$.

Because clouds are supported jointly by thermal energy, turbulence, and magnetic fields, it is natural to consider virial parameters including additional terms. We define $\mathcal{T} = \mathcal{T}_{\text{kin}} + \mathcal{T}_{\text{thm}}$, such that the virial parameter including both nonthermal and thermal gas motions is $2\mathcal{T}/|\mathcal{W}|$. The virial parameter accounting for the total energy is

$$\tilde{\alpha}_{\text{vir,tot}} = \frac{2\mathcal{T} + \mathcal{B}}{|\mathcal{W}|}. \quad (26)$$

The time evolution of $2\mathcal{T}/|\mathcal{W}|$ (purple) and $(2\mathcal{T} + \mathcal{B})/|\mathcal{W}|$ (black) are plotted in the bottom row of Figure 5. The thermal terms do not make a large difference, but the magnetic terms can lead to a factor of two increase in $\tilde{\alpha}_{\text{vir,tot}}$ compared to $\tilde{\alpha}_{\text{vir}}$, or even more for the most strongly magnetized model.

The scatter plots in Figure 13 show the relationship between the traditional kinetic virial parameter estimate (α_{vir}) and total virial ratio ($\tilde{\alpha}_{\text{vir,tot}}$) for all of the simulation snapshots taken before $t_{*,90\%}$ in the α - (left) and β -series (right) models. From top to bottom, the ordinate shows the kinetic virial parameter computed using $\sigma_{1d,\perp}$, $\sigma_{1d,\parallel}$, and σ_{1d} . The symbols are colored by time normalized to $t_{*,0}$. Grey dots mark the values at $t = t_{*,0}$.

In all models, $\tilde{\alpha}_{\text{vir,tot}}$ initially decreases with time due to the decay of turbulence, and then turns around after the onset of radiative feedback. Remarkably, $\tilde{\alpha}_{\text{vir,tot}}$ at $t = t_{*,0}$ in the α -series (β -series) falls in a fairly narrow range $\sim 0.6\text{--}1.7$ ($\sim 0.5\text{--}1$), suggesting that the collapse starts when the cloud reaches a near-virial state.

The results of the α -series models suggest that, for moderate magnetic field strength ($\mu_{\Phi,0} = 2$), α_{vir} can underestimate or overestimate the true gravitational boundedness depending on the relative orientation between the mean magnetic field and the observer’s line of sight. The bottom panels of Figure 13 suggest that, even with the correct estimate of kinetic energy, the kinetic virial parameter would systematically overrate the boundedness due to the neglect of magnetic support. The results of the β -series models (the bottom right panel in Figure 5 and the top right panel in Figure 13) suggest that the use of the traditional kinetic virial parameter can significantly underestimate the kinetic energy in magnetically critical and subcritical clouds when the line of sight is orthogonal to the field direction. Still, except for extreme magnetizations and orientations, the traditional α_{vir} estimates boundedness within a factor of ~ 2 .

We emphasize that the above results are for isolated clouds; tidal forces will reduce the gravitational energy, which would increase $\tilde{\alpha}_{\text{vir,tot}}$. This would enhance the discrepancy between the traditional virial estimate and the true boundedness shown in the bottom panels of Figure 13.

3.9. SFE per Freefall Time

The freefall time $t_{\text{ff}} = \sqrt{3\pi/(32G\rho)}$ is a natural characteristic timescale in a self-gravitating gaseous system, representing the shortest possible timescale for gravitational collapse at a given mean density. In common practice, the SFR is expressed as

$$\dot{M}_* \equiv \varepsilon_{\text{ff}} \frac{M_{\text{gas}}}{t_{\text{ff}}}, \quad (27)$$

which defines the SFE per freefall time ε_{ff} ; the freefall time is evaluated at the mean density of the system (e.g., Krumholz & McKee 2005). Since the star formation rate is also defined in terms of the depletion time, $\dot{M}_* \equiv M_{\text{gas}}/t_{\text{dep}}$, these are related by $\varepsilon_{\text{ff}} = t_{\text{ff}}/t_{\text{dep}}$. A cloud collapsing under its own gravity without any hindrance would form stars at maximal efficiency ($\varepsilon_{\text{ff}} \approx 1$, $t_{\text{dep}} \approx t_{\text{ff}}$). A wealth of observational studies however suggest that both galactic and cloud-scale star formation proceeds much slower than the freefall rate ($\varepsilon_{\text{ff}} \ll 1$ or $t_{\text{dep}} \gg t_{\text{ff}}$) (e.g., Zuckerman & Evans 1974; Williams & McKee 1997; Krumholz & Tan 2007; Kennicutt & Evans 2012; Evans et al. 2014; Lee et al. 2016; Barnes et al. 2017; Leroy et al. 2017; Ochsendorf et al. 2017; Utomo et al. 2018).

In our simulations, we measure the SFE per freefall time using the mass and freefall time of the cloud at

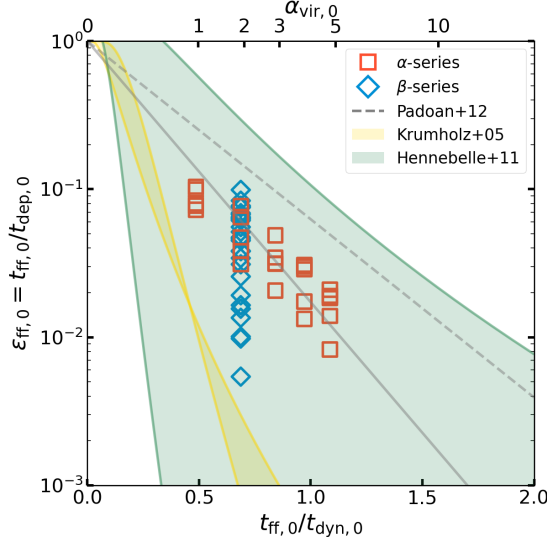


Figure 14. Time-averaged SFE per free fall time defined as $\langle \varepsilon_{\text{ff}} \rangle \varepsilon_{\text{ff},0} = t_{\text{ff},0} \langle \dot{M}_* \rangle / M_0 = t_{\text{ff},0} / t_{\text{dep},0}$ as a function of the ratio between the initial freefall and dynamical times in the α -series (red squares) and the β -series (blue diamonds) models. The empirical law $\exp(-1.6\sqrt{3}t_{\text{ff},0}/t_{\text{dyn},0})$ found by Padoan et al. (2012) is shown as a gray dashed line. The gray solid shows the fit to the α -series simulations $\exp(-4.06t_{\text{ff},0}/t_{\text{dyn},0})$. The yellow (green) shaded region is the prediction by the analytic model of Krumholz & McKee (2005) (Hennebelle & Chabrier (2011)) for the Mach number range $13.6 < \mathcal{M} < 30.4$ with $b = 0.5$ and $\beta = 0.02$ (see text for more details).

$t = 0$ and the time-averaged SFR $\langle \dot{M}_* \rangle$ as

$$\varepsilon_{\text{ff},0} = t_{\text{ff},0} \frac{\langle \dot{M}_* \rangle}{M_0} = \frac{t_{\text{ff},0}}{t_{\text{dep},0}}. \quad (28)$$

This is similar to the approach adopted by Padoan et al. (2012); Raskutti et al. (2016). Since $t_{\text{ff},0}$ is the same for all of the present models, $t_{\text{dep},0}$ and $\varepsilon_{\text{ff},0}$ are inversely proportional to each other.

The right y -axes in the bottom row of Figure 11 indicates that $\varepsilon_{\text{ff},0}$ ranges between 0.008 and 0.1 in the α -series and between 0.006 and 0.1 in the β -series, with scatter of 0.3–0.5 dex for each model. Note that the ratio between ε_* and $\varepsilon_{\text{ff},0}$ corresponds to the duration of star formation in units of $t_{\text{ff},0}$ (second row in Figure 11), which is in the range $\sim 1\text{--}2$.

Our simulations show that $\varepsilon_{\text{ff},0}$ decreases when the virial parameter increases, which is qualitatively consistent with some previous work. In the rest of this section, we study more quantitatively the relationship between the SFE per freefall time and the virial parameter in comparison to other simulations, theoretical models, and observations.

3.9.1. Comparison with Simulations and Theory

In Figure 14, we plot $\varepsilon_{\text{ff},0}$ of all models against the ratio $t_{\text{ff},0}/t_{\text{dyn},0} = \sqrt{\pi^2/40}\alpha_{\text{vir},0}^{1/2}$, where $t_{\text{dyn},0} \equiv R_0/\sigma_{1d,0}$ is the dynamical time (or turbulent crossing time) at $t = 0$. We perform a linear square fit of the α -series models to $\varepsilon_{\text{ff},0} = \exp(-Ct_{\text{ff},0}/t_{\text{dyn},0})$ and find the best-fit value $C = 4.06$, which is shown as a grey solid line.

The empirical relation $\varepsilon_{\text{ff},0} \propto \exp(-Ct_{\text{ff},0}/t_{\text{dyn},0})$ is qualitatively consistent with the star formation law proposed by Padoan et al. (2012), who carried out a set of adaptive-mesh refinement simulations of star formation with driven turbulence in a periodic box. For a range of 3D sonic Mach number (10 and 20), Alfvén Mach number (1.25–33), and the timescale ratio $0.23 < t_{\text{ff}}/t_{\text{dyn}} < 1.78$ (or $0.2 < \alpha_{\text{vir}} < 13$), they measured ε_{ff} from the slope of a linear fit between the $M_*(t)/M_0$ and $t/t_{\text{ff},0}$. They found that ε_{ff} has weak dependence on \mathcal{M} and \mathcal{M}_A and is well fit by a relation $\exp(-1.6\sqrt{3}t_{\text{ff}}/t_{\text{dyn}})$ ¹⁰, which is shown as a gray dashed line in Figure 14. While our best-fit value $C = 4.06$ is steeper than 2.77 found by Padoan et al., a direct comparison is difficult considering the ambiguity in defining the dynamical timescale and/or the gravitational energy in local simulations with periodic boundary conditions. The main point is that a similar exponential dependence of $\varepsilon_{\text{ff},0}$ on $\alpha_{\text{vir},0}^{1/2}$ holds true in global as well as local simulations, and for realistic feedback as well as driving in k -space.

To explain the low observed SFR, a class of theoretical models have been proposed to describe how (magnetized) turbulence regulates SFR (e.g., Krumholz & McKee 2005; Padoan & Nordlund 2011; Hennebelle & Chabrier 2011; see also the reviews by Federrath & Klessen 2012 and Padoan et al. 2014). In brief, these models assume that star formation takes place in a (magnetized) supersonically turbulent cloud where the distribution of mass with density follows a lognormal PDF: $p(s) = (\sqrt{2\pi}\sigma_s)^{-1} \exp[-(s - s_0)^2/(2\sigma_s^2)]$, where $s = \ln(\rho/\rho_0)$, $s_0 = \sigma_s^2/2$, ρ_0 is the mean density, and σ_s increases at higher Mach number \mathcal{M} , with some reduction for stronger magnetic fields.

The collapse is assumed to occur in regions where the support by thermal plus turbulent pressure cannot overcome gravity, and it is argued that this leads to a critical density $\rho > \rho_{\text{crit}}$, where various different forms have been proposed for ρ_{crit} as a function of α_{vir} , \mathcal{M} , and β (see Table 1 in Federrath & Klessen 2012). The fraction of mass undergoing collapse per free-fall time (hence SFE per free-fall time) can then be obtained by integrating the mass PDF above the critical density. A “multi-freefall” factor $t_{\text{ff}}(\rho)/t_{\text{ff}}(\rho_0)$ is included inside the

¹⁰ The best-fit value found by Padoan et al. (2012) is 1.6. The factor of $\sqrt{3}$ comes in because Padoan et al. (2012) defined the dynamical timescale as $t'_{\text{dyn}} = L/(2\sigma_{3D})$, where L is the box size; taking $L = 2R_0$ gives $t'_{\text{dyn}} = t_{\text{dyn}}/\sqrt{3}$.

integral in some models to account for the freefall time of gas structures at different densities.

We compare our results with the analytic models of SFR. Of the six models presented in Table 1 of [Federrath & Klessen \(2012\)](#), we consider the [Krumholz & McKee](#) model without the multi-freefall factor (KM), and the multi-freefall version of the [Hennebelle & Chabrier](#) model (multi-ff HC), both of which are extended to include the effect of magnetic field. The yellow and green shaded regions in Figure 14 show the predictions by the KM and multi-ff HC models, respectively. In both models, we have assumed fixed values of $b = 0.5$ and $\epsilon_{\text{core}}/\phi_t = 1$, and author-favored values of fudge factors $\phi_x = 1.12$ for the KM model and $y_{\text{cut}} = 0.1$ for the multi-ff HC model, respectively (see [Federrath & Klessen 2012](#)). We also take $\beta = 0.02$ and a range of sonic Mach number $13.6 < \mathcal{M} < 30.4$ consistent with the parameters of the α -series models.¹¹

The qualitative prediction by these analytic models agrees with our simulation results, although the quantitative results differ. Both models predict that ρ_{crit} increases linearly with α_{vir} (for fixed other dimensionless parameters), so ε_{ff} decreases with increasing α_{vir} . Higher overdensity is required for collapse at higher α_{vir} because the relative importance of turbulent stress, which tends to tear apart structures, versus gravity increases. In the [Krumholz & McKee](#) model, the dependence on Mach number is weak, because an increase in \mathcal{M} increases both the critical density ($\rho_{\text{crit}} \propto \mathcal{M}^2$) and the width of the density PDF, whose effects tend to cancel each other. In the [Hennebelle & Chabrier](#) model, however, $\rho_{\text{crit}} \propto \mathcal{M}^{-2}$ and ε_{ff} increases monotonically (and sensitively) with increasing \mathcal{M} .

3.9.2. Comparison with Observations

Next, we compute the time-dependent, “observed” SFE per freefall time $\varepsilon_{\text{ff,obs}}$ using mock observations of simulated clouds. For this exercise, we use the instantaneous cloud mass (M_{neu} , assumed to be recoverable from molecular lines or dust emission), size ($R = 2^{1/3}R_{50\%}$), and velocity dispersion (σ_{1d}) to compute the dynamical time $t_{\text{dyn}} = R/\sigma_{1d}$ and the free-fall time $t_{\text{ff}} = \sqrt{3\pi/(32G\bar{\rho})}$, where $\bar{\rho} = 3M_{\text{neu}}/(4\pi R^3)$. The instantaneous ratio $t_{\text{ff}}/t_{\text{dyn}} \propto \sigma_{1d}(R/M_{\text{neu}})^{1/2}$.

Assuming that an observer is able to recover cluster’s bolometric UV luminosity from massive star formation tracers such as H α and/or infrared fluxes, the instantaneous SFR is calculated as $\dot{M}_* = \Psi^{-1}L_{\text{UV}}/t_{\text{UV}}$, where $L_{\text{UV}} = L_{\text{LyC}} + L_{\text{FUV}}$ is the bolometric UV luminosity. For the conversion factor between SFR and UV luminosity, we use the IMF-averaged light-to-mass ratio $\Psi = 10^3 L_{\odot} M_{\odot}^{-1}$ (see also Figure 16), and we adopt an effective lifetime of UV luminosity

$t_{\text{UV}} = 6.7 \text{ Myr}$, to be consistent with the relation $M_* = 1.5 \times 10^{-4} M_{\odot} \text{ Myr}^{-1} (L_{\text{UV}}/L_{\odot})$ widely adopted in observations ([Kennicutt & Evans 2012](#); [Liu et al. 2020](#)). This assumes a more exact age for the stellar system is not known, although with spectral fitting cluster ages can be obtained (e.g. [Adamo et al. 2017](#)). The observed SFE per freefall time is then $\varepsilon_{\text{ff,obs}} = (t_{\text{ff}}/t_{\text{UV}})L_{\text{UV}}/(\Psi M_{\text{neu}}) \propto M_*(R/M_{\text{neu}})^{3/2}$.¹²

Figure 15 plots as squares (α -series) and diamonds (β -series) $\varepsilon_{\text{ff,obs}}$ for all models as a function of $t_{\text{ff}}/t_{\text{dyn}}$. The top axis also shows instantaneous $\alpha_{\text{vir}} = (40/\pi^2)(t_{\text{ff}}/t_{\text{dyn}})^2$. We consider snapshots in the time range $t_* < t < t_{*,90\%}$. The color of symbols indicates the 1D velocity dispersion. In contrast with $\varepsilon_{\text{ff,0}}$ in Figure 14, all of our models start from the lower left with $\alpha_{\text{vir}} \sim 0.5\text{--}1.5$ and $\varepsilon_{\text{ff,obs}} \sim 10^{-3}$, and, as time progresses, they move upward slightly and then to the upper right. This trajectory reflects the evolution of cloud’s gas mass, size, and velocity dispersion, and the cluster’s mass and luminosity. The stellar mass M_* and UV luminosity start very small and keep increasing during the main star formation phase (note that t_{SF} is comparable or shorter than t_{UV} , except for a small number of late snapshots in strongly magnetized clouds). Meanwhile, radiation feedback drives mass loss and radial expansion, leading to an increase in R/M_{neu} , together with an increase in velocity dispersion σ_{1d} . As a result, evolution causes $\varepsilon_{\text{ff,obs}} \propto M_*(R/M_{\text{neu}})^{3/2}$ and $t_{\text{ff}}/t_{\text{dyn}} \propto \sigma_{1d}(R/M_{\text{neu}})^{1/2}$ to increase in tandem. The distribution of $t_{\text{ff}}/t_{\text{dyn}}$ extends to larger values (by a factor of a few) than in Figure 14 due to cloud evolution. Even more extreme is the stretch in the distribution of $\varepsilon_{\text{ff,obs}}$ by two orders of magnitude compared to $\varepsilon_{\text{ff,0}}$ in Figure 14. We note, however, that in their later stages, the simulated systems have very low gas mass (leading to $\varepsilon_{\text{ff,obs}} \gtrsim 0.1$ and $t_{\text{ff}}/t_{\text{dyn}} \gtrsim 1$), and would not necessarily be included in observed star-forming GMC samples.

Although there is a large variation during the evolution, we calculate the “characteristic” values of $t_{\text{ff}}/t_{\text{dyn}}$ and $\varepsilon_{\text{ff,obs}}$ as a median for snapshots equally spaced in time between $t_{*,0}$ and $t_{*,90\%}$. We find $0.54 < \text{med}(t_{\text{ff}}/t_{\text{dyn}}) < 1.08$ and $0.8\% < \text{med}(\varepsilon_{\text{ff,obs}}) < 3.7\%$ in the α -series models, while $0.54 < \text{med}(t_{\text{ff}}/t_{\text{dyn}}) < 1.23$ and $0.8\% < \text{med}(\varepsilon_{\text{ff,obs}}) < 3.5\%$ in the β -series models. The bars in Figure 15(a) indicate the ranges of the medians. These values are similar to the ranges of $t_{\text{ff,0}}/t_{\text{dyn,0}}$ and $\varepsilon_{\text{ff,0}}$ shown in Figure 14, as indicated by grey bars in Figure 15(a).

The circles in each panel show estimates of the ratio $t_{\text{ff}}/t_{\text{dyn}}$ and ε_{ff} for observed star-forming clouds, colored by one-dimensional velocity dispersion. Panel (a) shows the low-mass, nearby cloud sample taken from [Evans et al. \(2014\)](#), in which the cloud mass and size

¹¹ We note that in the α -series models M_0 and $\alpha_{\text{vir},0}$ vary together rather than independently of each other (see Table 1).

¹² Strictly speaking, L_{UV}/Ψ can underestimate the stellar mass if $t_{\text{SF}} \gtrsim t_{\text{UV}}$, but $t_{\text{SF}} < t_{\text{UV}}$ for most of our clouds.

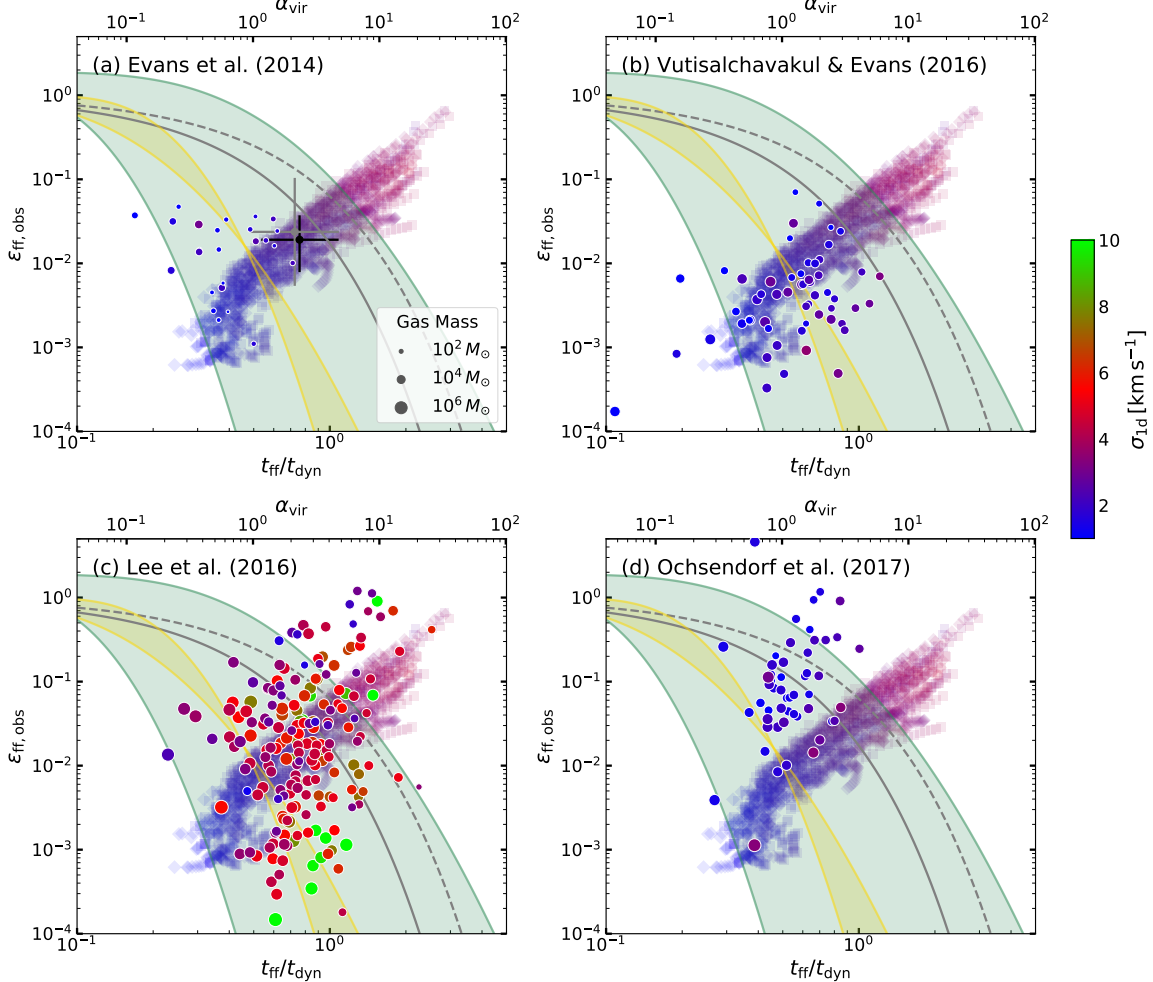


Figure 15. Relation between instantaneous $t_{\text{ff}}/t_{\text{dyn}} = (\pi^2/40)^{1/2} \alpha_{\text{vir}}^{1/2}$ vs. $\varepsilon_{\text{ff,obs}}$ in simulations (squares and diamonds; α - and β -series models) and observations (circles). For simulations, we use the instantaneous mass, size, and velocity dispersion of the gas cloud and cluster’s bolometric UV luminosity. We show snapshots in the time interval $t_{*,0} < t < t_{*,90\%}$. The circles in different panels show data from different observational studies: (a) low-mass, nearby clouds compiled by Evans et al. (2014); (b) molecular clouds in the Galactic Plane with massive star formation rate $M_* > 5 M_\odot \text{ Myr}^{-1}$ (Vutisalchavakul et al. 2016). (c) GMCs with associated star-forming complexes in the Milky Way (Lee et al. 2016). (d) GMCs with associated star-forming complexes in the Large Magellanic Cloud (Ochsendorf et al. 2017). All data points are colored by one-dimensional velocity dispersion σ_{1d} and their sizes denote gas mass. The solid and dashed gray lines, and the yellow and green shaded areas, are based on the same functional forms as in Figure 14, but for instantaneous measurements. In panel (a), the grey bars indicate the ranges of $\varepsilon_{\text{ff,0}}$ and $t_{\text{ff,0}}/t_{\text{dyn,0}}$ plotted in Figure 14, while the black bars indicate the ranges of median values of $\varepsilon_{\text{ff,obs}}$ and $t_{\text{ff}}/t_{\text{dyn}}$ for snapshots between $t_{*,0}$ and $t_{*,90\%}$.

are derived from extinction maps, velocity dispersion from molecular linewidth (mostly ^{13}CO), and SFRs from counting young stellar objects (YSOs). Panel (b) shows the sample of larger molecular clouds in the Galactic Plane with ongoing massive star formation, compiled by Vutisalchavakul et al. (2016) (their Fig. 6). In their study, the cloud properties are derived from ^{13}CO observations and SFR is determined from mid-infrared (MIR) luminosity. Following Vutisalchavakul et al. (2016), we exclude clouds with $\dot{M}_* < 5 M_\odot \text{ yr}^{-1}$ as MIR emission may seriously underestimate the true SFR at low SFR

(even for cases shown, the MIR-based SFR may be underestimated by a factor 2–3). Panel (c) shows the Milky Way GMCs with associated star-forming complexes in Lee et al. (2016) (their Fig. 7). Their samples are built from the ^{12}CO catalog of molecular clouds (Miville-Deschénes et al. 2017), cross-correlated with WMAP free-free sources. The panel (d) shows the star forming complexes in the Large Magellanic Cloud (Ochsendorf et al. 2017). The cloud properties are identified by ^{12}CO and SFR from $\text{H}\alpha + 24\mu\text{m}$. We note that they multiplied the $\text{H}\alpha$ -based SFR by a factor of 2 to account

for the fact that the diffuse H α emission (outside the star-forming regions) constitutes 50% of the total H α emission (Pellegrini et al. 2012).

The results for $\varepsilon_{\text{ff,obs}}$ from the simulations are generally similar to the observations, especially for the Vutisalchavakul et al. (2016) sample. However, the observations show no significant correlation of SFE per freefall time with $t_{\text{ff}}/t_{\text{dyn}}$. Furthermore, while the theoretical predictions (green and yellow shaded regions) lie in the same general range as both $\varepsilon_{\text{ff,obs}}$ from the simulations and the observations themselves, they do not follow the same trends. We conclude that evolutionary effects (the correlated increase over time of stellar mass, cloud size, and velocity dispersion along with the decrease of gas mass), which tend to make $\varepsilon_{\text{ff,obs}}$ increase with $t_{\text{ff}}/t_{\text{dyn}}$ in Figure 15, completely obscure the underlying decrease of $\varepsilon_{\text{ff,0}}$ with $t_{\text{ff,0}}/t_{\text{dyn,0}}$ seen in Figure 14.

Also, while the observed SFE per freefall time is small on average, it exhibits large intrinsic scatter.¹³ As discussed by previous authors, the large scatter in $\varepsilon_{\text{ff,obs}}$ may arise for a number of reasons. First, as in our mock observed clouds, sampling clouds at different evolutionary stages (low stellar mass and high gas mass at an early evolutionary stage and the opposite at a later stage), is an important source of scatter (see also Grudić et al. 2019). Second, if the SFR in a cloud accelerates with time it will tend to produce a large scatter in $\varepsilon_{\text{ff,obs}}$ (e.g., Lee et al. 2016) (although in fact we do not find evidence for accelerating SFR in our simulations). Third, poor sampling of the IMF at the high-mass end can be a source of large scatter and bias in the light-to-mass ratio and hence the inferred SFR, especially for SFR tracers relying on ionizing radiation (e.g., da Silva et al. 2014; Geen et al. 2018). Fourth, some variations can be induced by the distribution of $\alpha_{\text{vir,0}}$ and $\mu_{\Phi,0}$ of initial clouds (e.g., Federrath 2013), which in reality would represent a varying dynamical environment where molecular clouds form. In addition, there is scatter introduced in the observational estimation of cloud mass and t_{ff} , largely because the former usually depends on conversion from CO luminosity via X_{CO} , which is known from both observations and modeling to have significant scatter (e.g., Pineda et al. 2008; Gong et al. 2020; Seifried et al. 2020).

4. SUMMARY AND DISCUSSION

In this work, we have presented a suite of RMHD simulations modeling the evolution of a turbulent, magnetized GMC and its dispersal by UV radiation feedback from embedded star clusters. Our simulations

model radiation from both internal cluster particles (using adaptive ray tracing) and external sources (using the six-ray approximation). The radiative transfer calculation is coupled with a simple photochemistry module that follows the non-equilibrium abundances of molecular, atomic, and ionized hydrogen as well as equilibrium abundances of C- and O-bearing species. Dynamical evolution is driven by the high thermal pressure of the ionized (photoevaporated) gas, and by the radiation pressure of both LyC and FUV on the gas/dust.

Our model clouds all have a common initial mass $M_0 = 10^5 M_\odot$, radius $R_0 = 20 \text{ pc}$, and freefall time $t_{\text{ff,0}} = 4.68 \text{ Myr}$. They differ in the initial level of turbulence and in the initial uniform magnetic field that threads the clouds. In the α -series models, we vary the initial kinetic virial parameter $\alpha_{\text{vir,0}}$ between 1 and 5 and adopt a fixed initial mass-to-magnetic flux ratio $\mu_{\Phi,0} = 2$ (relative to the critical mass-to-flux). In the β -series models, we adopt a fixed $\alpha_{\text{vir,0}} = 2$, while varying $\mu_{\Phi,0}$ between 0.5 and 8; we also consider the unmagnetized case ($\mu_{\Phi,0} = \infty$). For each cloud model with a given $(\alpha_{\text{vir,0}}, \mu_{\Phi,0})$, we run five simulations with different turbulence realizations. Our fiducial model has $(\alpha_{\text{vir,0}}, \mu_{\Phi,0}) = (2, 2)$, corresponding to an initial 1D velocity dispersion of 2.9 km s^{-1} and magnetic field strength of $13.5 \mu\text{G}$.

The following summarizes key results from our work:

1. *Overall Evolution.* Clouds in our simulations undergo the following evolutionary stages: (1) development of filamentary structures, (2) formation of sink particles and compact H II regions within filaments, (3) breakout and merging of H II regions that photoevaporate and dynamically eject the cold neutral gas, leading ultimately to quenching of star formation. Compared to the fiducial model, stronger turbulence in initially unbound ($\alpha_{\text{vir,0}} > 2$) clouds makes them expand in size and lose a larger fraction of neutral gas as outflows (Figure 17 and Figure 5(e)). In strongly magnetized clouds ($\mu_{\Phi,0} \leq 1$), filaments are aligned predominantly perpendicular to the direction of large-scale magnetic fields (Figure 18) and the motion of (both neutral and ionized) gas is highly anisotropic (Figures 4 and 5(j)). Models with different turbulence realizations show that the initial large-scale velocity field and its relative orientation to the magnetic field affect the details of structure formation and ensuing cluster formation, giving rise to moderate variations in simulation outcomes (Figures 8–12 and Table 2).

2. *Star Formation Rate and Efficiency.* For all models, UV radiation feedback is very effective in dispersing gas and keeping the final cloud-scale SFE low. Both the final SFE and the SFR are reduced in models with strong turbulence and magnetic fields. The median value of the final SFE (ε_*) ranges between 2.1% and 9.5% in the α -series and between 2.4% and 8.4% in the β -series models, systematically increasing with decreasing $\alpha_{\text{vir,0}}$.

¹³ From (a) to (d), the median value $\varepsilon_{\text{ff,obs}}$ of each sample is 0.015, 0.004, 0.018, and 0.075, and the scatter is 0.5, 0.6, 0.8, and 0.6 dex. The systematically higher ε_{ff} in the LMC may partly be due to the difference in the method by which molecular clouds are matched to star-forming regions (identified by H α or free-free emission) (Krumholz et al. 2019).

and increasing $\mu_{\Phi,0}$. Different realizations of turbulence lead to $\sim 2\text{--}5\%$ variation (up to a factor of $\sim 2\text{--}3$) in the final SFE. The SFE at the nominal time of the first supernovae ($\varepsilon_{*,3\text{Myr}}$) ranges between 0.5% and 7% and is about $50^{+20\%}_{-20\%}$ of the final SFE (Figure 9).

The time-averaged SFR ($\langle \dot{M}_* \rangle$) is systematically lower at higher $\alpha_{\text{vir},0}$ and lower $\mu_{\Phi,0}$ (Figure 8). The median value of the gas depletion timescale $t_{\text{dep},0} = M_0/\langle \dot{M}_* \rangle$ ranges between 58–255 Myr in the α -series models and 62–464 Myr in the β -series models.

3. Mass Loss Efficiency. In most of our simulated clouds, the majority of cloud mass is lost via photoevaporation followed by dynamical ejection ($\varepsilon_{\text{ion}} \sim 0.6\text{--}0.8$; Figure 10). Initially unbound clouds have a higher fraction of gas ejected as neutrals due to expansion driven by initial turbulence. In strongly magnetized clouds, most of the gas is ejected in the atomic phase due to the low ionizing photon rate and magnetic confinement, which limits escape routes of the gas.

4. Evolutionary Timescales. The median value of the time at which the first star formation occurs ($t_{*,0}$) is 3.5–4.3 Myr in the α -series models and 2.1–8.6 Myr in the β -series models. Except for the magnetically subcritical clouds (A2B05), clouds in our simulations form stars on timescales of $t_{\text{SF}} \sim 5\text{--}7$ Myr (or 1–1.5 freefall times) and are destroyed within $t_{\text{dest},\text{H}_2} \sim 6\text{--}9$ Myr (or 1.3–2.0 freefall times) after the onset of radiation feedback (Figure 11). Magnetically subcritical clouds have longer evolutionary timescales because of the low SFR and inefficient mass loss processes.

5. Escape of Radiation. The cumulative median escape fraction of LyC (FUV) radiation ranges between 21–34% (53–69%) in the α -series models and between 13–33% (57–64%) in the β -series. The escape fraction is low in magnetically subcritical clouds because of reduced gas compressibility, which results in less porous structure. Different turbulent realizations yield greater variation in $f_{\text{esc},\text{LyC}}$ than in $f_{\text{esc},\text{FUV}}$.

6. Virial Ratios. We study the evolution of the virial ratio $\tilde{\alpha}_{\text{vir,tot}}$ that accounts for kinetic, thermal, and magnetic energies of the neutral cloud, and compare it with the traditional kinetic virial parameter $\alpha_{\text{vir}} = 5R\sigma_{1\text{d}}^2/(GM_{\text{neu}})$ based on the cloud mass, size, and velocity dispersion (Figures 5 and 13). The virial ratio decreases due to decaying turbulence at early times, but it increases to large values ($\tilde{\alpha}_{\text{vir,tot}} > 10$) at late times as feedback disperses the cloud. In spite of the widely ranging initial conditions of the models, at the time of the first star formation $\tilde{\alpha}_{\text{vir,tot}}$ falls in a fairly narrow range 0.5–1.7. In strongly magnetized clouds, the kinetic energy may be significantly underestimated or overestimated depending on the relative orientation between the observer’s line of sight and the direction of magnetic field. Averaging over directions (as would be

possible with an ensemble average in observations), the traditional virial parameter generally agrees with $\tilde{\alpha}_{\text{vir,tot}}$ within a factor of two. However, gravitational boundedness is systematically overestimated when α_{vir} is used, due to the neglect of magnetic energy.

7. SFE per freefall time. The median value of the SFE per freefall time based on the time-averaged SFR and the initial cloud mass and size ($\varepsilon_{\text{ff},0} = t_{\text{ff},0}\langle \dot{M}_* \rangle/M_0$) ranges between 1.8–8.0% in the α -series and 1.0–7.6% in the β -series, higher at lower $\alpha_{\text{vir},0}$ (weak turbulence) and higher $\mu_{\Phi,0}$ (weak mean magnetic fields) (Figure 14). However, the dependence on $\varepsilon_{\text{ff},0}$ on $\mu_{\Phi,0}$ is very slight in the magnetically supercritical regime. The functional form $\varepsilon_{\text{ff},0} \propto \exp(-Ct_{\text{ff},0}/t_{\text{dyn},0})$ (similar to Padoan et al. 2012, from driven-turbulence simulations) well describes the results of α -series models, with the best-fit parameter $C = 4.06$. The decreasing trend of $\varepsilon_{\text{ff},0}$ with $t_{\text{ff},0}/t_{\text{dyn},0} \propto \alpha_{\text{vir},0}^{1/2}$ is also in qualitative agreement with theoretical models for SFR based on a density threshold (e.g. Krumholz & McKee 2005; Hennebelle & Chabrier 2011; Federrath & Klessen 2012). However, the relation between instantaneous measurements $\varepsilon_{\text{ff,obs}}(t)$ and $\alpha_{\text{vir}}(t)$ (as would be available in observations) shows a quite different (almost orthogonal) trend from both numerical measurements and theoretical models of $\varepsilon_{\text{ff},0}$. The increase in $\varepsilon_{\text{ff,obs}} \propto M_*(R/M_{\text{neu}})^{3/2}$ with instantaneous $t_{\text{ff}}/t_{\text{dyn}} \propto \sigma_{1\text{d}}(R/M_{\text{neu}})^{1/2}$ owes to rapidly evolving cloud and cluster properties (physical expansion of the cloud combined with conversion of neutral gas to stars and ionized gas) which affect both quantities in the same way. This “evolutionary masking” explains why observations of star-forming clouds fail to reproduce the decline of $\varepsilon_{\text{ff},0}$ with $\alpha_{\text{vir},0}$ predicted by the theory (Figure 15).

Our conclusions regarding the rapid and efficient dispersal of GMCs by ionizing and non-ionizing UV are in agreement with our previous findings in Kim et al. (2018). There, we focused on how evolution and final outcomes depend on the cloud surface density (for a range $\Sigma_0 \approx 10 - 10^3 M_{\odot} \text{ pc}^{-2}$), and found that in all cases star formation is quenched and clouds are dispersed within a few freefall times or several Myrs after star formation commences. Our new simulations, with more realistic physics (addition of realistic thermochemistry, magnetic fields, and time-dependent luminosity) confirm this evolutionary scenario. The short timescales we find are also consistent with recent empirical constraints on rapid cloud dispersal after the onset of star formation (e.g., Kruijssen et al. 2019; Chevance et al. 2020b,c).

Our findings of decreasing SFR and net SFE with increasing $\alpha_{\text{vir},0}$ are consistent with findings from previous hydrodynamical simulations of global clouds (e.g., Raskutti et al. 2016; Bertram et al. 2015; Howard et al. 2016; Dale 2017; Kim et al. 2018), as well as hydrody-

namic and MHD simulations with driven turbulence in a periodic box (Padoan et al. 2012). General theoretical expectations as well as some numerical simulations (e.g., Federrath 2015) suggest lower SFR and SFE in magnetized compared to unmagnetized clouds, but we are not aware of a previous systematic numerical study of the dependence on global mass-to-magnetic flux ratio with realistic feedback.

While traditionally it was usually assumed that the virial parameter is close to unity for GMCs (Solomon et al. 1987), recent extragalactic surveys of molecular gas on scales $\sim 50 - 100$ pc have instead found that the typical virial parameter may be closer to 4 than 1 (Sun et al. 2020b). Measurements of pressure also show that only half can be accounted for by the self-gravity of the cloud (Sun et al. 2020a), which again suggests $\alpha_{\text{vir}} > 2$. Thus, our $\alpha_{\text{vir}} \sim 4 - 5$ models are likely the most realistic, and it is these that have the lowest $\varepsilon_{\text{ff},0} \sim 2 - 3\%$. While the estimate of the mean ε_{ff} from the large extragalactic PHANGS survey is closer to $\sim 1\%$ (Utomo et al. 2018), it must be borne in mind that whole-galaxy averages include diffuse and quiescent molecular gas in clouds prior to the onset of star formation. For our simulations, the quiescent period in fact has comparable duration to the active star-forming epoch; averaging over both the non-star-forming and star-forming epochs would reduce the mean efficiency per unit time. The range of ε_* in our simulations is in good agreement with estimates of the integrated cloud-scale SFE of 4–10% obtained from the statistical analysis of CO and H α emission in nearby star-forming galaxies (Chevance et al. 2020b).

As remarked in Section 3.2.2, the subcritical clouds ($\mu_{\Phi,0} = 0.5$) have evolution very different from other models in several respects. These include an extremely long time until the first star formation followed by very slow star formation and dispersal (the lifetime can exceed 30 Myr for some seeds, and the final SFE $\sim 2 - 3\%$), columnar outflow configuration, very low fraction of gas that is ionized, and extremely low escape fraction of LyC radiation, $f_{\text{esc,LyC}} \sim 8 - 13\%$. The columnar outflow configuration of the subcritical models is not seen in observed GMCs. In addition, the low $f_{\text{esc,LyC}}$ appears insufficient to explain emission from diffuse ionized gas, which requires low-density channels in the large-scale ISM and also sufficient photons escaping from active star-forming clouds (see Kim et al. 2019b; Kado-Fong et al. 2020, and references therein). Another feature of the subcritical models is that the cloud typically consists of massive filaments aligned preferentially perpendicular to the mean magnetic field (e.g. top row of Figure 18). This feature, while unlike observations of GMCs, is reminiscent of the perpendicular alignment between magnetic fields and high-column structures in several nearby lower-mass ($M \lesssim 10^4 M_\odot$) dark molecular clouds (e.g., Soler et al. 2016). This raises the interesting possibility that observed dark clouds, which have low overall SFE and lack of high-mass stars (e.g., Evans et al. 2009), may

be magnetically subcritical. With slow star formation and low total mass, they may typically be destroyed (by external supernova shocks) before they ever form high-mass stars.

We note that our reported values for ε_* are higher than the predictions for the SFE ($\sim 1\%$) based on spherical shell expansion driven by ionized gas pressure and radiation pressure (Kim et al. 2016; Rahner et al. 2019; Inoguchi et al. 2020). As explained previously in Kim et al. (2018), several factors contribute to this. One factor is the filamentary nature of the gas distribution, which allows a significant fraction of radiation to escape without contributing direct radiation pressure or photoevaporating neutral gas and helping to maintain the thermal pressure in ionized gas. Also, given the turbulent nature of clouds and multiple sources, thermal and radiation pressure forces may partially cancel, unlike the situation for a spherical cloud with a central source. In clouds with realistic structure, forces derived from feedback are reduced by an order of magnitude compared to simple spherical estimates (e.g. Figure 13 of Kim et al. 2018). While idealized analytic studies are valuable for identifying key physical effects and predicting trends in parameter dependence, numerical simulations with realistic geometry and accurate physical treatments are required in order to obtain quantitative predictions for star formation rates and efficiencies. Indeed, idealized spherical evolution driven by ionized gas pressure and radiation pressure does not even include the photoevaporation mechanism, which we find (as in Kim et al. (2018)) is the main means for dispersing the cloud. Although not always taken under consideration in simple treatments of cloud destruction (e.g. Chevance et al. 2020c), we note more generally that photoevaporation is a distinct mechanism from acceleration of neutral gas by the pressure of confined photoionized gas, and results in a much larger fraction of gas becoming ionized.

The present simulations have made a significant advance over previous work in terms of physical realism. However, there is still more to be done. One limitation of the present simulations is the isolated nature of clouds. The isolation of clouds means that they are not affected by events in the surrounding ISM, which in reality may be important in high density environments such as spiral arms where GMCs are near neighbors. These events include supernovae from neighboring, more mature star-forming regions, which may destroy a cloud before star formation reaches the limit imposed by its own internal feedback.

A second limitation is the idealized spherical initial condition with uniform density and magnetic field. Our model clouds become highly filamentary before star formation commences, so we do not consider the uniform spherical initial condition in itself a serious issue. However, our model clouds are at much higher density than the mean ISM, and it is clearly desirable to follow the ISM condensation processes that form GMCs at high

resolution with comprehensive physics, not least because this removes the need to artificially set an initial virial parameter and mass-to-flux ratio. Zoom-in simulations (e.g. Seifried et al. 2017; Haid et al. 2019; Seifried et al. 2020) offer a route to a more complete and holistic numerical study of molecular cloud lifecycle, from formation to destruction.

A third limitation is related to our treatment of star formation. In our simulations, we use sink particles, which are relatively massive, to represent regions of the cloud that have collapsed gravitationally. Because our approach does not resolve individual stars, we adopt the same time-dependent light-to-mass ratio for all particles, which assumes a fully-sampled IMF. While our clouds are massive enough that a fully-sampled IMF is reasonable over the lifetime of the cloud, stochastic IMF sampling is not properly represented during the earlier formation stages. Sampling from the IMF would lead to additional statistical variations in the lifetime SFE (Grudić & Hopkins 2019) on top of those we have found from turbulence sampling, since clouds that happen to form more high-mass stars early would be able to quench star formation more rapidly, and vice versa for those with late formation of massive stars. Simple methods for IMF sampling have been developed to address this (Soromani et al. 2017), but just as for turbulence sampling, IMF sampling greatly increases the total computational expense because multiple runs are needed.

Beyond addressing the above issues, another important goal for future work is to include additional forms of feedback, rather than only radiation. In particular, stellar winds may be important at early stages after star clusters form (especially in very dense clouds), while supernovae may be important at late stages (in low density clouds with long lifetimes). However, the reduction

of the CFL timestep necessary to follow hot gas implies considerably higher computational expense. This underscores the imperative for numerical algorithms that both represent the underlying equations accurately, and are performance-optimized for modern computational platforms.

ACKNOWLEDGMENTS

J.-G.K. acknowledges the participants of Paris-Saclay University’s Institut Pascal program “The Self-Organized Star Formation Process” for useful discussions. J.-G.K. benefited from the KITP program on “Globular Clusters at the Nexus of Star and Galaxy Formation”, which is supported by the National Science Foundation under Grant No. NSF PHY-1748958. J.-G.K. acknowledges support from the Lyman Spitzer, Jr. Postdoctoral Fellowship at Princeton University. This work was partly supported by the National Science Foundation (AARG award AST-1713949). Computational resources were provided by the Princeton Institute for Computational Science and Engineering (PICSciE) and the Office of Information Technology’s High Performance Computing Center at Princeton University.

Software: *Athena* (Stone et al. 2008; Stone & Gardiner 2009), *ParaView* (Ayachit 2015), *IPython* (Perez & Granger 2007), *NumPy* (van der Walt et al. 2011), *xarray* (Hoyer & Hamman 2017), *scipy* (Virtanen et al. 2020), *Matplotlib* (Hunter 2007), *Astropy* (Astropy Collaboration et al. 2013, 2018), *pandas* (McKinney et al. 2010), *yt* (Turk et al. 2011).

REFERENCES

Adamo, A., Ryon, J. E., Messa, M., et al. 2017, *ApJ*, 841, 131

Adamo, A., Zeidler, P., Kruijssen, J. M. D., et al. 2020, *SSRv*, 216, 69

Akimkin, V. V., Kirsanova, M. S., Pavlyuchenkov, Y. N., & Wiebe, D. S. 2015, *MNRAS*, 449, 440

Ali, A., Harries, T. J., & Douglas, T. A. 2018, *MNRAS*, 477, 5422

Arthur, S. J., Henney, W. J., Mellema, G., de Colle, F., & Vázquez-Semadeni, E. 2011, *MNRAS*, 414, 1747

Astropy Collaboration, Robitaille, T. P., Tollerud, E. J., et al. 2013, *A&A*, 558, A33

Astropy Collaboration, Price-Whelan, A. M., Sipőcz, B. M., et al. 2018, *AJ*, 156, 123

Ayachit, U. 2015, *The ParaView Guide: A Parallel Visualization Application* (Clifton Park, NY, USA: Kitware, Inc.)

Ballesteros-Paredes, J., Vázquez-Semadeni, E., & Scalo, J. 1999, *ApJ*, 515, 286

Barnes, A. T., Longmore, S. N., Battersby, C., et al. 2017, *MNRAS*, 469, 2263

Bertoldi, F., & McKee, C. F. 1992, *ApJ*, 395, 140

Bertram, E., Glover, S. C. O., Clark, P. C., & Klessen, R. S. 2015, *MNRAS*, 451, 3679

Bolatto, A. D., Leroy, A. K., Rosolowsky, E., Walter, F., & Blitz, L. 2008, *ApJ*, 686, 948

Chastenet, J., Sandstrom, K., Chiang, I. D., et al. 2019, *ApJ*, 876, 62

Chevance, M., Kruijssen, J. M. D., Vazquez-Semadeni, E., et al. 2020a, *SSRv*, 216, 50

Chevance, M., Kruijssen, J. M. D., Hygate, A. P. S., et al. 2020b, *MNRAS*, 493, 2872

Chevance, M., Kruijssen, J. M. D., Krumholz, M. R., et al. 2020c, arXiv e-prints, arXiv:2010.13788

Crutcher, R. M. 1999, *ApJ*, 520, 706

—. 2012, *ARA&A*, 50, 29

Crutcher, R. M., Wandelt, B., Heiles, C., Falgarone, E., & Troland, T. H. 2010, *ApJ*, 725, 466

Cunningham, A. J., Krumholz, M. R., McKee, C. F., & Klein, R. I. 2018, *MNRAS*, 476, 771

da Silva, R. L., Fumagalli, M., & Krumholz, M. R. 2014, *MNRAS*, 444, 3275

Dale, J. E. 2015, *NewAR*, 68, 1

—. 2017, *MNRAS*, 467, 1067

Dale, J. E., Ercolano, B., & Bonnell, I. A. 2012, *MNRAS*, 424, 377

Deharveng, L., Schuller, F., Anderson, L. D., et al. 2010, *A&A*, 523, A6

Draine, B. T. 1978, *ApJS*, 36, 595

—. 2011a, *ApJ*, 732, 100

—. 2011b, *Physics of the Interstellar and Intergalactic Medium* (Princeton University Press)

Draine, B. T., & Bertoldi, F. 1996, *ApJ*, 468, 269

Evans, Neal J., I. 1991, in *Astronomical Society of the Pacific Conference Series*, Vol. 20, *Frontiers of Stellar Evolution*, ed. D. L. Lambert, 45

Evans, Neal J., I., Heiderman, A., & Vutisalchavakul, N. 2014, *ApJ*, 782, 114

Evans, Neal J., I., Dunham, M. M., Jørgensen, J. K., et al. 2009, *ApJS*, 181, 321

Fall, S. M., Krumholz, M. R., & Matzner, C. D. 2010, *ApJL*, 710, L142

Federrath, C. 2013, *MNRAS*, 436, 3167

—. 2015, *MNRAS*, 450, 4035

Federrath, C., & Klessen, R. S. 2012, *ApJ*, 761, 156

Franco, J., Shore, S. N., & Tenorio-Tagle, G. 1994, *ApJ*, 436, 795

Fukui, Y., & Kawamura, A. 2010, *ARA&A*, 48, 547

Fukushima, H., Yajima, H., Sugimura, K., et al. 2020, *MNRAS*, 497, 3830

Gardiner, T. A., & Stone, J. M. 2008, *Journal of Computational Physics*, 227, 4123

Geen, S., Hennebelle, P., Tremblin, P., & Rosdahl, J. 2016, *MNRAS*, 463, 3129

Geen, S., Soler, J. D., & Hennebelle, P. 2017, *MNRAS*, 471, 4844

Geen, S., Watson, S. K., Rosdahl, J., et al. 2018, *MNRAS*, 481, 2548

Glatzle, M., Ciardi, B., & Graziani, L. 2019, *MNRAS*, 482, 321

Glover, S. C. O., & Mac Low, M.-M. 2007, *ApJS*, 169, 239

Gong, H., & Ostriker, E. C. 2013, *ApJS*, 204, 8

Gong, M., Ostriker, E. C., & Kim, C.-G. 2018, *ApJ*, 858, 16

Gong, M., Ostriker, E. C., Kim, C.-G., & Kim, J.-G. 2020, arXiv e-prints, arXiv:2009.14631

Gong, M., Ostriker, E. C., & Wolfire, M. G. 2017, *ApJ*, 843, 38

González-Samaniego, A., & Vazquez-Semadeni, E. 2020, *MNRAS*, 499, 668

Górski, K. M., Hivon, E., Banday, A. J., et al. 2005, *ApJ*, 622, 759

Grasha, K., Calzetti, D., Bittle, L., et al. 2018, *MNRAS*, 481, 1016

Grasha, K., Calzetti, D., Adamo, A., et al. 2019, *MNRAS*, 483, 4707

Gritschneder, M., Burkert, A., Naab, T., & Walch, S. 2010, *ApJ*, 723, 971

Grudić, M. Y., & Hopkins, P. F. 2019, *MNRAS*, 488, 2970

Grudić, M. Y., Hopkins, P. F., Faucher-Giguère, C.-A., et al. 2018, *MNRAS*, 475, 3511

Grudić, M. Y., Hopkins, P. F., Lee, E. J., et al. 2019, *MNRAS*, 488, 1501

Haid, S., Walch, S., Seifried, D., et al. 2019, *MNRAS*, 482, 4062

He, C.-C., Ricotti, M., & Geen, S. 2019, *MNRAS*, 489, 1880

Heays, A. N., Bosman, A. D., & van Dishoeck, E. F. 2017, *A&A*, 602, A105

Heiles, C., & Troland, T. H. 2005, *ApJ*, 624, 773

Hennebelle, P., & Chabrier, G. 2011, *ApJL*, 743, L29

Hennebelle, P., & Inutsuka, S.-i. 2019, *Frontiers in Astronomy and Space Sciences*, 6, 5

Heyer, M., & Dame, T. M. 2015, *ARA&A*, 53, 583

Heyer, M., Krawczyk, C., Duval, J., & Jackson, J. M. 2009, *ApJ*, 699, 1092

Heyer, M. H., & Brunt, C. M. 2004, *ApJL*, 615, L45

Hoang, T., Tram, L. N., Lee, H., & Ahn, S.-H. 2019, *Nature Astronomy*, 3, 766

Hollenbach, D., & McKee, C. F. 1979, *ApJS*, 41, 555

Howard, C. S., Pudritz, R. E., & Harris, W. E. 2016, *MNRAS*, 461, 2953

Hoyer, S., & Hamman, J. 2017, *Journal of Open Research Software*, 5, doi:10.5334/jors.148. <http://doi.org/10.5334/jors.148>

Hunter, J. D. 2007, *Computing in Science and Engineering*, 9, 90

Indriolo, N., Geballe, T. R., Oka, T., & McCall, B. J. 2007, *ApJ*, 671, 1736

Inoguchi, M., Hosokawa, T., Mineshige, S., & Kim, J.-G. 2020, *MNRAS*, 497, 5061

Kado-Fong, E., Kim, J.-G., Ostriker, E. C., & Kim, C.-G. 2020, *ApJ*, 897, 143

Kauffmann, J., Pillai, T., & Goldsmith, P. F. 2013, *ApJ*, 779, 185

Kennicutt, R. C., & Evans, N. J. 2012, *ARA&A*, 50, 531

Kim, C.-G., Choi, S. K., & Flauger, R. 2019a, *ApJ*, 880, 106

Kim, C.-G., & Ostriker, E. C. 2017, *ApJ*, 846, 133

Kim, C.-G., Ostriker, E. C., Somerville, R. S., et al. 2020, *ApJ*, 900, 61

Kim, J.-G., & Kim, W.-T. 2014, *ApJ*, 797, 135

Kim, J.-G., Kim, W.-T., & Ostriker, E. C. 2016, *ApJ*, 819, 137

—. 2018, *ApJ*, 859, 68

—. 2019b, *ApJ*, 883, 102

Kim, J.-G., Kim, W.-T., Ostriker, E. C., & Skinner, M. A. 2017, *ApJ*, 851, 93

Kruijssen, J. M. D., Schruba, A., Chevance, M., et al. 2019, *Nature*, 569, 519

Krumholz, M. R. 2014a, *PhR*, 539, 49

—. 2014b, *MNRAS*, 437, 1662

Krumholz, M. R., & Federrath, C. 2019, *Frontiers in Astronomy and Space Sciences*, 6, 7

Krumholz, M. R., Matzner, C. D., & McKee, C. F. 2006, *ApJ*, 653, 361

Krumholz, M. R., & McKee, C. F. 2005, *ApJ*, 630, 250

Krumholz, M. R., McKee, C. F., & Bland -Hawthorn, J. 2019, *ARA&A*, 57, 227

Krumholz, M. R., & Tan, J. C. 2007, *ApJ*, 654, 304

Lee, E. J., Miville-Deschénes, M.-A., & Murray, N. W. 2016, *ApJ*, 833, 229

Leitherer, C., Ekström, S., Meynet, G., et al. 2014, *ApJS*, 212, 14

Leroy, A. K., Schinnerer, E., Hughes, A., et al. 2017, *ApJ*, 846, 71

Li, H., Griffin, G. S., Krejny, M., et al. 2006, *ApJ*, 648, 340

Li, H., Vogelsberger, M., Marinacci, F., & Gnedin, O. Y. 2019, *MNRAS*, 487, 364

Li, H.-B., Fang, M., Henning, T., & Kainulainen, J. 2013, *MNRAS*, 436, 3707

Li, H.-B., & Henning, T. 2011, *Nature*, 479, 499

Liu, T., Evans, N. J., Kim, K.-T., et al. 2020, *MNRAS*, 496, 2821

Mac Low, M.-M., & Klessen, R. S. 2004, *Reviews of Modern Physics*, 76, 125

Mao, S. A., Ostriker, E. C., & Kim, C.-G. 2020, *ApJ*, 898, 52

Matzner, C. D. 2002, *ApJ*, 566, 302

McKee, C. F., & Ostriker, E. C. 2007, *ARA&A*, 45, 565

McKee, C. F., & Zweibel, E. G. 1992, *ApJ*, 399, 551

McKinney, W., et al. 2010, in *Proceedings of the 9th Python in Science Conference*, Vol. 445, Austin, TX, 51–56

Mellema, G., Arthur, S. J., Henney, W. J., Iliev, I. T., & Shapiro, P. R. 2006, *ApJ*, 647, 397

Miville-Deschénes, M.-A., Murray, N., & Lee, E. J. 2017, *ApJ*, 834, 57

Mooney, T. J., & Solomon, P. M. 1988, *ApJL*, 334, L51

Murray, N., Quataert, E., & Thompson, T. A. 2010, *ApJ*, 709, 191

Myers, P. C., Dame, T. M., Thaddeus, P., et al. 1986, *ApJ*, 301, 398

Nakano, T., & Nakamura, T. 1978, *PASJ*, 30, 671

Neufeld, D. A., & Wolfire, M. G. 2017, *ApJ*, 845, 163

Ochsendorf, B. B., Meixner, M., Roman-Duval, J., Rahman, M., & Evans, Neal J., I. 2017, *ApJ*, 841, 109

Ostriker, E. C., Stone, J. M., & Gammie, C. F. 2001, *ApJ*, 546, 980

Padoan, P., Federrath, C., Chabrier, G., et al. 2014, in *Protostars and Planets VI*, ed. H. Beuther, R. S. Klessen, C. P. Dullemond, & T. Henning, 77

Padoan, P., Haugbølle, T., & Nordlund, Å. 2012, *ApJL*, 759, L27

Padoan, P., & Nordlund, Å. 2011, *ApJ*, 730, 40

Palmeirim, P., André, P., Kirk, J., et al. 2013, *A&A*, 550, A38

Pellegrini, E. W., Oey, M. S., Winkler, P. F., et al. 2012, *ApJ*, 755, 40

Perez, F., & Granger, B. E. 2007, *Computing in Science and Engineering*, 9, 21

Pineda, J. E., Caselli, P., & Goodman, A. A. 2008, *ApJ*, 679, 481

Planck Collaboration, Ade, P. A. R., Aghanim, N., et al. 2016, *A&A*, 586, A138

Rahner, D., Pellegrini, E. W., Glover, S. C. O., & Klessen, R. S. 2019, *MNRAS*, 483, 2547

Raskutti, S., Ostriker, E. C., & Skinner, M. A. 2016, *ApJ*, 829, 130

—. 2017, *ApJ*, 850, 112

Redman, M. P., Williams, R. J. R., Dyson, J. E., Hartquist, T. W., & Fernandez, B. R. 1998, *A&A*, 331, 1099

Roman-Duval, J., Jackson, J. M., Heyer, M., Rathborne, J., & Simon, R. 2010, *ApJ*, 723, 492

Safarzadeh, M., & Scannapieco, E. 2016, *ApJL*, 832, L9

Schinnerer, E., Hughes, A., Leroy, A., et al. 2019, *ApJ*, 887, 49

Seifried, D., Haid, S., Walch, S., Borchert, E. M. A., & Bisbas, T. G. 2020, *MNRAS*, 492, 1465

Seifried, D., Walch, S., Girichidis, P., et al. 2017, *MNRAS*, 472, 4797

Singh, A., Matzner, C. D., & Jumper, P. H. 2019, *ApJ*, 878, 22

Skinner, M. A., & Ostriker, E. C. 2015, *ApJ*, 809, 187

Soler, J. D. 2019, *A&A*, 629, A96

Soler, J. D., Alves, F., Boulanger, F., et al. 2016, A&A, 596, A93

Solomon, P. M., Rivolo, A. R., Barrett, J., & Yahil, A. 1987, ApJ, 319, 730

Sormani, M. C., Treß, R. G., Klessen, R. S., & Glover, S. C. O. 2017, MNRAS, 466, 407

Sternberg, A., Le Petit, F., Roueff, E., & Le Bourlot, J. 2014, ApJ, 790, 10

Stone, J. M., & Gardiner, T. 2009, NewA, 14, 139

Stone, J. M., Gardiner, T. A., Teuben, P., Hawley, J. F., & Simon, J. B. 2008, ApJS, 178, 137

Sun, J., Leroy, A. K., Schruba, A., et al. 2018, ApJ, 860, 172

Sun, J., Leroy, A. K., Ostriker, E. C., et al. 2020a, ApJ, 892, 148

Sun, J., Leroy, A. K., Schinnerer, E., et al. 2020b, ApJL, 901, L8

Thompson, K. L., Troland, T. H., & Heiles, C. 2019, ApJ, 884, 49

Tomisaka, K., Ikeuchi, S., & Nakamura, T. 1988, ApJ, 335, 239

Turk, M. J., Smith, B. D., Oishi, J. S., et al. 2011, ApJS, 192, 9

Utomo, D., Sun, J., Leroy, A. K., et al. 2018, ApJL, 861, L18

van der Walt, S., Colbert, S. C., & Varoquaux, G. 2011, Computing in Science and Engineering, 13, 22

Virtanen, P., Gommers, R., Oliphant, T. E., et al. 2020, Nature Methods, 17, 261

Vutisalchavakul, N., Evans, Neal J., I., & Heyer, M. 2016, ApJ, 831, 73

Ward-Thompson, D., Pattle, K., Bastien, P., et al. 2017, ApJ, 842, 66

Weingartner, J. C., & Draine, B. T. 2001a, ApJ, 548, 296

—. 2001b, ApJS, 134, 263

Whitworth, A. 1979, MNRAS, 186, 59

Williams, J. P., & McKee, C. F. 1997, ApJ, 476, 166

Zamora-Avilés, M., Vázquez-Semadeni, E., González, R. F., et al. 2019, MNRAS, 487, 2200

Zuckerman, B., & Evans, N. J., I. 1974, ApJL, 192, L149

Zweibel, E. G. 1990, ApJ, 348, 186

APPENDIX

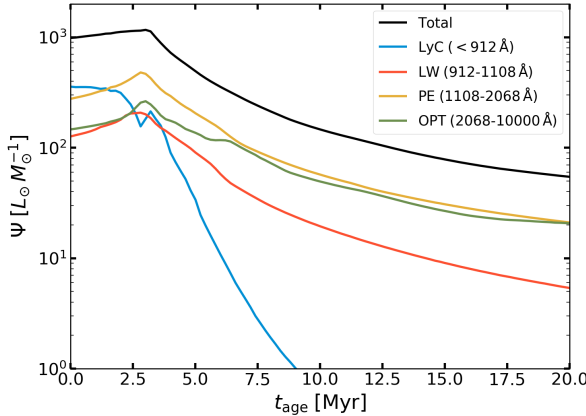


Figure 16. Luminosity per unit mass Ψ as a function of the age of a star cluster sampling the Kroupa IMF. Different lines show Ψ in different frequency bins: H-ionizing (LyC), photoelectric and H₂-dissociating (LW), photoelectric (PE), and optical (OPT) wavelength range.

A. RADIATIVE OUTPUT FROM STAR CLUSTERS

We use the Starburst99 stellar population synthesis code (Leitherer et al. 2014) to calculate the radiative output per unit mass $\Psi = L_*/M_*$ from a coeval stellar population fully sampling the Kroupa IMF in the mass range of 0.1–100 M_\odot . We adopt the Geneva evolutionary tracks for non-rotating, solar metallicity stars and Pauldrach + Hillier stellar atmosphere models. Figure 16 shows the luminosity per unit mass as a function of age in different frequency bins. The conversion factors for ionizing (LyC) and non-ionizing (LW+PE) UV photons drop to 50% of the initial value after 3 Myr and 6 Myr, respectively. The ratios $\Psi_{\text{LW}}/\Psi_{\text{PE}}$ and $\Psi_{\text{OPT}}/\Psi_{\text{PE}}$ range between 0.25–0.5 and 0.5–1 for $t_{\text{age}} < 20$ Myr.

B. SNAPSHOTS OF REPRESENTATIVE MODELS

To provide a sense of the differences in evolution for different models, here we present comparison snapshots at times $t_{*,0} - 0.2$ Myr, $t_{*,0} + 2$ Myr, $t_{*,0} + 5$ Myr, $t_{*,0} + 8$ Myr, where $t_{*,0}$ is the time of first star formation. We show projections of gas surface density along the y axis, so that individual panels have x horizontal and z vertical, with the initial magnetic field oriented along the z -direction.

Figure 17 compares members of the α -series with different initial kinetic energy (increasing top to bottom) but identical initial relative amplitudes of all the different turbulent Fourier modes (**seed**= 4) and initial mass-to-magnetic flux ratio $\mu_{\Phi,0} = 2$. The second row

shows the fiducial model. Members of the series with higher initial $\alpha_{\text{vir},0}$ disperse more rapidly and have a lower SFE.

Figure 18 compares members of the β -series with different initial magnetic energy (decreasing top to bottom) and an identical initial turbulence realization ($\alpha_{\text{vir},0} = 2$, **seed**= 4). The third row shows the fiducial model. Dense filamentary structures tend to be aligned perpendicular to the direction of the background magnetic field in strongly-magnetized models, and outflows driven by radiation are primarily parallel to the magnetic field. Weakly magnetized models are overall more isotropic in their evolution, evolve more rapidly, and have higher SFE.

Figure 19 compares different simulations with different initial turbulence seeds (i.e., different initial Fourier amplitudes of the turbulence) and the same value of $\alpha_{\text{vir},0} = 2$, $\mu_{\Phi,0} = 2$. Differences in the detailed turbulence realization can produce quite different morphological evolution, and there can also be significant differences in the SFE (see Figure 9) and other quantitative outcomes.

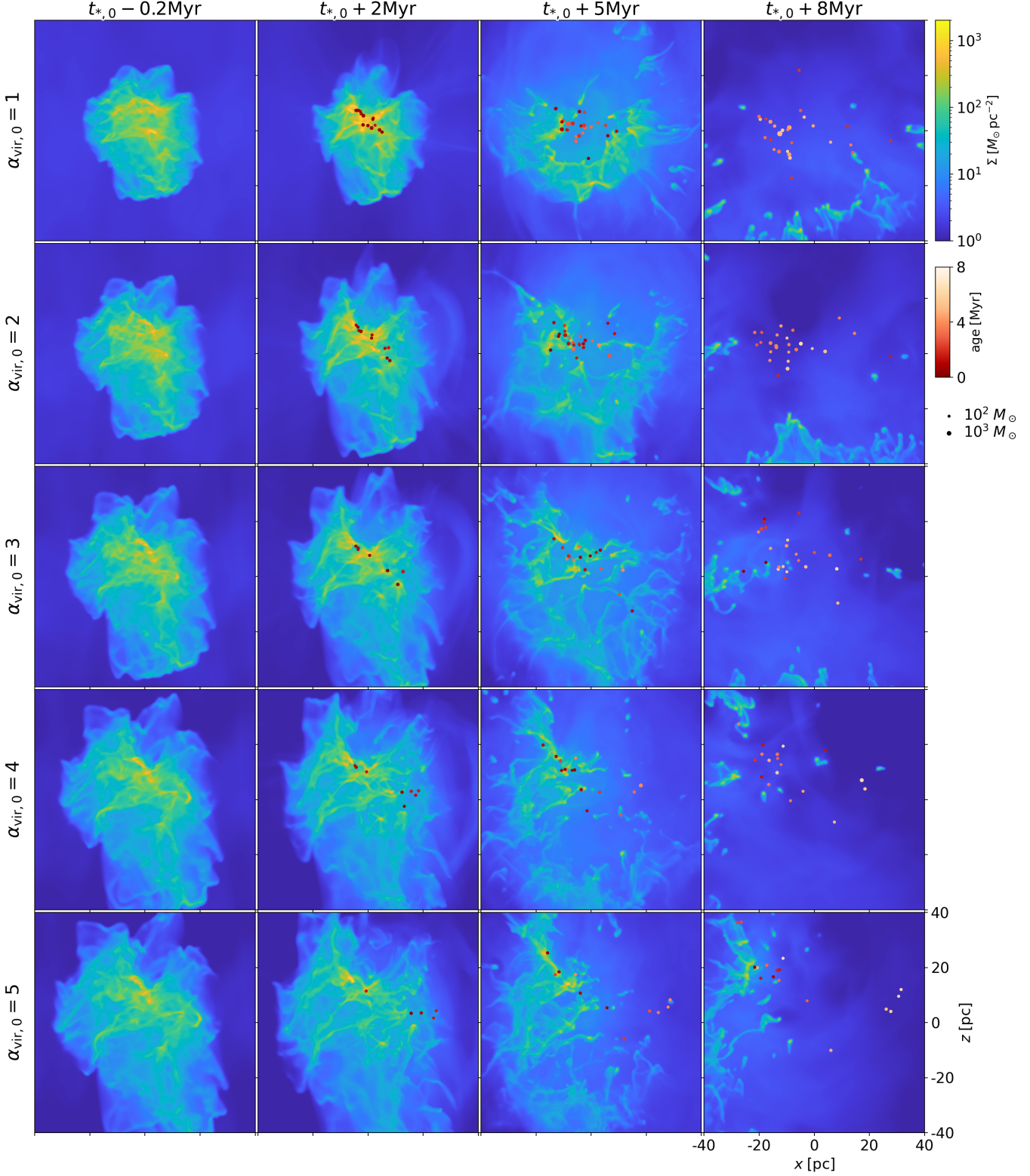


Figure 17. Snapshots of gas surface density projected along the y -axis from the α -series models with `seed` = 4. From top to bottom, the initial virial parameter $\alpha_{\text{vir},0}$ increases from 1 to 5. The projected positions of star particles are indicated by circles. The size and color of circles indicate mass and age, respectively.

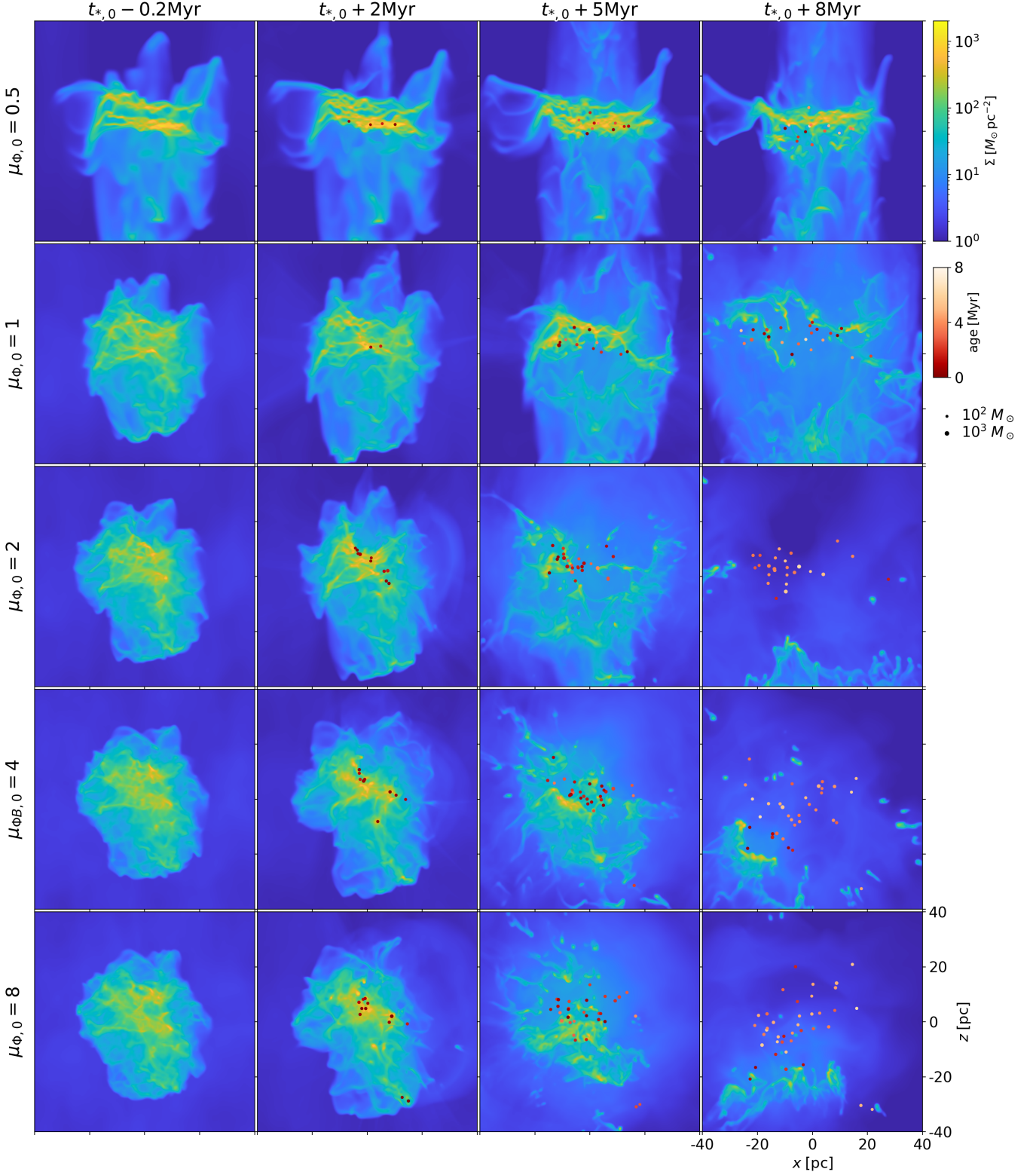


Figure 18. Same as Figure 17 but for the β -series modes with `seed` = 4, which have identical initial turbulent velocity field but varying initial magnetic field strength, decreasing from top to bottom. The corresponding initial mass-to-magnetic flux ratio $\mu_{\Phi,0}$ varies from 0.5 to 8.

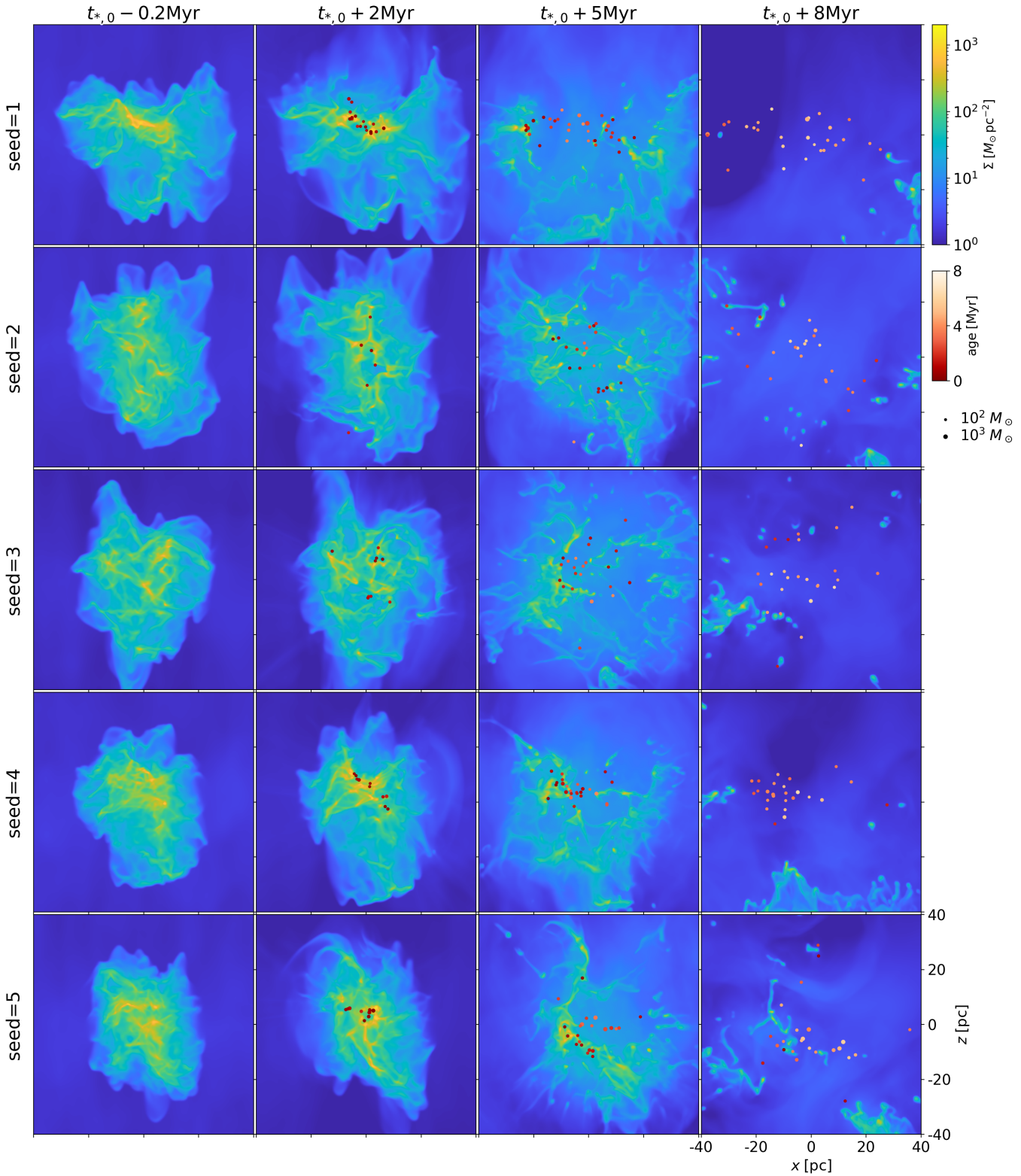


Figure 19. Same as Figure 17 but for the fiducial model A2B2 with different random seeds for the initial turbulent velocity field.